Diss. ETH No. 19023

DIFFUSION BARRIER COATINGS FOR POLYMER CONTAINERS PROCESSED BY PLASMA ENHANCED CHEMICAL VAPOR DEPOSITION

A dissertation submitted to

ETH ZURICH

for the degree of

Doctor of Sciences

presented by

Lutz Körner
Dipl.-Ing. Universität Stuttgart

born on May 25, 1978
in Stuttgart (Germany)

citizen of
Federal Republic of Germany

Accepted on the recommendation of

Prof. Dr. Philipp Rudolf von Rohr (ETH Zurich), examiner
Prof. Dr. Nicholas Spencer (ETH Zurich), co-examiner

2010

Man hat den Eindruck, dass die moderne Physik auf Annahmen beruht, die irgendwie dem Lächeln einer Katze gleichen, die gar nicht da ist.

Albert Einstein

Abstract

Plasma enhanced chemical vapor deposition (PECVD) of silicon oxide (SiO_x) films is widely used for several applications. These films are particularly well suited as gas diffusion barriers for food and pharmaceutical packaging applications due to their optical transparency, recyclability, and suitability for microwaving. The material properties of the substrate play a major role for the deposition process. The deposition of SiO_x on polyesters, e.g. polyethylene terephthalate (PET), is extensively explored. More than PET, however, polypropylene (PP) shows interesting properties for packaging applications, such as a high mechanical strength at elevated temperatures, an inherent water vapor barrier, and a low density at extremely low costs. Other properties of PP, its low glass transition temperature and its high thermal expansion, pose a challenge for the deposition process.

In this work, the fundamentals for PECVD of diffusion barrier coatings on injection molded PP containers with sufficiently low oxygen transmission rate (OTR) for food packaging applications and temperature durability to sustain retort cycling are investigated. As a first step, the PECVD process is explored on PP foil in a wide range of process parameters applying oxygen-hexamethyldisiloxane (HMDSO) mixtures. It is found that PP is much more temperature-sensitive than PET. At high power conditions, high temperatures, measured by a fiber-optical temperature measurement system, deteriorate diffusion barrier performance of SiO_x on PP. If the temperature is not the limiting factor, the applied power per mass of monomer (HMDSO) and the oxygen to monomer flow rate ratio are identified as most important process parameters. The influence of these parameters on the structural and (thermo)mechanical properties of the coatings is investigated more in detail by means of Fourier transform infrared (FTIR) spectroscopy, x-ray photoelectron spectroscopy (XPS), dynamic mechanical analysis (DMA), differential scanning calorimetry (DSC), fragmentation tests, and internal stress measurements. For both of the parameters a similar effect on the coating properties is observed. Carbon-rich, polymer-like coatings from pure HMDSO, i.e. plasma polymerized HMDSO (pp-HMDSO), show promising mechanical properties (low internal stress, excellent adhesion and cohesion) at the expense of barrier performance. The residual oxygen permeation through coatings with a low OTR is ascribed to defects in the SiO_x coating. Defect densities, determined by a chemical etching technique, can be related to the OTR by means of a simple approximate correlation. Both the defect density and the OTR drop by more than one order of magnitude, if a critical coating thickness of approximately 12 nm is exceeded. Further insight into the permeation mechanisms is gained by the activated rate theory.

In a second step, multilayer coatings, comprising layers of good mechanical properties and layers providing barrier performance, are explored. Dry heat and sterilization tests show that the temperature durability of the composites is considerably improved by a pp-HMDSO layer between the PP substrate and a SiO_x barrier layer. Alternatively, carbon-rich films (a-C:N:H and a-Si:C:O:N:H) are promising if the interlayer exceeds a certain thickness. This suggests that these layers act as buffer reducing the high thermal expansion mismatch of the PP substrate and the brittle SiO_x barrier layer. If no interlayer is present, cracks are evidenced in the brittle SiO_x coatings after exposure to elevated temperatures. These cracks cause a severe loss of barrier performance, while no such cracks are found in the multilayer coatings. XPS depth profiles give information about the chemical composition of the multilayer coatings.

Lastly, these findings are employed for the coating of injection molded PP containers. Further process optimization, adaptation of the electrode geometry to the form of the substrate container, and the application of an additional protective lacquer layer results in a composite with sufficiently low OTR for most food packaging applications of $1.7\pm0.5\,\mathrm{cm^3/m^2/d} = 0.017\,\mathrm{cm^3/pack/d}$, which withstands standard thermal sterilization cycling at 121°C with only minor deterioration in OTR.

Zusammenfassung

Die Plasmagasphasenabscheidung (PECVD) siliziumoxidischer Schichten kommt in vielen Anwendungsbereichen zum Einsatz. Besonders gut eignen sich diese Schichten als Diffusionsbarriereschichten auf Verpackungen von Lebensmitteln und pharmazeutischen Produkten aufgrund ihrer optischen Transparenz, ihrer Wiederverwertbarkeit und ihrer Durchlässigkeit für Mikrowellen. Die Materialeigenschaften des Substrates spielen eine wichtige Rolle für den Beschichtungsprozess. Die Abscheidung von $\mathrm{SiO_x}$ auf Polyester, wie z. B. Polyethylenterephthalat (PET), ist umfassend untersucht. Für die Verwendung als Verpackungsmaterial weist jedoch Polypropylen (PP) viele Vorteile auf, wie z. B. eine hohe mechanische Beanspruchbarkeit bei erhöhten Temperaturen, eine inhärente Wasserdampfbarriere und eine geringe Dichte bei sehr geringen Kosten. Andere Eigenschaften von PP, wie die tiefe Glassübergangstemperatur und die hohe thermische Ausdehnung, stellen eine Herausforderung an den Beschichtungsprozess dar.

In dieser Arbeit werden Grundlagen für die Plasmagasphasenabscheidung von Diffusionssperrschichten auf Spritzgussbehältern aus PP mit für Nahrungsmittelverpackungen ausreichend geringer Sauerstofftransmissionsrate (OTR) bei gleichzeitiger Temperaturbeständigkeit für die Sterilisation im Autoklaven erarbeitet. Als erster Schritt wurde der Beschichtungsprozess auf PP-Folie unter Anwendung von Sauerstoff-Hexamethyldisiloxan (HMDSO) Gemischen in einem grossen Prozessparameterbereich untersucht. Dabei hat sich gezeigt, dass PP deutlich temperaturempfindlicher ist als PET. Bei hohem Leistungseintrag verursachen die hohen auftretenden Temperaturen, die mittels eines Glassfaser-Temperaturmesssystems erfasst wurden, eine deutliche Beeinträchtigung der Barriereeigenschaften siliziumoxidischer Schichten auf PP. Für den Fall, dass die Temperatur nicht den limitierenden Faktor darstellt, wurden die eingetragene Leistung bezogen auf die Masse an zugeführtem Monomer (HMDSO) und das Volumenstromverhältnis von Sauerstoff zu HMDSO als massgebliche Prozessparameter identifiziert. Der Einfluss dieser Parameter auf die chemischen und (thermo)mechanischen Eigenschaften der Schichten wurde mittels Fourier-Transformations Infrarot-Spektroskopie (FTIR), Röntgenphotoelektronenspektroskopie (XPS), dynamisch-mechanischer Analyse (DMA), Differentialrasterkalorimetrie (DSC), Zugversuchen und Messungen der Eigenspannungen in den Schichten untersucht. Für beide Parameter wurde ein sehr ähnlicher Effekt auf die Schichteigenschaften beobachtet und die beiden Parameter können nicht als voneinander unabhängig erachtet werden. Kohlenstoffreiche, polymer-ähnliche Schichten, die ohne Zugabe von Sauerstoff in einem HMDSO Plasma abgeschieden wurden (pp-HMDSO), zeigen gute mechanische Eigenschaften (geringe Eigenspannungen, ausgezeichnete adhäsive und cohäsive Eigenschaften) auf Kosten ihrer Diffusionsbarriereeigenschaften. Die verbleibende Sauerstoffpermeation durch Schichten, die eine tiefe OTR aufweisen, ist auf Fehlstellen in der SiO_x-Schicht zurückzuführen. Von der (flächenbezogenen) Dichte an Fehlstellen, die durch ein chemisches Ätzverfahren bestimmt werden kann, kann über eine einfache Korrelation auf die OTR geschlossen werden. Sowohl die Dichte an Fehlstellen als auch die OTR nehmen um mehr als eine Grössenordung ab, wenn eine kritische Schichtdicke von ca. 12 nm überschritten wird. Weitere Schlüsse auf die Mechanismen, die der Permeation zugrunde liegen, können von der „activated rate theory“ abgeleitet werden.

Als zweiter Schritt wurden mehrlagige Schichten untersucht, die aus Schichten mit guten mechanischen Eigenschaften und aus solchen mit guten Barriereeigenschaften bestehen. Temperatur- und Sterilisationstests zeigen, dass die Temperaturbeständigkeit der Laminate durch eine pp-HMDSO Schicht zwischen dem PP Substrat und der SiO_x-Barriereschicht deutlich verbessert wird. Alternativ zeigen auch kohlenstoffreiche Schichten (a-C:N:H und a-Si:C:O:N:H) vielversprechende Ergebnisse, wenn die Zwischenschicht eine Mindestschichtdicke überschreitet. Das weist darauf hin, dass diese Schichten als Puffer für die unterschiedliche thermische Ausdehnung zwischen dem PP Substrat und der spröden SiO_x-Barriereschicht wirken. Wenn spröde SiO_x-Barriereschichten ohne eine Zwischenschicht hohen Temperaturen ausgesetzt werden, zeigen sich Risse in der Schicht, die eine gravierende Beeinträchtigung der Barriereeigenschaften zur Folge haben. In den mehrlagigen Schichten können dagegen keine Risse beobachtet werden. XPS Tiefenprofile geben Aufschluss über die chemische Zusammensetzung der mehrlagigen Schichten.

Schliesslich wurden die gesammelten Erkenntnisse auf die Beschichtung von Spritzgussbehältern aus PP übertragen. Durch weitere Prozessoptimierung, die Anpassung der Elektrodengeometrie an die Behälterform und die Aufbringung einer zusätzlichen Schutzlackschicht kann eine für die meisten Lebensmittelverpackungen ausreichend tiefe OTR von $1.7 \pm 0.5\,\mathrm{cm^3/m^2/d} = 0.017\,\mathrm{cm^3/pack/d}$ erzielt werden, die durch Sterilisation im Autoklaven bei 121°C nur geringfügig beeinträchtigt wird.

Table of Contents

Nomenclature

Latin letters

A	m^2	area
A_0	m^2	permeation cell area
A_{IR}	a.u.	infrared absorbance
A_n	-	Cauchy fitting coefficient
B_n	$\mu\mathrm{m}^2$	Cauchy fitting coefficient
c	wt.%, $\mathrm{mol/m}^3$	concentration
CD	mm^{-1}	crack desity
C_n	$\mu\mathrm{m}^4$	Cauchy fitting coefficient
COS	-	crack onset strain
CP	W/sccm	composite parameter (or J/g)
CR	nm/min/sccm	conversion ratio (or nm/g)
d	m	deflection
D	m^2/s	diffusion coefficient
e	As	elementary charge ($1.602176 \cdot 10^{-19}$)
E	J	energy
E	$\mathrm{N/m}^2$	Young's modulus
ΔE	kJ/mol	apparent activation energy
G	$\mathrm{J/m}^2$	toughness
h	m	thickness
ΔH_S	kJ/mol	sorption enthalpy
j	$\mathrm{mol/m}^2/\mathrm{s}$	permeant flux
k	-	extinction coefficient
k_B	J/K	Boltzmann constant ($1.380650 \cdot 10^{-23}$)
Kn	-	Knudsen number

l	m	length
m	kg	mass
$\dot{m}$	kg/s	mass flow rate
M	g/mol	molar mass
n_d	m^{-2}	defect density
n	m^{-3}	number density
n	-	refractive index
N_A	mol^{-1}	Avogadro constant ($6.022142 \cdot 10^{23}$)
p	Pa	pressure
P	$\mathrm{mol\,m/m^2/s/atm}$	permeability
P_{RF}	W	RF power
q	sccm/sccm	O_2/HMDSO flow rate ratio
r	m	radius
R	nm/min	deposition rate
R_p	-	total reflection coefficient p-polarized
R_s	-	total reflection coefficient s-polarized
$\Re$	J/mol/K	universal gas constant (8.314472)
Re	-	Reynolds number
S	$\mathrm{mol/m^3/Pa}$	solubility
S_a	m	average roughness
t_{dep}	s	deposition time
T	K, °C	temperature
T_{IR}	a.u.	infrared transmittance
TR	$\mathrm{cm^3/m^2/d}$	transmission rate
U	V	electric potential
$\mathbf{v}$	-	velocity vector
v_x	m/s	velocity component in x direction
v_y	m/s	velocity component in y direction
v_z	m/s	velocity component in z direction
$\dot{V}$	sccm	volumetric flow rate
w	m	width
x	m	space coordinate
y	m	space coordinate
z	m	space coordinate

Greek letters

α	K^{-1}	coefficient of linear thermal expansion
α_{Du}	-	Dundurs' first parameter
β_{Du}	-	Dundurs' second parameter
Δ	rad	relative phase shift
ϵ_0	F/m	permittivity in vacuum ($8.8541878 \cdot 10^{-23}$)
ε	-	strain
η	m^2/s	kinematic viscosity
θ	°	angle of incidence
λ	nm	wavelength
λ	m	mean free path
λ_{De}	m	Debye length
ν	-	Poisson's ratio
Π	$mol/m^2/s/atm$	permeance
σ	Pa	stress
σ	m^2	cross section
τ	Pa	shear stress
Φ	J	spectrometer work function
Φ_0	m^{-2}	surface coverage
χ_{iz}	-	degree of ionization
Ψ	rad	relative amplitude ratio

Sub- and superscripts

b	bias
B	binding
e	electron
c	coating
$crit$	critical
D	diffusion
$diss$	dissociation
g	ground
HMDSO	hexamethyldisiloxane
i	internal
i	ion

i	running index
$intr$	intrinsic
ILT	ideal laminate theory
j	running index
kin	kinetic
max	maximum
n	neutral
O_2	oxygen
p	plasma
P	permeation
RF	radio frequency
s	substrate
sat	saturation
th	thermal
tot	total
w	water
Y	yield

Abbreviations

a-C:H	amorphous hydrogenated carbon
a-C:N:H	amorphous hydrogenated carbon nitrogen
a-Si:C:O:N:H	amorphous hydrogenated silicon oxycarbonitride
AFM	atomic force microscopy
Al	aluminum
AlO_x	aluminum oxide
Ar	argon
ATR	attenuated total reflection
BIF	barrier improvement factor
BOPP	biaxially oriented polypropylene
C	carbon
CFD	computational fluid dynamics
CH_3	methyl group
CH_4	methane
C_2H_2	acetylene
CLTE	coefficient of linear thermal expansion

CO	carbon monoxide
CO_2	carbon dioxide
C=O	carboxyl group
CVD	chemical vapor deposition
DC	direct current
DLC	diamond-like carbon
DMA	dynamic mechanical analysis
DSC	differential scanning calorimetry
EEDF	electron energy distribution function
ERR	energy release rate
FTIR	Fourier transform infrared spectroscopy
FWHM	full width at half maximum
GaAs	gallium arsenide
He	helium
HMDSA	hexamethyldisilazane
HMDSO	hexamethyldisiloxane
H_2	hydrogen
H_2O	water
H_2SO_4	sulfuric acid
H_3PO_4	phosphoric acid
ICP	inductively coupled plasma
IFSS	interfacial shear strength
IR	infra-red
$KMnO_4$	potassium permanganate
MW	microwave
N_2	nitrogen
N_2O	nitrous oxide
NH_2	amino group
N=C	imino group
$N \equiv C$	nitrile group
O_2	oxygen
OM	optical microscopy
OTR	oxygen transmission rate
$\mathcal{O}$	order of
pp-HMDSO	plasma polymerized hexamethyldisiloxane
PC	polycarbonate
PDMS	polydimethylsiloxane

PECVD	plasma enhanced chemical vapor deposition
PEEK	polyether ether ketone
PET	polyethylene terephthalate
PI	polyimide
PP	polypropylene
PVD	physical vapor deposition
RBS	radio frequency biased substrate holder
RF	radio frequency
RIE	reactive ion etching
SEM	scanning electron microscopy
Si	silicon
SiH_4	silane
SiN	silicon nitride
SiO_2	silica
SiO_x	silica-like
Si-OH	silanol group
STP	standard temperature and pressure
TEOS	tetraethoxysilane
TMOS	tetramethoxysilane
UHV	ultra high vacuum
UV	ultraviolet
Xe	xenon
XPS	x-ray photoelectron spectroscopy
2D	two-dimensional
3D	three-dimensional

Chapter 1

Introduction

1.1 Motivation

The primary function of packaging materials is to protect goods. For a prolonged shelf-life of food and pharmaceutical products, it is essential that the packaging material provides a diffusion barrier. Many products undergo deteriorative reactions in the presence of oxygen. For some products, the diffusion of water vapor through the packaging material needs to be prevented to maintain the moisture content, while others need to be protected from humidity. Apart from oxygen and water vapor, the diffusion of flavors is an important issue. Thin silicon oxide (SiO_x) films show excellent barrier properties. Especially for food and pharmaceutical packaging these films are employed due to their advantages over metallic thin films, their optical transparency, recyclability, and suitability for microwaving [1].

Unfortunately, it is impossible to apply thin SiO_x films of typically a few tens of nanometers without a supporting base material. Polypropylene (PP) is a highly interesting packaging polymer as it shows high mechanical strength at elevated temperatures, an inherent water vapor barrier, and a low density at extremely low costs. Still, a considerable increase in consumption of PP is predicted for the next years [2]. For 2010 the global PP consumption is expected to exceed 50 million t/a. However, PP seems to be more problematic as base material for the deposition of barrier coatings than polyesters, which are commonly used for barrier coating applications. Apart from its high permeability for oxygen, PP shows a high thermal expansion and a low glass transition temperature. The latter two properties pose a challenge for the deposition process.

SiO_x coatings are widely applied in several other fields besides packaging. Beginning in the 1970s, thin SiO_x coatings were developed for the integrated circuit fabrication in semiconductor industry due to their dielectric properties [3]. Later, SiO_x coatings were employed as protective coatings, e.g. in the automotive industry, because of their chemical, scratch, and abrasion resistance. Emerging fields of application for SiO_x coatings are flexible organic light-emitting devices (OLEDs) and organic solar cells, which are very sensitive to trace amounts of O_2 and H_2O. Therefore, ultra-high barrier materials are to be developed to prevent premature degradation of the device [4–6].

Plasma enhanced chemical vapor deposition (PECVD) is a versatile method for coating of temperature-sensitive materials. Unlike to thermal CVD, it is a nonequilibrium process, i.e. the energy for the conversion of the reactants is provided by highly energetic electrons, while the substrate temperature remains typically below 100°C. Compared to physical vapor deposition (PVD) processes such as sputter, electron beam, and pulsed laser deposition, coating properties, i.e. the internal stress and the chemical composition, are more easily controlled. Moreover, PECVD coatings are superior over PVD coatings regarding their adhesion, since an extended interphase is formed between the substrate and the coating [7]. Most importantly for this work, PECVD is not restricted to the line-of-sight in contrast to PVD methods, and, in principle, the deposition of thin films on 3D geometries is feasible.

1.2 Objectives

The main goal of this work is to elaborate PECVD process conditions for diffusion barrier coatings on 3D injection molded PP containers, which provide sufficient diffusion barrier performance for food packaging applications and sustain retort cycling. While PECVD of SiO_x coatings on flat polyethylene terephthalate (PET) substrate is extensively explored and high diffusion barrier performance is reported [8–11], not as much work is contributed on flat PP substrate. Here, reported results are much more diverse. Properties of the polymeric substrate are known to play an eminently important role. Process conditions, optimized for one substrate, may not easily be transferred to another. Therefore, the PECVD process needs to be optimized for (flat) PP substrate in a first step. For a better process understanding, the most important process parameters are to be identified, and their influence on the mechanical and structural properties of the coatings needs to be investigated. The adhesion of the thin film to the substrate is another crucial point. Brittle coatings on polymers of high thermal expansion are prone to failure by cracking if exposed to elevated temperatures, e.g. during autoclaving [12]. Therefore, a coating with graded properties or a multilayer approach was suggested to improve the temperature durability [13]. This work is incorporated in a collaboration with an industry partner[1], who is well established in thin oxide web coating by electron beam evaporation [14]. While this process is already implemented on an industrial scale, the company is now emerging in the field of vacuum deposition of 3D injection molded substrates. As a first step towards this goal, the results are to be transferred from PP foil to injection molded 2D substrates. A deviant behavior is expected for these substrates due to an increased substrate thickness and different polymer properties. The issue of coating homogeneity further increases the complexity for 3D injection molded substrates. To overcome this problem, the effect of an adapted electrode geometry is explored. Finally, a lacquer layer is intended to be applied for the protection of the PECVD diffusion barrier coating. The right choice and application of the lacquer may further improve the mechanical as well as the diffusion barrier properties of the composite in a synergistic way [15]. Lastly, the lab-scale PECVD reactor setup is very versatile for research, but the geometry of the reactor chamber is not suitable for industrial application. In order to comply with short cycle times, shorter pumping times need to be realized by reducing the reactor volume. Since the deposition is also influenced by the flow field, computational fluid dynamics (CFD) modeling is a valuable tool towards a more applicable design without significantly changing the flow characteristics in the vicinity of the substrate.

---

[1] Alcan Technology & Management AG

Chapter 2

Basics and state of the art

2.1 Fundamentals of plasma processes

The fundamentals of plasma processes have been investigated intensively in the past. A complete coverage of this topic would by far exceed the scope of this work. Therefore, only the most relevant concepts and some basic ideas are introduced. Emphasis is placed on fundamentals which are relevant for the applied process within this work.

2.1.1 Introduction and Definition

A plasma is a partially ionized gas. It is often also referred to as the 4th state of matter, in addition to the solid, the liquid, and the gaseous state. Phase transitions from solid to liquid and from liquid to the gaseous state are induced by increasing the temperature. Further increase of the temperature results in the decomposition of atoms to form electrons and ions and the plasma state is reached. Indeed, more than 99% of the visible matter are in a plasma state, since stars as well as most interstellar matter are a plasma. More precisely, a plasma can be defined as a many-particle system of free electrons, ions, and neutrals (atoms and molecules in their ground and excited states), which is electrically (quasi)neutral and shows collective behavior in the presence of an external field due to charged particle interactions.

2.1.2 Classification of plasmas

Plasmas are characterized by their electron density n_e and their electron temperature T_e (or electron energy $k_B T_e$). T_e and n_e range over many orders of magnitude as shown for several plasma types in Figure 2.1. Low pressure glow discharges, relevant for many technical applications, are

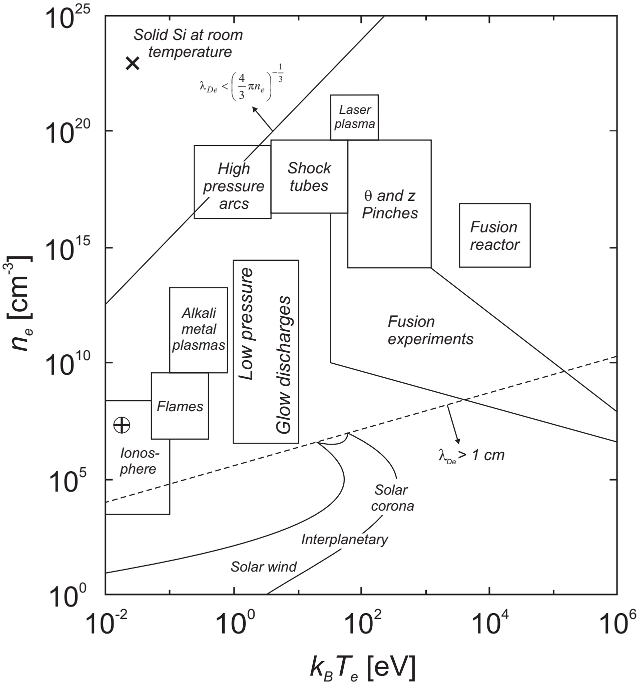

Figure 2.1: Classification of plasmas according to their electron density n_e and electron energy $k_B T_e$. Adapted from [16].

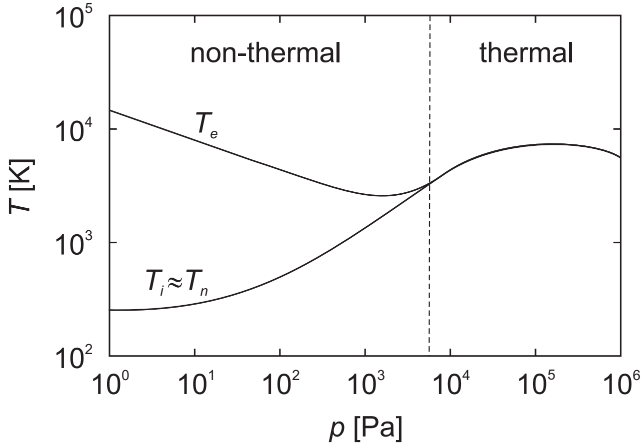

Figure 2.2: Dependence of the electron and ion temperature, T_e and T_i, on the pressure. Reproduced from [17].

characterized by typical values of $k_B T_e = 1 - 10\,\mathrm{eV}$ and $n_e = 10^8 - 10^{13}\,\mathrm{cm}^{-3}$ [16]. These plasmas are not in thermodynamic equilibrium, i.e. $T_i \ll T_e$, and are therefore referred to as non-thermal plasmas. At low pressure conditions, the mean electron energy is several orders of magnitude lower than the mean energy of ions and neutrals as shown in Figure 2.2. This is due to the low elastic collision frequency of the charged species at low pressure resulting in an ineffective heat and momentum transfer. T_e may exceed $10^4\,\mathrm{K}$ in glow discharges, while T_i and T_n are as low as $300 - 500\,\mathrm{K}$, enabling plasma processing of temperature-sensitive materials.

2.1.3 Basic plasma properties

Degree of ionization

Another characteristic of a plasma is the degree of ionization χ_{iz}, defined as

$$\chi_{iz} = \frac{n_i}{n_i + n_n}, \tag{2.1}$$

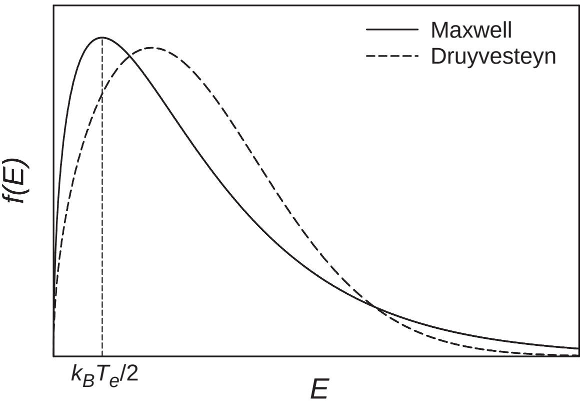

Figure 2.3: Maxwellian and Druyvesteyn electron energy distribution function (EEDF) in a weakly ionized discharge.

where n_n and n_i are the neutral gas and the ion density. Most plasmas are only weakly ionized. For technical plasmas, the degree of ionization χ_{iz} is typically in the range of $10^{-6} - 10^{-3}$.

Electron energy distribution function

Electrons show a distribution of energy. Therefore, ionization and dissociation takes place, even though threshold energies for ionization and dissociation are in general much higher than the mean electron energy E_e. A Maxwellian and a Druyvesteyn electron energy distribution function (EEDF) are sketched in Figure 2.3. For the Maxwellian EEDF, the mean electron energy E_e is given by

$$E_e = \frac{2}{3} k_B T_e. \tag{2.2}$$

Only the electrons of the high-energy tail ('hot-tail') possess sufficient energy to induce ionization and dissociation. Deviations from Maxwellian distribution in the tail may occur by electron heating or electron collision processes. The EEDF derived by Druyvesteyn, assuming constant (hard sphere) cross sections and mean free paths instead of a constant collision frequency, is often a more suitable approximation for low pressure glow discharges, where $T_i \ll T_e$ applies.

Debye shielding

An important characteristic length scale of a plasma is the Debye length λ_{De}. It is described as the length over which charge densities are shielded within a quasineutral plasma, i.e. the distance from a charge above which the quasineutrality condition is fulfilled. Based on Poisson's equation, λ_{De} can be derived as

$$\lambda_{De} = \sqrt{\frac{\epsilon_0 \cdot k_B \cdot T_e}{n_e \cdot e^2}}, \tag{2.3}$$

where ϵ_0 is the permittivity in vacuum. Since the quasineutrality is a compulsive characteristic for the definition of a plasma, the system dimensions have to exceed λ_{De}. Due to the shielding effect, a low-voltage plasma sheath extends to a few Debye lengths in width. For typical values of T_e and n_e in low pressure glow discharges, λ_{De} is in the order of a few tenths of a millimeter.

Sheath formation

The formation of a plasma sheath is illustrated in Figure 2.4. Despite the low degree of ionization and the low T_i and T_n compared to T_e in non-thermal plasmas, ion bombardment of the walls confining a plasma occurs with considerable kinetic energy. This is due to the formation of a plasma sheath near the confining walls, which is related to the much higher thermal velocity of electrons $(eT_e/m_e)^{1/2}$ compared to the velocity of ions, since $m_e \ll m_i$. Due to their high mobility, electrons are rapidly lost to the walls on a short time scale after plasma ignition. This leads to an electric potential drop towards the walls as illustrated in Figure 2.4. The resulting electric field is directed to the walls. Therefore, further electrons are repelled and confined in the plasma zone, while (positive) ions entering the plasma sheath are accelerated by the plasma potential U_p towards the walls.

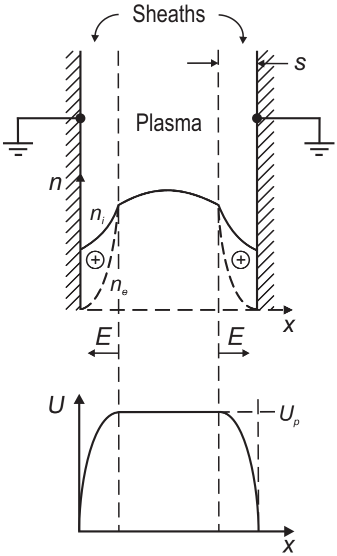

Figure 2.4: Formation of a plasma sheath. Ion and electron density n_i and n_e, electric field E, and electric potential U. Reproduced from [16].

2.1.4 Collision reactions

Momentum, energy, and charge transfer, essential for the excitation of and for sustaining a plasma, occurs via collision reactions. In general, elastic and inelastic collisions are distinguished:

- **Elastic collisions:** Kinetic energy is transferred among the collision partners, while the sum of kinetic energies is conserved and internal energies are not changed.
- **Inelastic collisions:** The sum of kinetic energies is not conserved and kinetic energy is transferred to internal energy. Among the most common inelastic collision reactions are excitation and ionization, where collisions reduce the sum of kinetic energies of the collision partners. Also the contrary effect is observed, which is referred to as superelastic collisions.

Table 2.1: Collision reactions involving electrons and neutrals or ions.

Reaction		Description	
$\mathrm{e^- + A}$	$\rightarrow$	$\mathrm{A + e^-}$	Elastic scattering
	$\rightarrow$	$\mathrm{A^+ + 2e^-}$	Ionization
	$\rightarrow$	$\mathrm{A^* + e^-}$	Excitation
$\mathrm{e^- + A^*}$	$\rightarrow$	$\mathrm{A^+} + 2e^-$	Two-step ionization
$\mathrm{e^- + AB}$	$\rightarrow$	$\mathrm{A + B + e^-}$	Fragmentation
	$\rightarrow$	$\mathrm{A^+ + B + 2e^-}$	Dissociative ionization
	$\rightarrow$	$\mathrm{A^- + B}$	Dissociative attachment
$\mathrm{e^- + A^+ + B}$	$\rightarrow$	$\mathrm{A + B}$	Volume recombination

Important collision reactions in the gas phase involving electrons, ions, and neutrals are summarized in Table 2.1 and 2.2 [18]. Collisions of electrons with molecules may additionally lead to the excitation of vibrational and rotational levels. Furthermore, surface reactions, i.e. heavy particle wall interactions such as etching and deposition, need to be considered, since technical plasmas are generally confined by physical boundaries. The fundamental quantity describing the probability of a certain type of collision is the cross section σ, which depends in general on the velocity of the collision partners. In the particular case of hard shell spheres with the radii r_1 and r_2, the cross section σ is independent of the velocity:

$$\sigma = \pi(r_1 + r_2)^2. \tag{2.4}$$

A related quantity is the mean free path λ, defined as

$$\lambda = \frac{1}{\sigma n}, \tag{2.5}$$

where n is the number density (per unit volume). The mean free path λ describes the distance over which the uncollided flux decays to 1/e of its initial value. For pure (ideal) gases, considering only elastic collisions,

Table 2.2: Collision reactions between ions and neutrals.

Reaction		Description	
$A^+ + B$	$\rightarrow$	$B + A^+$	Elastic scattering
	$\rightarrow$	$A + B^+$	Charge exchange
	$\rightarrow$	$A^+ + B^*$	Excitation
	$\rightarrow$	$A^+ + B^+ + e^-$	Ionization
$A + B^*$	$\rightarrow$	$A^+ + B + e^-$	Penning ionization
$A^+ + BC$	$\rightarrow$	$A^+ + B + C$	Dissociation, fragmentation
$A^\pm + B$	$\rightarrow$	$AB^\pm$	Oligomerization
$A + B$	$\rightarrow$	AB	Oligomerization

the mean free path is given by

$$\lambda = \frac{1}{\sqrt{2}\sigma n} = \frac{1}{4\sqrt{2}\pi r^2 n} = \frac{k_B T}{4\sqrt{2}\pi r^2 p}, \tag{2.6}$$

where r is the atomic or molecular collision radius of the gas. Evidently, the mean free path is inversely proportional to the pressure. For typical pressures of low pressure glow discharges ($1-100\,\mathrm{Pa}$), the mean free path is $\mathcal{O}(10 - 0.1\,\mathrm{mm})$. A dimensionless number for the characterization of gas flows is the Knudsen number, defined as

$$Kn = \frac{\lambda}{l}, \tag{2.7}$$

where l is the most characteristic dimension of the flow domain. For $Kn < \mathcal{O}(0.1)$ viscous flow, i.e. the validity of the laws of continuum mechanics, may be presumed, while $Kn > \mathcal{O}(10)$ implies nearly free molecular flow [19]. Another important dimensionless quantity commonly used in fluid dynamics is the Reynolds number Re. It expresses the ratio of inertia to viscous forces and is defined as

$$Re = \frac{\dot{V} \cdot l}{A \cdot \eta}, \tag{2.8}$$

where η is the kinematic viscosity and A the cross sectional area of the flow domain.

2.1.5 Plasma generation techniques

Alternating electric fields are most commonly used to generate and sustain a plasma in a low-pressure environment for technical applications. Plasma sources are operated at a broad range of frequencies from the kHz (radio frequency, RF) [10, 20, 21] to the GHz (microwave, MW) range [22, 23]. Most commonly, a frequency of 13.56 MHz (or higher harmonics thereof) is used for plasma processes, since this, as well as 2.45 GHz in the MW range, is the common standard in research and industry to avoid interference with telecommunication applications. In the MW range electrons are accelerated and collisions are induced less efficiently as in the RF range due to the higher frequency. For this reason, the generation (ignition) of a MW plasma is more difficult and depends strongly on the pressure and the gas composition. To overcome this problem, often a magnetic field is additionally applied, forcing the electrons on helicon pathways [24, 25]. This concept is referred to as an electron cyclotron resonance (ECR) source. For dual-frequency plasmas, consisting of a MW discharge simultaneously superimposed by a RF signal, high deposition rates are reported combined with the formation of a high voltage sheath [8, 26, 27]. Direct current (DC) electric fields are less frequently employed due to charging effects in case of electrically nonconducting substrates. Dual DC-RF plasma systems show the advantage of a more flexible control of the ion current density and the ion kinetic energy [28].

RF discharges are most commonly applied, as also in this work, and for this reason discussed more in detail. The RF power is either capacitively coupled (CCP) or inductively coupled (ICP) into the plasma. Inductive coupling is realized by a planar or a helical coil, mostly by external coupling through a dielectric wall or window rather than directly in the plasma zone. A time-variant magnetic field is induced by the RF powered coil, leading to electron acceleration. ICP is favorable if a high ion density and low ion bombardment of the adjacent walls is desired. Nevertheless, for most plasma processes, including deposition and etching, capacitive coupling is of advantage. Here, electrodes are arranged in parallel plate configuration in the simplest case as shown in Figure 2.5.

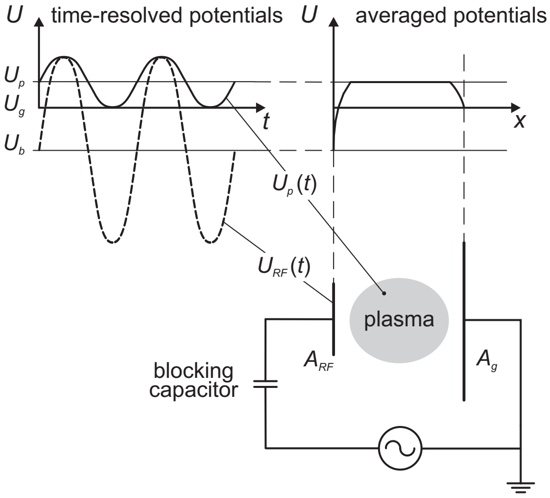

Figure 2.5: Time-resolved and time-averaged self-bias and plasma potential of a RF powered plasma reactor with asymmetric electrode configuration [29, 30].

Alternatively, the entire reactor wall may represent the grounded electrode. On the basis of Figure 2.5, the formation of a DC bias potential (or self-bias potential) for CCP RF discharges can be explained [29]. The self-bias potential induces an ion bombardment of the electrode with considerable kinetic energy of $100 - 1000\,\mathrm{eV}$, which is important for plasma processes. During the positive RF half cycle a high negative charge accumulates on the powered electrode, while during the negative RF half cycle only a smaller positive ion current flows due to the much lower ion mobility compared to the electron mobility. Negative charges accumulate on the electrode during a complete cycle, since the blocking capacitor prevents the flow of current in the external circuit. In subsequent RF cycles, a steady state is reached, since low energetic electrons are repelled by the formed potential. Therefore, the RF signal oscillates around a DC potential, the DC bias potential U_b, which is negative with respect to the plasma potential U_p. The DC bias potential U_b strongly depends on the ratio of the powered to the grounded electrode area. For asymmetric electrode configurations with $A_{RF} < A_g$, as illustrated in Figure 2.5, the main potential drop is obtained at the powered electrode. Due to this fact, the ion bombardment occurs primarily on the powered electrode, and the contamination of the reactor walls is reduced. This is the case if the reactor wall represents the grounded electrode. For a symmetric electrode configuration ($A_{RF} = A_g$), the plasma potential U_p still remains the most positive potential and $U_b = U_g$. Time-averaged potentials may be considered for the ions, since at frequencies in the MHz range ions are unable to follow the oscillation of the electric field.

2.2 Plasma enhanced thin film deposition

After the discovery in the second half of the 19^{th} century, it was not before the 1960s that the formation of polymeric materials under the influence of a plasma, referred to as plasma polymerization, was deliberately investigated [31, 32]. Evolving from the conventional polymerization, plasma polymerization was recognized with the years as a method for the synthesis of an entirely new kind of thin film materials with unique properties. The field attracted more and more attention, and the definition of plasma polymerization was motivated to be extended to a wider field, including not only organic polymeric materials, but also metallic and inorganic elements [33].

2.2.1 Principles of plasma polymerization

Plasma polymers show, unlike conventional polymers, no regular repeating structural unit and are rather described as a random amorphous network of chemical groups, as all active species (atoms, molecules, ions, and radicals), derived in the plasma by many simultaneous reactions from the monomer, contribute to a heterogeneous film growth. Among these species, electrons and ions initiate, but free radicals dominate the film growth [34]. Free radicals are either formed in the gas phase by the collision of free energetic electrons with monomer molecules or on the surface of the deposited films through the dissociation of adsorbed monomer upon electron and ion impact or the absorption of photons.

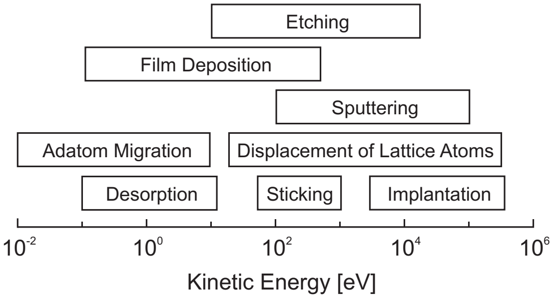

Figure 2.6: Kinetic energy ranges of ion-surface and gas-surface interactions. Adapted from [35].

Plasma-surface interactions

In glow discharges, the degree of ionization is typically very low ($x_{iz} < 10^{-3}$) due to the relatively high energies of ionization. Nevertheless, ion induced effects strongly affect the film growth and composition. Especially if the film is grown on the RF powered electrode, high kinetic ion energies are achieved due to the acceleration of positive ions by the self-bias voltage across the plasma sheath. Most relevant effects of the ion bombardment are summarized in the following. Corresponding kinetic energy ranges are given in Figure 2.6 [35, 36]:

(i) Enhancement of adatom migration

(ii) Desorption of impurity atoms on the surface

(iii) Displacement of surface atoms, smoothing of film

(iv) Trapping or sticking of incident ions on the surface

(v) Sputtering and displacement of atoms

(vi) Enhancement of internal compressive stress

(vii) Film densification (covalent bond rearrangement, hydrogen removal by sputtering or ion-assisted desorption)

(viii) Implantation, adsorption, and nucleation

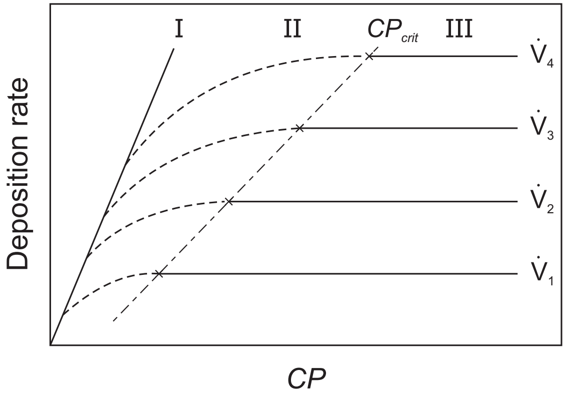

Figure 2.7: Schematic dependence of the deposition rate on the composite parameter $CP = P/\dot{V}M$ for different monomer flow rates ($\dot{V}_1 < \dot{V}_2 < \dot{V}_3 < \dot{V}_4$) indicating the regimes of plasma polymerization. I: energy-deficient, II: transient, III: monomer-deficient regime. Adapted from [33].

Macroscopic description of film growth

In the 1970s, the mechanisms of plasma polymerization were extensively investigated and it was mainly the work of Yasuda that contributed significantly to a deeper understanding [37–39]. In 1978, Yasuda introduced the composite parameter $CP = P/\dot{V}M$, where P is the discharge power, M the molar mass, and $\dot{V}$ the flow rate of the monomer, representing the energy input per unit mass of monomer, to describe and compare glow discharge conditions in plasma polymerization [40]. His semi-empirical model distinguishes three regimes for the dependence of the growth rate on the composite parameter as schematically shown in Figure 2.7. If the power input is the rate-determining parameter, the deposition rate is linearly dependent on CP as indicated by the initial straight line and referred to as energy-deficient regime (I). When sufficient discharge power is available, the monomer flow rate becomes the rate-limiting factor. In this monomer-deficient regime (III), the deposition rate is independent of

CP. This is the case if a critical CP for full glow conditions is exceeded, which depends on the monomer flow rate (here $\dot{V}_1 < \dot{V}_2 < \dot{V}_3 < \dot{V}_4$). In between the two limiting cases an energy-deficient transient regime (II) is obtained. Later on, Matsuda and Yasuda motivated the use of the conversion ratio $CR = R/\dot{V}M$ of monomer to polymer, where R is the deposition rate [41]. The fact that the conversion ratio shows good correlation with CP for various plasma conditions and monomers, affirms that CP and CR are meaningful parameters to describe plasma polymerization processes. It was more recently shown that the composite parameter concept also holds for oxygen diluted HMDSO plasmas at a fixed O_2/HMDSO flow rate ratio q [42].

2.2.2 Silicon oxide coatings

SiO_x coatings are deposited by PECVD for many applications due to the discussed advantages over PVD derived coatings. PECVD SiO_x coatings are often substoichiometric, i.e. they exhibit a considerable carbon and hydrogen content, depending mainly on the process gas mixture and the applied power. This is expressed by the x in SiO_x or the term 'silica-like'. More precisely, it is also referred to as $SiO_xC_zH_z$ in the literature. Nowadays, mainly organosilicon compounds are used as SiO_x precursors instead of the hazardous and pyrophoric silane (SiH_4), which is gaseous at room temperature. As excitation gas mostly O_2, N_2O, or a mixture of O_2 and N_2 is utilized. Among the numerous organosilicon precursors such as tetraethoxysilane (TEOS), tetramethoxysilane (TMOS), and hexamethyldisilazane (HMDSA), hexamethyldisiloxane (HMDSO) is most commonly used due to its high vapor pressure, low toxicity, and low cost. The chemical structure of HMDSO is depicted in Figure 2.8.

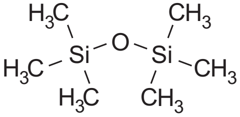

Figure 2.8: Chemical structure of precursor molecule hexamethyldisiloxane (HMDSO) [43].

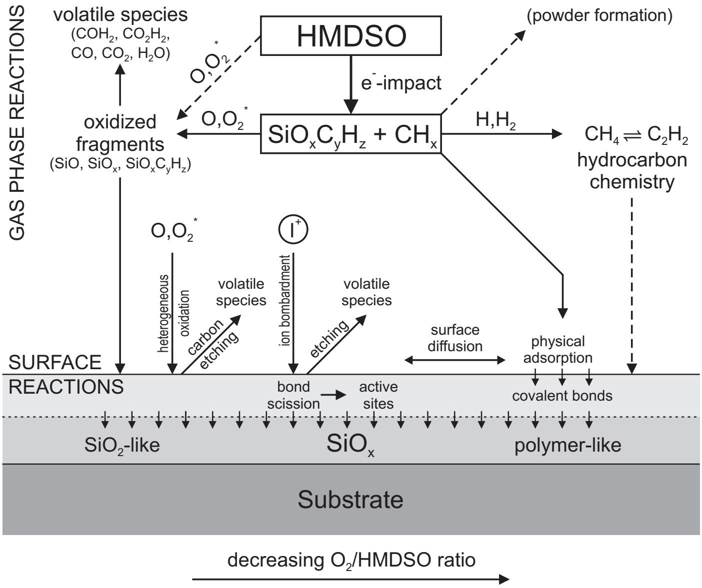

Figure 2.9: Deposition mechanism of gas phase and surface reactions for SiO_x films from O_2-HMDSO mixtures. Adapted from [44–47].

Mechanism of silicon oxide deposition

The fundamental mechanisms of SiO_x deposition were explored intensively by several techniques, especially for O_2 diluted HMDSO plasmas. This topic was addressed by d'Agostino and coworkers using actinometric optical emission spectroscopy, mass spectrometry (MS), gas chromatography with mass spectrometric detection (GC-MS) of the exhaust gas applying a cold trap, (*in situ*) XPS, and FTIR analysis [44, 45, 47]. Magni et al. proposed a schematic diagram for the reactions of the most abundant species of oxygen diluted HMDSO plasmas based on FTIR spectroscopy and mass spectrometry [46]. The most relevant findings of these investigations are schematically summarized in Figure 2.9. It was found concordantly that the HMDSO molecule is predominantly dissociated by electron impact. Preferably Si-C and C-H bonds are broken in the HMDSO molecule, since the bond energy of Si-C (4.5 eV) and C-H (3.6 eV) is lower than the bond energy of Si-O (8.3 eV) [46, 48, 49]. Depending on the feed gas composition, the carbonated radicals and the abstracted methyl radicals are directly deposited, undergo homogeneous oxidation reactions, or reactions with hydrocarbons. The fragments may then adsorb on the surface and carbonated species are oxidized by (atomic) oxygen. At high dilution conditions (i.e. O_2/HMDSO flow rate ratio $q > 10$) these heterogeneous oxidation reactions are dominating and responsible for a drastic reduction of the carbon content in the film. Depending on the kinetic energy of the impinging ions, active sites are formed by bond scission, and etching of smaller species occurs. The ion bombardment is also responsible for densification and smoothing of the growing film, which is essential for the deposition of high quality barrier films [8]. Depending on the process conditions, a third pathway leading to the formation of powder has to be mentioned. It is interesting to note that these main reaction pathways have also been found prominent for atmospheric pressure plasma deposition processes [43].

Silicon oxide diffusion barrier coatings on PP

For the deposition of barrier coatings, PP is more problematic as base material than polyesters. The deposition of SiO_x on PET, for instance, is intensely investigated in the literature. Low OTR values in the range of $0.1 - 1.0\,cm^3/m^2/d$ are reported by several authors [1, 8–11]. This corresponds to a barrier improvement factor (BIF), defined as the ratio of the TR through the uncoated to the TR through the coated substrate (TR_s/TR), for oxygen of up to 1000. For PP as substrate not as much work has been contributed. Oxygen barrier performances reported for SiO_x coated PP are much more diverse. Felts et al., Klemberg-Sapieha et al., and Agres et al. reported OTR values below $10\,cm^3/m^2/d$ for SiO_x on PP by PECVD using different precursors at very low deposition rates [20, 50, 51]. Bichler et al. achieved an OTR of $14\,cm^3/m^2/d$ by electron beam evaporation of SiO_x on PP [52], while Misiano et al. reached an OTR of $120\,cm^3/m^2/d$ in the best case using the same method [53]. Knoll et al. [21], as well as Inagaki et al. [54], found no oxygen barrier improvement of SiO_x on PP by PECVD. Inagaki therefore suggested a coupling treatment prior to deposition resulting in an OTR of

$37\,\mathrm{cm^3/m^2/d}$. Moosheimer reported an improvement in OTR from 1600 to $50\,\mathrm{cm^3/m^2/d}$ by evaporation of SiO_x on BOPP homopolymer foil [55]. The lowest OTR of $2.6\,\mathrm{cm^3/m^2/d}$ was achieved by lamination of an evaporated Al coating on low pressure plasma pretreated BOPP homopolymer to a BOPP copolymer [56]. In this work, the effect of low pressure O_2 plasma pretreatment of the BOPP foil prior to the deposition of thin films was investigated in detail. While for Al coatings on pretreated BOPP improved adhesion by more than twofold was reported, no such effect was observed for SiO_x and AlO_x coatings. Deng et al. also explored electron beam evaporation of thin AlO_x film on PP and PET foil [57]. They found a superior oxygen BIF of 24.2 for PET compared to only 2.7 for PP and ascribed this effect to the higher surface energy of PET and better wetting at the early stages of deposition. As a consequence, different growth mechanisms are observed on the two polymers for electron beam evaporation. After an initial island-like (Volmer-Weber) growth, the coating continues to grow layer-by-layer (Frank-van der Merwe) on PET, while on PP the growth continues in the initial mode creating a granular and more porous structure. Dennler et al. approved the hypothesis of the initial growth by island-coalescence for PVD methods in a comparative study of the initial stages of film growth for PVD and PECVD on different substrates [25]. Interestingly, for PECVD layer-by-layer growth is observed already at the very early stages of deposition irrespective of the substrate. They concluded that, unlike for PVD, during PECVD the polymer substrate is ‘pretreated’ (modified) by active species (atomic oxygen, UV photons, ions) immediately after plasma ignition. This increases the surface energy before appreciable deposition occurs, which presumably facilitates ‘wetting’ by the SiO_x deposit.

2.2.3 Amorphous hydrogenated carbon coatings

Carbon based coatings are very versatile due to their wide range of properties. As shown in the ternary phase diagram in Figure 2.10, their properties change as a function of the sp^2 to sp^3 ratio and the hydrogen content from graphite- and polymer-like to diamond-like [58–60]. Amorphous carbon (a-C) coatings show low friction, low roughness, high hardness, and good wear resistance [59]. Amorphous carbon with a considerable sp^3 content is frequently referred to as ‘diamond-like carbon’

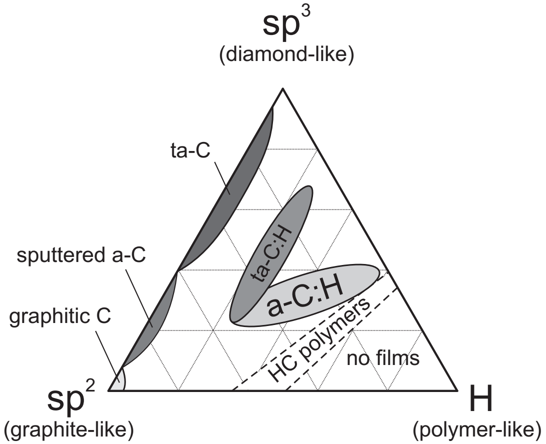

Figure 2.10: Ternary phase diagram of hydrocarbon films depending on their sp^3, sp^2, and hydrogen content [58, 59].

(DLC). For DLC coatings good biocompatibility is reported, and no adverse effect in direct contact with food for packaging applications is expected [61]. Depending on the sp^3 and hydrogen content, amorphous hydrogenated carbon (a-C:H), tetrahedral amorphous carbon (ta-C), and tetrahedral amorphous hydrogenated carbon (ta-C:H) are distinguished. Among their numerous applications are protective coatings for IR optics and hard discs, wear resistant coatings for fuel injectors and medical implants, and gas diffusion barrier coatings for food packaging. As hydrocarbon source mainly CH_4 or C_2H_2 is used for PECVD of a-C:H coatings, optionally diluted with Ar or He at a typical U_b of -100 to $-600\,\mathrm{V}$ [62–65]. Thin a-C:H diffusion barrier coatings with comparable barrier performance to SiO_x were achieved on PET with an OTR of $0.3 - 1.0\,\mathrm{cm^3/m^2/d}$, corresponding to a BIF of $60 - 150$, while for a-C:H on PP an OTR of $200\,\mathrm{cm^3/m^2/d}$, corresponding to a BIF of 100, is reported [65–67].

Properties of a-C:H coatings can be modified by incorporation of additional elements, such as F, N, O, and Si [60]. Fluorinated a-C:H (a-C:F:H) coatings are applied as hydrophobic and anti-adhesive layers, since the surface energy and the wetting behavior is influenced by F incorporation [68, 69]. The incorporation of N in a-C:H coatings reduces the internal compressive stress and lowers the content of sp^3 hybridization [70, 71]. Therefore, a-C:N:H coatings show appealing mechanical and tribological properties. Deposition of a-C:N:H films is commonly performed by PECVD from CH_4-N_2 or C_2H_2-N_2 mixtures (optionally diluted with He or Ar) at comparable U_b as for a-C:H [71–75]. For DLC films with incorporated Si and O, e.g. by the addition of HMDSO to CH_4 or C_2H_2, reduced internal stress and improved fracture toughness are reported as well as a high scratch and wear resistance and a high transparency [76–78].

2.3 Gas transport

2.3.1 Permeation through polymer films

The permeation of small molecules through flawless polymer films is generally described by the solution-diffusion model, comprising the consecutive steps of permeant solution in the polymer and activated diffusion of the permeant through the polymer, of which the latter is mostly considered to be the rate-limiting step [79, 80]. Fickian models of activated transport are frequently applied to adequately describe the permeation of ideal gases through polymers, despite thermally dependent interchain interactions and the temporary formation of interstitial spaces [81, 82]. The diffusive flux j, i.e. the amount of permeant per unit time and area, is related to the concentration gradient by Fick's first law

$$j = -D\nabla c, \tag{2.9}$$

where D is the diffusion coefficient. Fick's second law can be derived from Fick's first law and the mass balance over an infinitesimal volume element of the polymer to obtain

$$\frac{\partial c}{\partial t} = \nabla \cdot (D\nabla c) \tag{2.10}$$

or in case of isotropic conditions, where D is a scalar:

$$\frac{\partial c}{\partial t} = D\nabla^2 c. \tag{2.11}$$

If the diffusion process is the rate-limiting step, the solution step can be considered in equilibrium (first assumption of the solution-diffusion model). This holds for noninteracting gases of low molecular weight due to their low solubility in most polymers [83]. Therefore, the concentration of dissolved permeant is directly related to the partial pressure of the component i in the gas phase by Henry's law

$$c_i = Sp_i, \tag{2.12}$$

where S is Henry's solubility constant. By integration of Equation 2.9 over the polymer film thickness h_s and by applying Henry's law, a correlation for the permeant flux of component i (also referred to as the transmission rate TR) and its partial pressure difference over the film is derived:

$$j_i = -DS\frac{\Delta p_i}{h_s} = TR. \tag{2.13}$$

The product DS equals the permeability coefficient P, which is a characteristic constant for the permeant/polymer system in the case of small noninteracting molecules such as N_2, O_2, and CO_2 through most polymers. According to the activated rate theory, permeation is considered as an activated process. Therefore, the temperature dependence of P, D, and S follows Arrhenius behavior with the apparent activation energy for permeation and for diffusion, ΔE_P and ΔE_D, and the sorption enthalpy ΔH_S:

$$P = P_0 \exp(-\Delta E_P/\Re T), \tag{2.14}$$

$$D = D_0 \exp(-\Delta E_D/\Re T), \tag{2.15}$$

$$S = S_0 \exp(-\Delta H_S/\Re T). \tag{2.16}$$

Consequently, $\Delta E_P = \Delta E_D + \Delta H_S$ applies.

According to the ideal laminate theory, the permeation P_{ILT} through a series of defect-free polymeric layers is given by

$$P_{ILT} = \sum_i h_i \left(\sum_i \frac{h_i}{P_i}\right)^{-1}, \tag{2.17}$$

where h_i and P_i are the thickness and permeability of the single layers, respectively [82, 84–87].

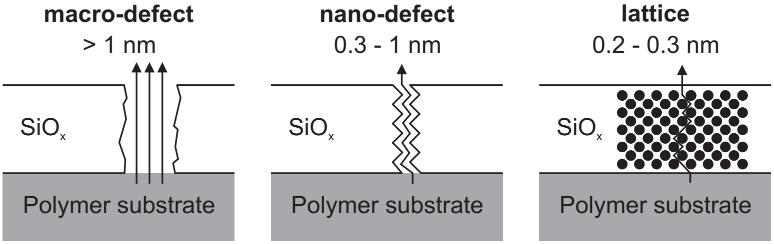

(a) Unhindered transport through macro-defects

(b) Hindered transport through nano-defects

(c) Hindered transport through the SiO_x lattice

Figure 2.11: Gas transport pathways through thin oxide/polymer composites after Roberts et al. [87].

2.3.2 Permeation through thin oxide film/polymer composites

The diffusion barrier performance of polymers can be improved significantly by the deposition of thin oxide or metal films. A BIF usually exceeding 500 is achieved on PET foil [8, 88]. Activation energies for O_2 permeation through fused silica of $92 - 290$ kJ/mol are reported [89–91]. Extrapolation of the O_2 permeability data to 25°C and a thickness typical for thin films results in an OTR of several orders of magnitude lower than the actually observed OTR values of PECVD SiO_x [30, 92, 93]. This suggests that defect free SiO_x would be virtually impermeable for O_2. The permeation through SiO_x/polymer composites is generally defect-controlled as discussed by several authors [87, 88, 93–96].

Roberts et al. proposed a model for the O_2 and H_2O transport through SiO_x gas barrier films comprising contributions from three components as illustrated in Figure 2.11: (a) unhindered transport through 'macro-defects' (> 1 nm), (b) hindered transport through 'nano-defects' (< 1 nm), and (c) hindered transport through the amorphous lattice of the oxide (interstice < 0.3 nm) [87]. The relative contribution of each component was found to depend on the size of the permeant molecule and the number and size of each class of defect. The transport of O_2

molecules is believed to occur mainly through macro-defects [82] due to its relatively large diameter of 0.32 nm [97]. The formation of macro-defects is ascribed to incomplete coverage at the early stages of the deposition process and to impurities on the substrate (e.g. dust, protrusions from fillers or anti-block particles), while nano-defects may arise along grain boundaries.

Further insight into the prevailing transport mechanisms can be gained by the activated rate theory. According to this approach, the temperature dependence of permeation of noninteracting gases through both $\mathrm{SiO_x}$ and polymers below their glass transition temperature follows Arrhenius behavior as indicated by Equation 2.14. Since the permeance is defined as the permeability divided by the substrate thickness ($\Pi = P/h_s$), this applies also for the permeance Π [82, 95]:

$$\Pi(T) = \Pi_0 \exp(-\Delta E_P/\Re T). \tag{2.18}$$

Here, Π_0 is a preexponential factor characteristic to the system. If a constant pressure difference is applied during measurement, TR is expected to show Arrhenius-type temperature dependence as well with identical ΔE_P values, since $\Pi = TR/\Delta p$ [57]. For the unhindered gas transport through macro-defects in an otherwise impermeable oxide coating, no rise in ΔE_P is expected over the value of the uncoated polymer substrate. For the other limiting case, a macro-defect free barrier coating, ΔE_P values in the range of fused silica as reported above are expected. Therefore, conclusions can be drawn regarding the presence of macro-defects from the apparent activation energy ΔE_P. For the permeation of O_2 through $\mathrm{SiO_x}$/polymer composites, identical ΔE_P values are found as for the uncoated polymer substrates by most authors [57, 82, 95, 98]. For $\mathrm{SiO_x}$/PC an increasing ΔE_P with increasing coating thickness h_c is reported, which is ascribed to the hindered transport through nano-defects of $0.5 - 0.6$ nm showing an increasing tortuosity with increasing h_c [99]. For PET coated with $\mathrm{SiO_x}$ on both sides ($\mathrm{SiO_x}$/PET/$\mathrm{SiO_x}$), Tropsha and Harvey observed a clear increase in ΔE_P up to the range of fused silica and concluded that permeation occurs also through the oxide matrix in this case due to decoupling of the (rare) defects [82]. On the contrary, da Silva Sobrinho et al. reported no increase in ΔE_P for the 'same' composite of comparable or even higher barrier performance [98].

While defects in metallic coatings can be detected directly by means of OM or SEM, the visualization of defects in transparent oxide coatings is more difficult. To overcome this problem, a technique based on reactive ion etching (RIE) was developed [93, 98]. The defective coating is exposed to atomic oxygen in a low pressure O_2 plasma. Cavities are etched in the polymer through coating defects, which can be examined by OM or SEM. Since the undercut region can be assumed to grow linearly, it is possible to derive the initial defect size distribution additionally to the defect density n_d, which is defined as the number of defects per area. Unfortunately, the applicability of this approach is limited in the case of temperature-sensitive substrate materials. Even at low MW/RF power, the formation of cracks in the oxide coating is inevitable due to the high thermal expansion of the substrate during RIE. Alternatively, wet chemical etching can be applied to etch cavities in the polymer underneath the defects in oxide coatings. For PET substrate H_2SO_4 can be used [30]. In principle, the chemical etching technique is also applicable for temperature-sensitive substrate materials, but it shows the disadvantage that it is impossible to deduce original defect sizes or defect size distributions from the defect patterns as the etched hole in the polymer underneath the defect is considerably larger. Minimal defect densities of about 80 and $70\,\mathrm{mm}^{-2}$, in exceptional cases even down to $5\,\mathrm{mm}^{-2}$, were determined by RIE for PECVD SiO_2 and SiN on PET with excellent barrier performance. The maximum in the (Gaussian shape) defect size distribution was found at a radius of $0.6\,\mu$m [98]. For evaporated Al coatings on PET, defect densities of 25 to $400\,\mathrm{mm}^{-2}$ are reported with a maximum in defect size distribution at $1-2\,\mu$m [96].

The calculation of the steady state permeation through defects in an otherwise impermeable coating on a polymer substrate was addressed analytically and numerically for circular, rectangular, and other defect geometries by several authors [85, 86, 94, 96, 98, 100]. It was concluded that many small and compact defects are more fatal in comprising barrier performance than a few larger ones of same total defect area. Furthermore, for a given defect density and size distribution, the permeability of the polymer adjacent to the defects is decisive for the overall permeability of the composite [94]. For the case that the substrate thickness exceeds the typical defect size, the permeability is independent of the substrate thickness.

In their theoretical approach, based on the solution of Laplace's equation, Rossi and Nulman derived two limiting cases for the amount of permeant per unit time and defect hole $j(r, h_s)$ as a function of the substrate thickness h_s and the defect radius r assuming a cylindrical defect shape [86]:

$$j(r, h_s) = D\frac{\pi r^2}{h_s}\Phi_0 \qquad h_s \ll r \tag{2.19}$$

$$j(r, h_s) = 4 \cdot D \cdot r \cdot \Phi_0 \qquad h_s \gg r \tag{2.20}$$

The surface coverage Φ_0 can be derived from the transmission rate measurement of the bare substrate applying Equation 2.19. Here, $h_s \ll r$ applies, as in this case r is the size of the permeation cell aperture. A similar approach was followed to calculate the residual transmission rate (TR) through $\mathrm{SiO_x}$ on PET [9]. For this case, $j = TR_s$ and $\pi r^2 = A_0$, where TR_s is the TR of the bare substrate and A_0 is the area of the permeation measurement cell:

$$\Phi_0 = \frac{j \cdot h_s}{\pi r^2 \cdot D} = \frac{TR_s \cdot h_s}{A_0 \cdot D}. \tag{2.21}$$

The TR through the coating/substrate composite may then be calculated from Equation 2.20 by multiplication with the defect density n_d, since $h_s \gg r$ is fulfilled in this case. Here, sufficient separation of the defects from each other is assumed so that interactions can be neglected. The surface coverage Φ_0 can then be replaced by Equation 2.21 and a simple correlation between TR and the defect density n_d is obtained:

$$TR(r, h_s, n_d) = j(r, h_s) \cdot A_0 \cdot n_d = 4 \cdot TR_s \cdot h_s \cdot r \cdot n_d. \tag{2.22}$$

This expression contains only the substrate thickness h_c, the (average) defect size r, and the transmission rate of the bare substrate TR_s as additional quantities. It is noteworthy that the expression for TR is independent of the diffusion coefficient D and the permeation cell area A_0.

2.4 Mechanical properties of thin films

2.4.1 Internal stress

Internal stresses are inherent to most coating/substrate composites due to differences in thermomechanical properties. Since the internal stress influences coating performance, particularly the adhesion of thin oxide films, attention should be paid to the internal stress state. The main components of the internal stress generated during deposition of thin oxide coatings on polymers are the thermal stress, the intrinsic stress, and stress originating from the absorption of water [101–103]:

$$\sigma_i = \sigma_{i,th} + \sigma_{i,intr} + \sigma_{i,w}. \tag{2.23}$$

The thermal component of the internal stress arises from the mismatch in thermal expansion of the coating and the substrate according to

$$\sigma_{i,th} = \frac{E_c}{(1-\nu_c)} \int_{T_1}^{T_2} [\alpha_s(T) - \alpha_c(T)]\,\mathrm{d}T, \tag{2.24}$$

where α_s and α_c are the coefficients of linear thermal expansion (CLTE) of the substrate and the coating [12, 102, 104]. E_c and ν_c are Young's modulus and Poisson's ratio of the coating. Elevated temperatures are often inevitable during processing and thermal stresses are induced during subsequent cooling due to differences in CLTE and in elastic moduli between the oxide and the polymer substrate [12]. In the case of cooling after deposition, T_1 represents the temperature at the end of the deposition process and T_2 the service temperature. Intrinsic stress $\sigma_{i,intr}$ is related to the quenched disorder state in the oxide coating (i.e. the formation of nanoscale voids in the Si-O network), which is a result of the fact that the deposition process is thermodynamically not in an equilibrium. The intrinsic stress of $\mathrm{SiO_x}$ coatings produced by PECVD or PVD methods at low temperature is mostly of compressive nature [101, 102, 105–108]. Additionally, internal stress may result from the absorption of water in the substrate or the coating.

Residual compressive stress in coating/substrate composites generates a momentum, which leads to bending (or even curling) of the composite according to Figure 2.12. Residual (moderate) compressive stress is beneficial for the durability of the coating/substrate composite for the case

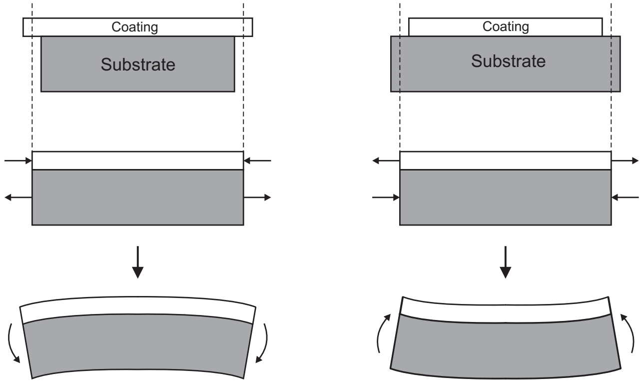

(a) Coating under residual compressive stress

(b) Coating under residual tensile stress

Figure 2.12: Curvature development of coating/substrate composites under residual compressive and tensile stress in mechanical equilibrium. Adapted from [103].

that a tensile load is applied. This is true at elevated temperatures if the thermal expansion of the substrate exceeds the expansion of the coating. In general, however, a detailed model for the prediction of the internal stress accounting for the preparation method, the process temperature, and the coating/substrate material combination is not available [103].

A correlation between σ_i and the radius of curvature r of the coating/substrate composite was derived by Stoney following a one-dimensional analysis [109]:

$$\sigma_i = -\frac{E_s h_s^2}{6 r h_c}, \tag{2.25}$$

where h_c and h_s are the coating and the substrate thickness, respectively, and E_s is the elastic modulus of the substrate. Although widely used due to its simplicity, Stoney's equation is strictly speaking only applicable for an infinitely small coating/substrate thickness ratio and disregards the effect of Poisson's ratio ν [12]. In order to overcome these insufficiencies, several expressions were proposed which also account for thicker coatings and in-plane substrate deformation as for instance the expression derived by Inoue and Kobatake [108, 110]:

$$\begin{aligned}\sigma_i = & -\frac{E_s h_s^2}{6 r h_c} \times \frac{1}{1+ab} \\ & \times \left\{ 1 + b(4a-1) + b^2 \left[a^2(b-1) + 4a + \frac{(1-a)^2}{1+b} \right] \right\},\end{aligned} \tag{2.26}$$

where $a = \frac{E_c}{E_s}$ in the case of uniaxial stress or $a = \frac{E_c}{E_s}\frac{1-\nu_s}{1-\nu_c}$ in the case of biaxial stress and $b = \frac{h_c}{h_s}$.

2.4.2 Adhesion and cohesion

The term adhesion refers to the interaction between closely contiguous surfaces of adjacent bodies, i.e. coating and substrate, and is defined as the condition in which two surfaces are held together by intermolecular forces, by mechanical anchoring, or by both together [103]. In case of thin oxide films on polymers, it is controlled by the type of interactions at the interface and the process-induced (intrinsic) stress. For PECVD derived coatings, in general high adhesion levels can be achieved due to the formation of covalent bonds and an extended interphase between the coating and the polymer. Quantitative measurement of the adhesion, especially of thin transparent oxide films, is rather difficult, and there is a lack of widely applicable adhesion test methods. Mainly three adhesion test principles are distinguished: shear, scratch, and tensile test methods [103]. The most commonly applied adhesion test methods for thin oxide films on polymers are the adhesive tape (or peel) test, the scratch test with a stylus or related (nano)indentation techniques, the simple pull-off test, and the fragmentation test. Most test methods suffer from the general drawback that a third body is introduced. For the measurement of high adhesion levels, the adhesive-tape test is additionally limited by the requirement that the tape/film bond is stronger than the film/substrate bond. Scratch tests, where a stylus or indenter is drawn over the coating surface with increasing load, are limited by the problem of visual examination of the scratch, particularly for transparent oxide coatings, and the complexity of the developed stress field in the polymer

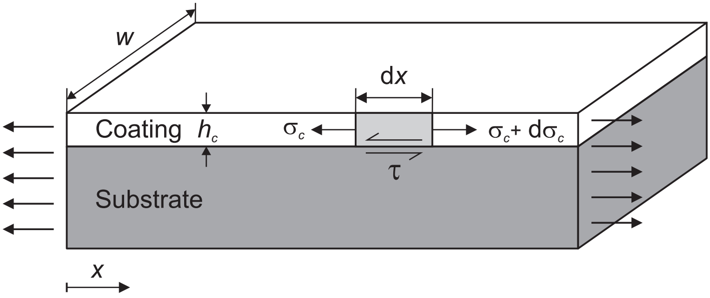

Figure 2.13: Force equilibrium of an infinitesimal coating slice of length dx, width w, and thickness h_c along the loading direction [111].

substrate. The analysis of nanoindentation tests of thin films on soft and ductile polymer substrate is delicate.

The fragmentation test method is a reliable technique to investigate the adhesive and cohesive properties of thin, brittle coatings on polymer substrates [108]. It was applied to thin brittle films on ductile metal and on polymer substrates, particularly on PET [111–114]. The method is based on the evolution of crack patterns, i.e. the crack density, with applied tensile load on the coating/substrate composite. The tensile load is directly transferred from the substrate to the coating fragments. Therefore, no third body is involved. The fragmentation of the coating depends on the stress transferability from the substrate to the coating. The critical strain at the propagation onset of the first crack in the coating, also termed crack onset strain (COS), is related to the cohesive properties of the coating. The fragmentation proceeds until a saturation crack density CD_{sat} is reached. At this point the adhesion of the fragments is not sufficient to induce further cracks. The interfacial shear strength (IFSS), which characterizes the adhesion between the coating and the substrate, can be derived from shear lag theory first described by Cox assuming a fully elastic interface [115] and later by Kelly and Tyson assuming a fully plastic interface [116]. Applying the perfectly plastic Kelly-Tyson model, the stress transfer at the coating/substrate interphase can be deduced from the force equilibrium along the loading direction of an infinitesimal coating slice of length dx, width w, and coating thickness h_c as sketched in Figure 2.13:

$$\sigma_c w h_c + \tau w \mathrm{d}x = (\sigma_c + \mathrm{d}\sigma_c) w h_c, \tag{2.27}$$

where τ is the IFSS and σ_c the stress in the coating in loading direction. This force balance can be rewritten as:

$$\frac{\mathrm{d}\sigma_c}{\mathrm{d}x} = \frac{\tau}{h_c}. \tag{2.28}$$

Under the assumptions of negligible end effects on the coating, a perfectly plastic polymer matrix, and an independent coating strength σ_{max} of the fragment length, this equation can be integrated to

$$\tau = 2h_c \frac{\sigma_{max}(l_c)}{l_c}, \tag{2.29}$$

where the critical crack spacing l_c is defined as the minimum coating length at which the maximum allowable coating stress σ_{max} can be achieved [111]. The crack density at saturation CD_{sat} is defined as the inverse fragment length $\bar{l}_{sat}$, when an increase in strain does not induce further cracks. A correlation between the fragment length $\bar{l}_{sat}$ and the critical crack spacing l_c can be obtained as an analytical solution to the problem of average crack spacing [117]:

$$\bar{l}_{sat} = CD_{sat}^{-1} = \frac{1.337}{2} l_c. \tag{2.30}$$

Applying this correlation, an expression for the IFSS τ, which is a measure for the adhesion between the coating and the substrate, can be derived from Equation 2.29 to obtain:

$$\tau = 1.337 \cdot h_c \cdot \sigma_{max} \cdot CD_{sat}. \tag{2.31}$$

The coating strength σ_{max} is related to the COS by:

$$\sigma_{max} = E_c \cdot COS. \tag{2.32}$$

A quantity for the cohesive properties of the coating, the fracture toughness G_c, can be derived from the COS and the elastic properties of the coating, assuming that it is equal to the steady state energy release rate

(ERR) G_{ss} at COS following the approach of Beuth as also applied by Andersons et al. [118, 119]:

$$G_c = G_{ss} = \frac{\pi}{2}\bar{E}_c \cdot h_c \cdot COS^2 \cdot g(\alpha_{Du}, \beta_{Du}), \tag{2.33}$$

where

$$\bar{E}_c = \frac{E_c}{1-\nu_c^2} \tag{2.34}$$

is the plane strain elastic modulus of the coating and g is a function of Dundurs' parameters α_{Du} and β_{Du} [120], which describe the elastic mismatch of the coating/substrate system. In the case of plane strain problems

$$\alpha_{Du} = \frac{\bar{E}_c - \bar{E}_s}{\bar{E}_c + \bar{E}_s}, \tag{2.35}$$

where

$$\bar{E}_s = \frac{E_s}{1-\nu_s^2} \tag{2.36}$$

is the plane strain elastic modulus of the substrate. Dundurs' second parameter is approximated by $\beta_{Du} = \alpha_{Du}/4$. This simplified approximation is applicable in the case of plane strain for many technically relevant material combinations [121].

Fracture analysis of multilayered coatings, i.e. a brittle thin film on a deformable substrate with a soft elastic-plastic interlayer, was performed by McGuigan et al. applying an elastic-plastic shear lag model [122]. They found that the onset of failure is controlled by the COS of the brittle layer. A low CD_{sat} is obtained for a low interlayer shear stress. The thickness of the interlayer does neither affect the COS nor the CD_{sat}, but the rate of crack formation.

Chapter 3

Experimental

3.1 Reactor set-up

The reactor set-up consists of a stainless steel vacuum chamber, a RF and a MW generator, gas and monomer supply, and a pumping unit as schematically shown in Figure 3.1. The vacuum chamber with an inner diameter of 160 mm and a height of 1078 mm is double-walled to enable wall heating with a thermostat. This is essential to prevent condensation of the precursor at the reactor wall. The deposition of thin films on flat substrates is performed on a RF biased substrate holder (RBS 150/100, JE PlasmaConsult GmbH, Germany). The RF powered electrode plate of the substrate holder with a diameter of 140 mm is water-cooled to 25°C to prevent substrate heating. Flat substrates are fixed with a clamping ring on the electrode plate to provide good thermal contact. For the deposition of 3D substrates, stainless steel electrodes are screwed on the electrode plate of the substrate holder. The geometry of these electrodes is adapted to the food container geometry for inside and outside coating, respectively. Drawings of the adapted electrodes are shown in Figure A.1 in the Appendix. A dark space shield is mounted at the backside of the RF powered electrode plate to avoid the generation of a undesired secondary plasma zone below the electrode plate. It is grounded and positioned with a gap to the electrode plate, which is small enough to prevent the ignition of a plasma at typical pressures used for PECVD.

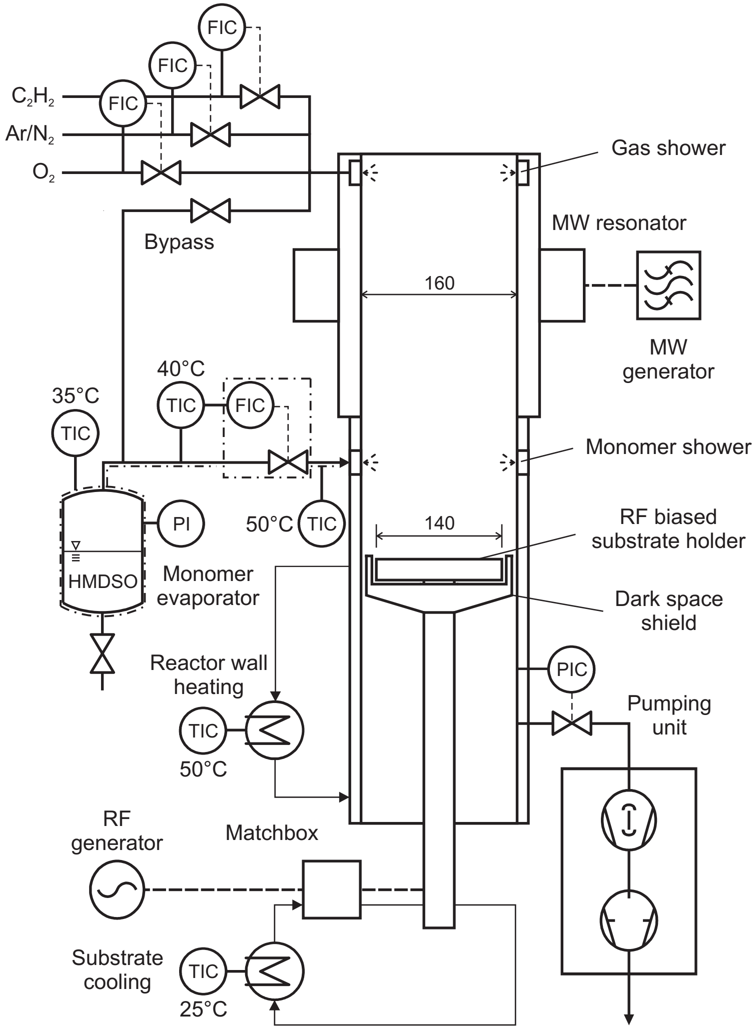

Figure 3.1: Scheme of the plasma enhanced chemical vapor deposition reactor set-up.

The substrate holder is capacitively coupled to a 13.56 MHz RF generator (Cesar 1310, Dressler HF-Technik GmbH, Germany) with a maximum RF power of 1000 W via a matching network. The gamma type matching network allows RF power coupling of up to 300 W and consists basically of two variable capacitors and an inductance. A schematic diagram of a matching network is shown in Figure A.3 in the Appendix. By manually adjusting the capacitors of the matching network, the impedance of the plasma load is matched to the resistive RF generator output impedance of 50 Ω. Thus, the reflected RF power is minimized. The impedance of the plasma load depends on the process conditions, mainly on the pressure, the gas mixture, the reactor geometry, as the reactor wall represents the grounded counter electrode to the RBS, and the RF cable connectors.

The reactor is additionally equipped with a slot antenna plasma source (SLAN I, JE PlasmaConsult GmbH, Germany) powered by a 2.45 GHz MW generator (GMP 60 KE/DC, SAIREM, France) in remote configuration. In this work, the MW source was only used for preliminary pretreatment experiments, since for the deposition of diffusion barrier coatings the bias voltage of the RF plasma proved to be advantageous [30, 123]. Therefore, a more detailed description of the MW plasma source is not given here.

The precursor HMDSO is evaporated in a cylindrical vessel, which is heated by an electrical heating tape to 35°C. This temperature corresponds to a vapor pressure of approximately 96 mbar [124]. A bypass enables the evacuation of the monomer evaporator in case of air intrusion, e.g. after refilling of monomer. The monomer is fed through a stainless steel tubing to the reactor. The mass flow is controlled by a MKS mass flow controller (type 1179B, MKS Instruments, USA), which is calibrated for HMDSO in a flow rate range of 0.2 − 20 sccm (cm^3 (STP)/min). The flow controller is heated to 40°C as well as the tubing to the low controller. The tubing between the HMDSO mass flow controller and the reactor is heated to a higher temperature of 50°C to avoid condensation. The monomer is then distributed in the reactor through a gas shower 150 mm above the substrate holder. The gas shower consists of 24 holes of 0.6 mm in diameter, which are equally distributed on the circumference of the reactor wall and directed downwards under an angle of 45°. O_2, N_2, Ar, and C_2H_2 are introduced at the top of the reactor via a gas shower with 10 holes of 1 mm in diameter. Mass flow rates are controlled by MKS mass flow controllers of type 1179A and B (MKS Instruments, USA) with a range of $5-500\,\mathrm{sccm}$ for O_2, $0.7-73\,\mathrm{sccm}$ for N_2, $1-100\,\mathrm{sccm}$ for Ar, and $0.2-21\,\mathrm{sccm}$ for C_2H_2 connected to a MKS multi gas controller unit type 647B (MKS Instruments, USA).

The pumping unit comprises a WKP 1000 A roots pump (Pfeiffer Vacuum GmbH, Germany) with a nominal pumping speed of $1070\,\mathrm{m^3/h}$ backed by a dual stage rotary vane pump (DUO 170, Balzers AG, Liechtenstein) with a pumping speed of $170\,\mathrm{m^3/h}$, which is applied to reach a fore pressure of 4 mbar. The pressure in the reactor is measured below the substrate holder by a Baratron type 627A absolute pressure transducer and controlled by a MKS type 253B butterfly throttle valve connected to a MKS 600 series pressure controller (MKS Instruments, USA).

3.2 Materials

3.2.1 Substrates

Polypropylene (PP) and polyethylene terephthalate (PET) foil, injection molded PP discs and PP containers, as well as Si wafers were used as substrates. Deposition experiments for process optimization were performed on a 30 μm thick cast PP foil (Profol Kunststoffe GmbH, Germany) due to the shorter OTR measurement time compared to injection molded PP substrate. The average roughness was determined to $S_a < 2\,\mathrm{nm}$ by AFM on scans of $1 \times 1\,\mu\mathrm{m}^2$. A melting temperature of 161°C was measured by DSC. For the uncoated PP foil an OTR of $3061.8 \pm 315.2\,\mathrm{cm^3/m^2/d}$ was obtained by masking. As reference substrate, 12 μm thick PET foil (Mylar type A, DuPont Teijin Films) with a melting temperature of 260°C and an OTR of $87.4 \pm 0.90\,\mathrm{cm^3/m^2/d}$ was used. Injection molded PP food containers of the block copolymer resin Clyrell EC440P and of the copolymer Metocene RM1099 (LyondellBasell AF S.C.A. Industries, The Netherlands) of 400 μm thickness and a dimension of $96 \times 96 \times 25\,\mathrm{mm^3}$ were used as 3D model substrate. Furthermore, injection molded discs with a diameter of 120 mm and a thickness of 400 μm were produced of the same PP resins under identical injection molding process conditions to disentangle the effect of the 3D geometry and the PP material properties. For coating thickness measurements by means of ellipsometry and profilometry as well as for FTIR spectroscopy, polished Si(100) wafers (POWATEC GmbH, Switzerland) of 700 μm thickness were used.

3.2.2 Chemicals

The purity and the molar mass M of the applied process gases for PECVD (Pangas AG, Switzerland) and the precursor HMDSO (Fluka, Switzerland) are given in Table 3.1. For OTR measurements, O_2 (Pangas AG, $\geq$ 99.999%) and forming gas 5 (Pangas AG, 5% H_2 in 95% N_2) were used. FTIR spectroscopy was performed while purging the instrument with N_2 (Pangas AG, $\geq$ 99.999%). For chemical etching and defect density analysis of SiO_x on PP, a mixture of sulfuric acid (H_2SO_4, 95 – 98%, Sigma-Aldrich Chemie GmbH, Switzerland), (ortho-)phosphoric acid (H_3PO_4, 85%, Merck KGaA, Germany), and potassium permanganate ($KMnO_4$, Schweizerhall Chemie AG, Switzerland) was applied, while on PET only sulfuric acid (95 – 98%, Sigma-Aldrich Chemie GmbH, Switzerland) was used.

Table 3.1: Purity and molar mass of process chemicals.

Chemical	Purity [%]	M [g/mol]
O_2	$\geq$ 99.999	31.9989
N_2	$\geq$ 99.999	28.0134
Ar	$\geq$ 99.999	39.9481
C_2H_2	$\geq$ 99.6 (solvent free)	26.0375
HMDSO	$\geq$ 98.5	162.3782

3.3 Experimental procedure and process conditions

Prior to deposition experiments, the equipment (i.e. the reactor wall, the HMDSO mass flow controller, the HMDSO feed line, and the pressure transducer) was heated up for at least two hours. The PP foil was cleansed in an ultrasonic acetone bath, fixed flat on the powered electrode with good thermal contact, and blown off with Ar (Pangas AG, $\geq 99.996\%$), while the PET foil was only blown off with Ar without further cleansing. After a base pressure of $p < 1\,\mathrm{Pa}$ was reached, the process gas composition and the process pressure was adjusted and given time to equilibrate. Subsequently, the RF plasma was ignited. The reflected power was minimized to $\leq 2\,\mathrm{W}$ by adjusting the capacitors of the matching network. In order to keep the thermal load on the PP substrate low, deposition was performed discontinuously in intervals of 4 s plasma operation followed by 10 s off-time. Before aeration and removal of the sample, the reactor chamber was evacuated for at least 2 min.

3.4 Temperature measurements

The gas temperature in the plasma zone and the surface temperature of the PP substrate was measured by the fiber-optical temperature measurement system FOTEMP-Multichannel with TS2 fiber-optical probes (Polytec GmbH, Germany). The measuring principle is based on the temperature dependent band-edge shift of a GaAs crystal of 0.4 nm/K. The temperature measurement range of the device is -50 to 300°C at a resolution of 0.1°C. The accuracy is $< \pm 2$°C for the entire temperature range with a reproducibility of ± 0.2°C.

For temperature measurements within plasma process environments, fiber-optical systems are advantageous as they are resistant to reactive environments. Furthermore, they show no interference with electromagnetical fields due to their non-conducting probes. The thermal probes were positioned in the gas phase with a PEEK fixture, which allows the adjustment of the measurement position in height and the measurement of four radial positions simultaneously. A drawing of the fiber-optical thermal probe fixture is provided in Figure A.2 in the Appendix. In order to measure the temperature of the substrate surface, a thermal probe was fixed with self-adhesive Al foil on the PP substrate. Preliminary tests were conducted to estimate the influence of the direct ion bombardment on the thermal probes. Very similar temperatures were measured inside a PP plate of 4 mm thickness and when the thermal probes were fixed on the polymeric substrate, since a sheath region is formed over the polymeric substrate as well as around the polymeric thermal probes. Temperatures indicated by the polymeric probes in the gas phase may exceed the 'real' gas temperature due to an additional ion bombardment. In the gas phase, steady state temperature was reached after approximately 10 min and 95% of the steady state substrate temperature was reached after 2 min. During deposition, the substrate surface temperature was presumably below the measured values due to shorter deposition times and the application of the discontinuous deposition mode (4 s plasma operation followed by 10 s off-time).

3.5 Lacquer application

Lacquers were applied on the coatings for their mechanical protection, since this step is also intended for the industrial application of the process. To investigate the influence of an additional lacquer layer, different UV curable lacquers were sprayed manually on the coatings, immediately after removal from the PECVD reactor. Before UV curing, the samples were heated to 60°C for 10 min in a hot air oven to improve the homogeneity of the surface finish. Subsequent UV curing was performed in a home-made UV curing chamber equipped with a metal halide lamp (OSRAM Supratec HSC 400-221, OSRAM GmbH, Germany) of 460 W nominal power, thereof 90 W in the UVA range (315 – 400 nm) and 22 W in the UVB range (280 – 315 nm). The lamp was cooled by pressurized air during operation. The sample was separated from the lamp by a shutter during warm-up time (120 s). Lacquers were cured on PP foil and PP discs at a distance of approximately 0.12 m from the lamp for 120 s, while the PP containers were rotated and cured for 45 s from each of the four sides.

ORMOCER lacquer

A sol-gel derived ORMOCER® (*or*ganically *mo*dified *cer*amics) lacquer was synthesized according to the method described by Amberg-Schwab et al. [15] by base catalyzed addition of 0.213 mol 3-mercaptopropyltrimethoxysilane (MTS, 95%, Sigma-Aldrich Chemie GmbH, Switzerland) to 0.25 mol 1,1,1-tris-(hydroxymethyl)propan triacrylate (tech. grade, Sigma-Aldrich Chemie GmbH, Switzerland) in 250 ml ethyl acetate. Subsequently, the alkoxy groups were hydrolyzed by slowly adding 1 mol of deionized water ($\approx$ 70% of the stoichiometric amount of hydrolyzable alkoxy groups) while stirring at 15°C. After evaporation of 175 ml ethyl acetate, 0.05 mol of the photoinitiator 1-hydroxycyclohexyl phenyl ketone (99%, Sigma-Aldrich Chemie GmbH, Switzerland) were added, and the sol was filtered. Prior to lacquer application, the PECVD coatings were treated in a pure O_2 plasma for 10 s ($P_{RF} = 100\,\mathrm{W}$, $\dot{V}_{\mathrm{O}_2} = 50\,\mathrm{sccm}$, $p = 10\,\mathrm{Pa}$) to improve wetting of the ORMOCER lacquer.

Commercial lacquer

A commercially available UV curable cationic epoxy resin lacquer (HOBA Lacke und Farben GmbH, Germany) was alternatively applied. In order to reduce the viscosity, 25 wt.% ethyl acetate were added enabling the application by spraying. Best wetting was achieved directly on $\mathrm{SiO_x}$ coatings ($q = 15 - 30$) for this lacquer without pretreatment in an O_2 plasma.

Chapter 4

Film characterization methods

4.1 Oxygen transmission rate

The OTR was measured with an OX-TRAN 100 permeability tester (Mocon Inc., USA) at 50% relative humidity and 25°C according to DIN 53380. The measuring principle is illustrated in Figure 4.1. The measurement cell is divided into two sealed half cells by the test sample. Before each measurement, the sample was conditioned by purging both half cells with carrier gas (5% H_2 in 95% N_2) to desorb oxygen from the sample and the walls of the measurement chamber. The time until a steady state in residual oxygen content, mainly caused by leakage of atmospheric oxygen, is reached, varies from less than 1 h for thin foils to more than 12 h for injection molded substrates. The sensor is exposed to the carrier gas flow by switching valve V_1 when the oxygen content is low enough for its high sensitivity. Both the carrier gas and the oxygen is humidified in a bubbler. Residual oxygen in the carrier gas is removed with hydrogen over a platinum catalyst. After a constant baseline is found, carrier gas is replaced by oxygen in the upper half cell by switching valve V_2 and oxygen permeates through the test sample. The coulometric sensor contains a potassium hydroxide soaked graphite

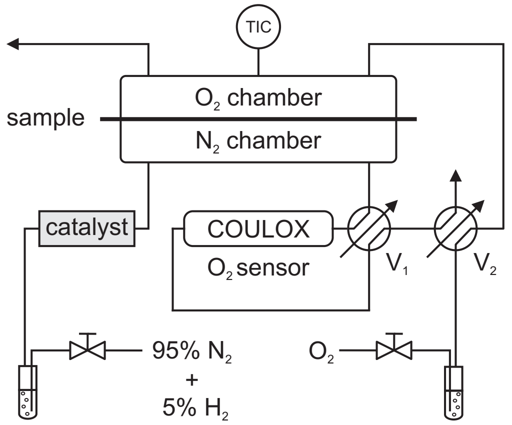

Figure 4.1: Scheme of OX-TRAN 100 permeability tester (valves V_1 and V_2 in measurement position).

cathode and a porous cadmium anode. Oxygen undergoes the following electrochemical reactions:

$$O_2 + 2\,H_2O + 4\,e^- \rightarrow 4\,OH^- \tag{4.1}$$

$$2\,Cd + 4\,OH^- \rightarrow 2\,Cd(OH)_2 + 4\,e^- \tag{4.2}$$

Accordingly, four electrons are transferred from the graphite cathode to the cadmium anode per O_2 molecule. Therefore, the measured current is directly proportional to the OTR. A current of $1.993 \cdot 10^{-6}$ A corresponds to the commonly used OTR unit of $1\,\text{cm}^3(\text{STP})/\text{m}^2/\text{d}$ for a measurement area of $100\,\text{cm}^2$ with the given values for N_A, R, and e.

The current is measured with a SCB-68 shielded I/O block over a $100\,\Omega$ measurement resistance, connected to a NI PCI-6221 data acquisition board (National Instruments Corp., USA). Data acquisition was performed with NI-DAQ 7.x and NI LabVIEW 7.1 data-logging software. The barometric pressure was measured for the correction of the OTR with a barometric precision pressure transducer (144SC0811-BARO, Sensortechnics GmbH, Germany) and recorded with the NI data acquisition system.

Resistive heating of the measurement cell allows the measurement of the OTR in the temperature range of $25 - 70$°C. To determine the apparent activation energy of permeation, OTR measurements were performed in the temperature range of $25 - 60$°C with increments of 5 K. After each increment, the OTR was repeatedly measured at a lower temperature to assure that no deterioration of the barrier performance occurred. Direct contact of the coating with the sealing grease of the measurement cell at elevated temperatures may negatively affect the integrity of the barrier coating. For OTR measurements of PP containers, a permeation test cell, adapted to the container geometry, was attached to the OX-TRAN 100 device via copper tubing.

4.2 Dry heat/sterilization tests

Dry heat tests were conducted to explore the temperature durability of the coatings on PP. Samples were consecutively heated to 80, 100, 120, and 140°C in a hot air oven (type UL 80, Memmert GmbH, Germany), the corresponding temperature was maintained for 30 min, and samples were cooled down to room temperature. The OTR was determined before exposure to elevated temperatures and after each step. Samples, coated under identical process conditions, were subjected to a standard sterilization cycle in an autoclave (Tuttnauer Systec 5075 ELVC, Systec GmbH Labor-Systemtechnik, Germany) at 121°C in 2.1 bar of steam for 30 min and the OTR was measured before and after autoclaving.

4.3 Thickness measurements

4.3.1 Variable angle spectroscopic ellipsometry

Ellipsometry is a non-destructive technique commonly used to determine the thickness and the optical properties of thin films. For samples consisting of a small number of discrete, planar, and homogeneous layers, the thickness can be derived with high accuracy down to the Ångstrom range. The functional principle is schematically shown in Figure 4.2. Xe light is linearly polarized and reflected on the sample. Upon light reflection on the sample, the p-polarizations (parallel to the plane of incidence)

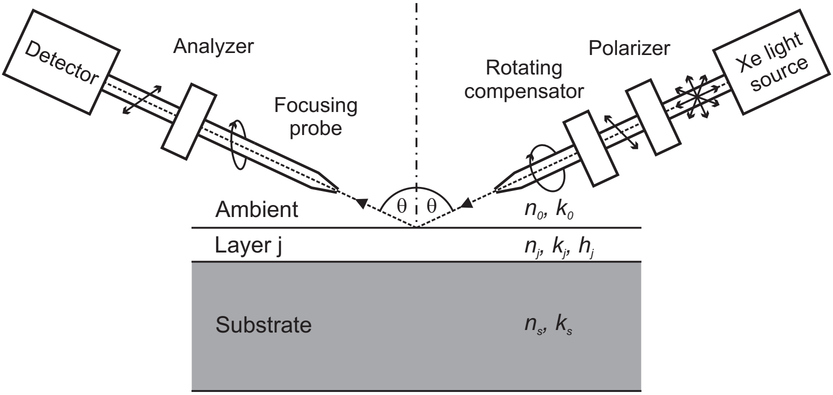

Figure 4.2: Scheme of variable angle spectroscopic ellipsometer.

and s-polarizations (perpendicular to the plane of incidence) show different changes in amplitude and phase [125]. The signal with the altered state of polarization is then analyzed and detected with a CCD camera. A rotating compensator allows shorter data acquisition times and enhanced measurement accuracy. Ellipsometry measures the amplitude ratio Ψ and the phase shift Δ between p- and s-polarizations. These two quantities are related to the ratio of the amplitude reflection coefficients for p- and s-polarization, R_p and R_s, by the fundamental equation of ellipsometry:

$$\frac{R_p}{R_s} = \tan\Psi \cdot e^{i\Delta} = f(\lambda, \theta, h_j, n_j, k_j). \tag{4.3}$$

The measured quantities, Ψ and Δ, are not directly related to the layer thickness h_j, the optical constants (refractive index n_j and extinction coefficient k_j), the angle of incidence θ, and the wavelength λ. Hence, ellipsometry is a model-based technique. The material sequence of the layers is specified within the model. The dependence of the refractive index n on the wavelength λ is approximated, for instance, by a Cauchy model:

$$n(\lambda) = A_n + \frac{B_n}{\lambda^2} + \frac{C_n}{\lambda^4}. \tag{4.4}$$

The thickness information is then deduced by regression analysis to obtain the best fit of the model to the experimental data by minimization of the mean squared error.

Coating thicknesses were determined on Si(100) wafers, which were centered on the polymer substrate during the deposition experiments, with a M-2000F variable angle spectroscopic ellipsometer (J.A. Woollam Inc., USA) at three angles of incidence (65°, 70°, and 75°) in the wavelength range of $371 - 995$ nm. The device was equipped with a focusing probe, which reduces the spot size to $25 \times 60\,\mu\text{m}^2$. At least three different spots were measured and averaged. The angles of incidence were also included in the regression analysis, since the focusing probes may slightly alter the angle of incidence. A native SiO_2 layer of the Si wafer was taken into account within the model by a first SiO_2 layer of 2.3 nm thickness. The wavelength dependence of the refractive index of the coating was approximated with a Cauchy model according to Equation 4.4 with $A_n = 1.45$, $B_n = 0.01\,\mu\text{m}^2$, and $C_n = 0.00\,\mu\text{m}^4$. Minimization of the mean squared error was performed with the WVASE32 Data Analysis software provided with the instrument. The homogeneity of the coating thickness on 3D substrates was determined on Si wafers which were attached to the container walls by double-sided sticky tape. The mass density of the coatings was calculated from the measured coating thickness and the mass, which was determined on $50 \times 50\,\text{mm}^2$ glass slides with a Mettler Toledo AX205 DeltaRange analytical microbalance (Mettler Toledo International Inc., Switzerland) with a resolution of 0.1 mg and a readability of 0.01 mg.

4.3.2 Profilometry

Reference thickness measurements were performed with a stylus profilometer (Tencor P10, KLA-Tencor, USA) on Si wafers. Prior to coating, part of the Si wafer was covered by scotch tape, which was removed before measurement to create a coating edge. On each sample a length of $3000\,\mu$m was scanned with a speed of $100\,\mu$m/s, a sampling rate of 100 Hz, and a stylus force equivalent to 10 mg. The base-level was fit with the related Tencor software (version 7.0).

4.4 Differential scanning calorimetry

The melting temperature and the heat of fusion of the PP substrates were determined by differential scanning calorimetry (DSC) with a DSC 822^{e} (Mettler Toledo International Inc., Switzerland). Approximately 4 mg of PP sample was heated from -50 to 200°C in an Al pan with a heating rate of 10 K/min. The thermogram was evaluated with the STAR^{e} software 8.01 (Mettler Toledo International Inc., Switzerland). The melting temperature was estimated from the intersection of two tangent lines on both sides of the endothermic peak.

4.5 Scanning electron microscopy

Scanning electron microscopy (SEM) was performed with a LEO 1530 Gemini (Carl Zeiss Inc., Germany). Samples were attached on the metallic sample holders with conductive double-sided adhesive carbon tape. Prior to analysis, $4-5$ nm platinum were sputter-deposited on the samples to prevent charging during SEM analysis. The working distance was varied between 2 and 12 mm and the acceleration voltage between 2 and 10 kV. Secondary electrons were collected with a SE2 detector.

4.6 Atomic force microscopy

The surface topography of uncoated and SiO_x coated PP samples was explored by atomic force microscopy (AFM) with a NTEGRA Prima AFM system (NT-MDT, Russia). Areas of $1 \times 1\,\mu m^2$ were scanned by a silicon cantilever with a force constant of approximately 5.5 N/m and a resonance frequency of 120 kHz in the semi-contact mode. Data processing was performed by applying a plane fitting algorithm with the software tool Nova RC1 (NT-MDT, Russia). The average roughness S_a was calculated from their discrete approximation according to

$$S_a = \frac{1}{KL} \sum_{i=0}^{K-1} \sum_{j=0}^{L-1} |z_{ij} - \bar{z}|, \tag{4.5}$$

where K and L denote the number of data points in x and y direction and $\bar{z}$ is the mean surface height given by:

$$\bar{z} = \frac{1}{KL} \sum_{i=0}^{K-1} \sum_{j=0}^{L-1} z_{ij}. \tag{4.6}$$

4.7 Chemical characterization

4.7.1 Fourier transform infrared spectroscopy

Fourier transform infrared spectroscopy is a common method to identify chemical bonds. This method is based on the intensity change of an infrared beam due to the excitation of vibrational modes of bonds within a molecule. Therefore, energy is absorbed at specific vibrational frequencies characteristic for a chemical bond.

FTIR spectroscopy was performed with a Spectrum BX II FTIR system (PerkinElmer, USA), equipped with a deuterated tri-glycene sulfate (DTGS) detector. For each spectrum, 64 scans were collected and averaged in the range of $600 - 4000\,\mathrm{cm}^{-1}$ at $2\,\mathrm{cm}^{-1}$ resolution. The coating thickness was adjusted to $1039 \pm 81\,\mathrm{nm}$ on Si wafers, which were positioned in the center of the PP substrate during deposition. The FTIR system was purged with N_2 20 min before and during recording of each spectrum to minimize the effect of atmospheric H_2O and CO_2. Before and after each series of measurements, spectra of the background and of an uncoated Si wafer were acquired. Spectra were recorded as transmittance T_{IR}, defined as the intensity ratio of the transmitted to the incident light, and converted to absorbance A_{IR} according to the following equation:

$$A_{IR} = -\log_{10} T_{IR}. \tag{4.7}$$

For data analysis the Spectrum v5.0.2 software (PerkinElmer, USA) was used. A base line correction algorithm was applied. The spectrum of an uncoated Si wafer was subtracted from the absorbance spectra to eliminate the effect of the substrate.

The analysis of thin coatings on polymeric substrates was performed by attenuated total reflectance (ATR) FTIR spectroscopy. The principle of this method is shown in Figure 4.3. An infrared beam is passed

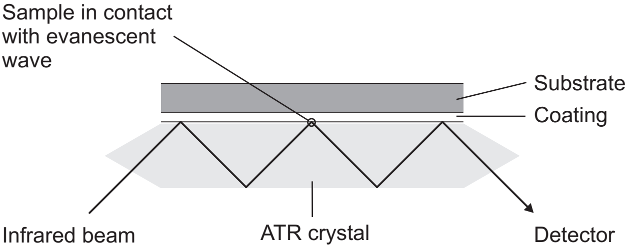

Figure 4.3: Principle of attenuated total reflectance (ATR) FTIR spectroscopy.

through a crystal and undergoes total internal reflection. This creates an evanescent wave, which extends a few microns beyond the crystal surface into the sample. Therefore, the sample has to be in direct contact with the crystal. Due to the low penetration depth of the evanescent wave of typically only $0.5 - 2\,\mu$m, a relatively high surface sensitivity is achieved by ATR FTIR spectroscopy and total absorption of IR bands is prevented.

ATR FTIR spectra were recorded with a diamond probe (MIRacle, PIKE technologies, USA). Intimate contact between the sample and the ATR crystal was assured by a high pressure clamp. The influence of the N_2/C_2H_2 flow rate ratio on the chemical structure of a-C(:N):H films with constant coating thickness of approximately 290 nm on PP foil was explored by ATR FTIR spectroscopy. The intensity of the ATR signal was corrected by multiplication with the wavenumber to account for the linear dependence of the sampling depth on the wavelength.

4.7.2 X-ray photoelectron spectroscopy

X-ray photoelectron spectroscopy (XPS), also referred to as electron spectroscopy for chemical analysis (ESCA), is a surface chemical analysis technique. It allows to determine the elemental composition as well as the chemical and the electronic state of an element. The basic principle of XPS is illustrated in Figure 4.4. The sample is irradiated by an x-ray beam and the number of the emitted photoelectrons is simultaneously

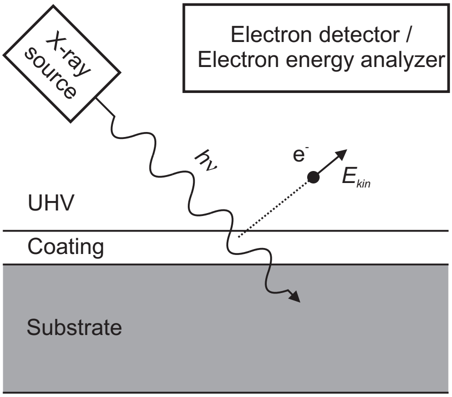

Figure 4.4: Principle of x-ray photoelectron spectroscopy.

analyzed with their kinetic energy. The photoelectrons originate from the top $1 - 10\,\mathrm{nm}$ of the surface due to the restricted path length of electrons in a solid material. The binding energy E_B of the electron is determined from the following energy balance equation:

$$E_B = E_{photon} - (E_{kin} + \Phi), \tag{4.8}$$

where $E_{photon} = h\nu$ is the photon energy, E_{kin} is the kinetic energy of the photoelectron, and Φ is the work function of the spectrometer.

XPS was performed with a Kratos Axis Nova device (Kratos Analytical, UK). The source emits monochromatic AlKα irradiation and was run at 225 W (15 kV, 15 mA). The analyzed area was $700 \times 300\,\mu\mathrm{m}^2$ in general and reduced to a diameter of $110\,\mu$m in the case of depth profiling. The photoelectrons were detected with a hemispherical analyzer, operated in the fixed-analyzer-transmission mode with a pass energy of 40 eV for the detailed spectra and 80 eV for the survey spectra (full width at half maximum (FWHM) for Ag3d$_{5/2}$ = 0.75 eV and 1.1 eV, respectively). The take-off angle was 90°. Charging of the samples was over-compensated with slow electrons from the neutralizer. Sputtering was performed using Ar ions accelerated with a voltage of 3.8 kV. The extractor current was $100\,\mu$A. For sputter cleaning of the reference samples, an area of

$3 \times 3\,\mathrm{mm}^2$ was sputtered for 30 s. For sputter depth profiling, the sputtered area was $2.5 \times 2.5\,\mathrm{mm}^2$, resulting in a sputter rate of 15 nm/min for a Ta_2O_5 reference sample. The residual pressure in the spectrometer was below $1 \cdot 10^{-6}$ Pa for the reference samples and below $5 \cdot 10^{-6}$ Pa during sputter depth profiling. The system was calibrated according to ISO 15472:2001, and the accuracy was better than ±0.05 eV. The spectra were analyzed using the CasaXPS software (V2.3.14, Casa Software Ltd., UK). Peak-shifting was corrected by referencing aliphatic carbon to 285.0 eV [126]. The peak fitting was performed after subtraction of an iterated Shirley background [127]. The quantitative composition was calculated by correcting the peak areas by the transmission function and the sensitivity factors given by Kratos assuming a homogenous compound. The FWHM was constrained to be equal in the case of peaks fitting by more than one component. A SiO_2 reference sample was prepared by wet thermal oxidation of a Si wafer at 1000°C for 7 h in water vapor and oxygen.

4.8 Mechanical analysis

4.8.1 Tensile tests

In uniaxial tensile tests, a specimen is elongated by an uniaxial load, and the elongation Δl is recorded. Results are presented as stress-strain curves, where the strain ε is defined as

$$\varepsilon = \frac{\Delta l}{l_0} \tag{4.9}$$

with the initial length l_0 of the sample. Young's modulus E_s and the tensile yield stress σ_Y are determined from the slope of the stress-strain curve in the elastic region and from the maximum after the elastic region. Tensile tests of the 30 μm PP foil were performed with a ZWICK/ROELL Z005 (Zwick GmbH & Co. KG, Germany) at a strain rate of $0.0167\,\mathrm{s}^{-1}$ on five samples of $18 \times 10\,\mathrm{mm}^2$ perpendicular and parallel to the machine direction of the PP foil, respectively. A preload of 0.01 MPa was applied prior to testing. E_s was determined between 0.5 and 1.5% strain at a lower strain rate of $0.0017\,\mathrm{s}^{-1}$.

4.8.2 Dilatometry analysis

Expansion and shrinkage behavior of uncoated PP and SiO_x/PP samples of $8 \times 40\,mm^2$, cut along and perpendicular to machine direction, was explored by dynamic mechanical analysis (DMA) with a DMA Q800 (TA Instruments, USA) in the temperature range of 25 to 135°C with a heating rate of 5 K/min and a constant load of 1 mN. The change in length of the sample was measured as a function of temperature. The CLTE was deduced from the initial linear part between 30 and 45°C.

4.8.3 Internal stress measurements

The internal stress σ_i was deduced from the radius of curvature of the substrate/coating composite by applying Equation 2.26, which was derived by Inoue and Kobatake. The radius of curvature r was determined from the maximum deflection d of $80 \times 15\,mm^2$ rectangular samples with spacing l according to:

$$r = \frac{l^2}{8d}. \tag{4.10}$$

Young's modulus of the substrate E_s was derived from tensile tests. The coating thickness h_c was approximately 200 nm. Young's moduli E_c of the coatings were estimated from E_{SiO_2}, α_{SiO_2}, and α_c according to Ashby [128]:

$$E_c = E_{SiO_2}\frac{\alpha_{SiO_2}}{\alpha_c}. \tag{4.11}$$

The CLTE values α_c of the coatings are *a priori* unknown and may change with their carbon content. Hence, these values were estimated by linear interpolation between the literature values of PECVD SiO_2 and pp-HMDSO with the C/Si ratio from XPS as the variable.

4.8.4 Fragmentation tests

Fragmentation tests were carried out with a miniature tensile tester MiniMat 2000 (Rheometric Scientific GmbH, Germany) *in situ* under an optical microscope (Olympus BX 60, Japan) equipped with videoextensometry with strain accuracy better than 10^{-3}. Rectangular samples of $8 \times 40\,mm^2$ were incrementally strained and crack patterns were analyzed in terms of crack density (CD) versus true strain. The CD was derived from the number of cracks K_i counted on L micrographs of width w at each explored strain level ε according to

$$CD = (1+\varepsilon)\sum_{i=1}^{L}\frac{K_i}{L \cdot w}, \tag{4.12}$$

where the factor $(1+\varepsilon)$ accounts for the crack opening as a first approximation [119]. In order to determine the true strain by means of videoextensometry, small ink dots were marked in a triangular arrangement on each sample at several positions. Micrographs of the ink marks were evaluated at all strain levels with the image processing software analySIS (Olympus Soft Imaging Solutions GmbH, Germany) and calculated strain values were averaged from three images at each strain level. The thickness of all investigated coatings was $119 \pm 6\,\mathrm{nm}$. The crack onset strain (COS) was derived by linear regression from the crack density versus strain data at the beginning of fragmentation.

4.9 Defect analysis

In order to derive defect densities of thin $\mathrm{SiO_x}$ films, defect patterns of chemically etched PET and PP substrate through defects in $\mathrm{SiO_x}$ coatings of varying coating thickness were analyzed. $\mathrm{SiO_x}$ coated PP samples were chemically etched by applying a mixture of 65 wt.% H_2SO_4, 32 wt.% H_3PO_4, and 3 wt.% $KMnO_4$ for 48 h at room temperature. This mixture was shown to be capable of etching PP [129]. Comparable defect patterns were obtained on PET applying H_2SO_4 within a much shorter etching time of 30 s. To stop the etching process, the samples were rinsed thoroughly with water. The etch patterns were examined by optical microscopy (OM) with a Zeiss Axioplan microscope equipped with a Zeiss AxioCam MRc digital camera (Carl Zeiss AG, Germany) and SEM. The number of defects was evaluated and averaged on multiple areas of $400 \times 400\,\mu\mathrm{m}^2$ (150 fold magnification, OM), $200 \times 200\,\mu\mathrm{m}^2$ (300 fold magnification, OM), and $50 \times 50\,\mu\mathrm{m}^2$ (2000 fold magnification, SEM).

Chapter 5

Results and discussion

The main goal of this work is to achieve diffusion barrier coatings on 3D PP substrate, which sustain exposure to elevated temperatures in an autoclave. PECVD is a versatile method with many individual adjustable parameters. The effects of different parameters on coating properties, however, may not be considered independent from each other. Moreover, preliminary experiments showed that the substrate has a major influence on the results. Transferability of results from one polymer to another may not be taken for granted [21]. As mentioned before, PP is problematic as substrate due to its high thermal expansion coefficient and its low glass transition temperature. Therefore, the first part of this chapter is dedicated to the process optimization with respect to the barrier performance over a wide range of process parameters. As a first step, thin PP foil was employed as substrate. Apart from a reduction of complexity of the problem, this greatly reduces OTR measurement time from more than 24 h to 1 − 2 h per experiment. Previous works and preliminary experiments identified the RF power, the monomer, and the oxygen flow rate as main parameters for the manipulation of coating properties [30, 123]. A pressure range of 10 − 20 Pa was found to be favorable for good diffusion barrier performance. Since temperature-sensitive materials are used as substrate, it is essential to explore occurring process temperatures. The chemical characterization of SiO_x coatings and their related mechanical properties is presented in Section 5.1.2 and 5.1.3. Apart from SiO_x, carbon-based coatings, such as a-C:H and a-C:N:H, show interesting properties, which are explored in Section 5.2. Based on these results, coating layers with good mechanical properties are combined with a layer of favorable diffusion barrier performance in a multilayer approach. The temperature durability of these multilayer coatings and their chemical composition is investigated in Section 5.3. Finally, the optimized coatings are applied to 2D and 3D injection molded PP substrates. In a last part, further optimization of process conditions for these substrates, the effect of an additional protective lacquer layer, and the coating homogeneity on a 3D model substrate is discussed.

5.1 Silicon oxide coatings

5.1.1 Influence of process parameters

The influence of the main PECVD process parameters, P_{RF}, $\dot{V}_{\mathrm{HMDSO}}$, and $\dot{V}_{\mathrm{O_2}}$, is investigated over a wide range in order to optimize diffusion barrier performance of $\mathrm{SiO_x}$ on PP substrate. The use of the composite parameter $P_{RF}/(\dot{V}_{\mathrm{HMDSO}} \cdot M)$ as a measure for the energy input per unit mass of monomer was motivated by Yasuda and described more in detail in Section 2.2.1. Since HMDSO is used as the only monomer, in the following the molar mass of the precursor M is omitted and $P_{RF}/\dot{V}_{\mathrm{HMDSO}}$ is employed as the composite parameter CP, combining P_{RF} and $\dot{V}_{\mathrm{HMDSO}}$ to a more meaningful parameter. Accordingly, the $\mathrm{O_2}$ and HMDSO volumetric flow rates, $\dot{V}_{\mathrm{O_2}}$ and $\dot{V}_{\mathrm{HMDSO}}$, are combined in a second important parameter, the $\mathrm{O_2}$/HMDSO flow rate ratio q.

Influence of the RF power and the monomer flow rate

In Figure 5.1, the OTR of $\mathrm{SiO_x}$ thin film on PP foil is shown as a function of CP for constant $q = 30$, $p = 10\,\mathrm{Pa}$, and $t_{dep} = 15 \times 4\,\mathrm{s}$. Within a wide range of P_{RF} below 200 W an improvement of diffusion barrier performance is observed with increasing CP. At $CP = 50\,\mathrm{W/sccm}$, corresponding to $4.1 \cdot 10^5\,\mathrm{J/g}$, an optimum in OTR is reached. Further increase of CP results in a weak decrease of barrier performance. A similar dependence of the OTR on CP is also found for a-C:H coatings on PET [130].

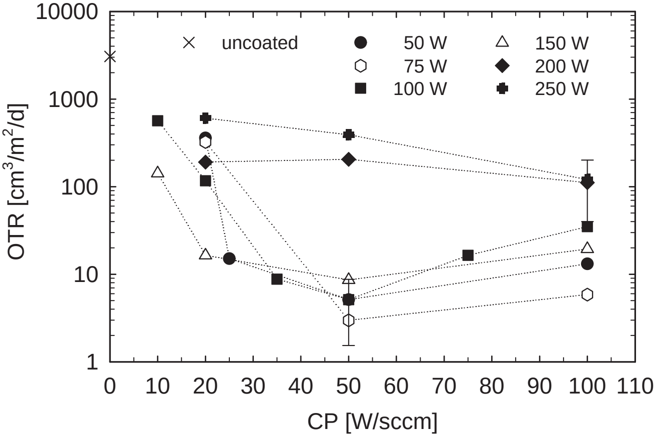

Figure 5.1: OTR as a function of the composite parameter $CP = P_{RF}/\dot{V}_{\mathrm{HMDSO}}$.

For PP substrate, an upper limit in P_{RF} of approximately 200 W is observed for good diffusion barrier performance. Possible reasons for this observation may be found in an increased thermal load and a more intense ion bombardment. Both factors are mainly dependent on P_{RF}. On less temperature-sensitive substrates, as for instance on PET, coatings with good barrier performance can be obtained for RF powers exceeding 200 W. For one representative low power and high power condition, respectively, error bars show the standard deviation of the OTR in Figure 5.1. In general, at high power conditions ($P_{RF} \geq 200\,\mathrm{W}$) a higher variability in OTR is observed (please note the logarithmic scale), accompanied by visible thermal damage of the PP substrate, i.e. the formation of folds.

The self-bias voltage U_b, which is measured between the powered electrode plate and the grounded reactor wall, mainly depends on the applied RF power as shown in Figure 5.2. The bias voltage is related to the kinetic energy of the positive ions bombarding the substrate surface. The ion bombardment is essential for the densification and smoothing of the growing film, while excessive ion bombardment causes damage of the

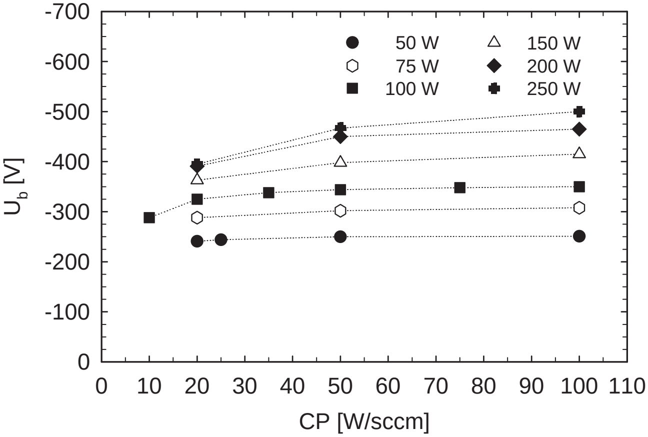

Figure 5.2: Self-bias voltage U_b as a function of the composite parameter $CP = P_{RF}/\dot{V}_{\mathrm{HMDSO}}$.

polymer substrate. Changes in $\dot{V}_{\mathrm{HMDSO}}$ seem to have a minor influence on U_b. A slight decrease in U_b is noticed with increasing $\dot{V}_{\mathrm{HMDSO}}$ (i.e. decreasing CP). This is explained by the higher total gas flow rate and the related higher energy consumption in the plasma bulk.

In Figure 5.3, the deposition rate R is plotted as a function of CP. High deposition rates, desirable for industrial application, can be achieved by increasing P_{RF} and/or $\dot{V}_{\mathrm{HMDSO}}$. However, increasing the monomer flow rate at constant power (i.e. decreasing the composite parameter) or increasing the power at constant composite parameter is only possible within limits in order to retain good barrier properties on PP as shown in Figure 5.1. As for CP, the molar mass of the monomer is omitted in the case of the conversion ratio $R/(\dot{V}_{\mathrm{HMDSO}} \cdot M)$ of monomer to polymer for plasma polymerization as introduced by Matsuda and Yasuda [41]. Hence, the conversion ratio $CR = R/\dot{V}_{\mathrm{HMDSO}}$ is employed. In Figure 5.4, the conversion ratio CR is shown as a function of CP for the deposition of $\mathrm{SiO_x}$ at constant $q = 30$. Particularly at low CP, a very similar CR is obtained for a wide range of RF powers. Interestingly, a change from an energy-deficient region, where the conversion ratio increases with in-

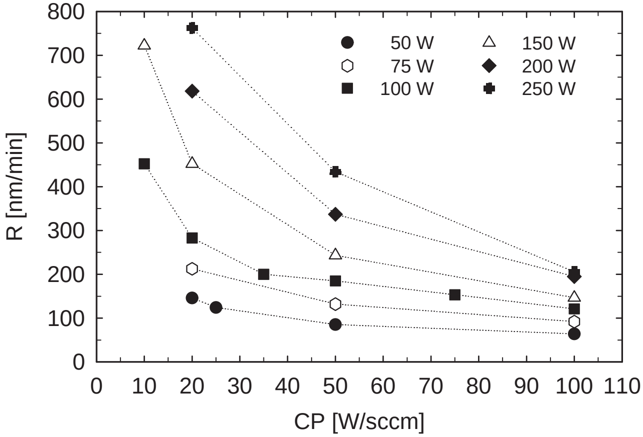

Figure 5.3: Deposition rate R as function of the composite parameter $CP = P_{RF}/\dot{V}_{\mathrm{HMDSO}}$.

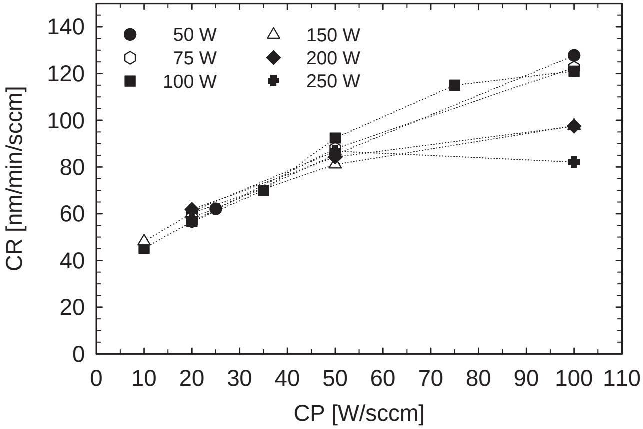

Figure 5.4: Conversion ratio $CR = R/\dot{V}_{\mathrm{HMDSO}}$ as a function of the composite parameter $CP = P_{RF}/\dot{V}_{\mathrm{HMDSO}}$.

creasing composite parameter, to a monomer-deficient region is observed at approximately 50 W/sccm for P_{RF} exceeding 100 W. This coincides with the optimal value in terms of barrier performance. For lower P_{RF}, the transition of an energy to a monomer-deficient regime seems to be slightly shifted towards higher values of CP.

Influence of the oxygen to monomer flow rate ratio

The O_2/HMDSO flow rate ratio q strongly affects the characteristics of SiO_x coatings and it may not be considered independently from P_{RF} and CP. Therefore, the influence of q on the diffusion barrier performance of SiO_x coatings is shown in Figure 5.5 for constant P_{RF} between 50 and 200 W and for $CP = 20$ and 50 W/sccm. For low $P_{RF} = 50$ W, the barrier performance is improved with increasing q and a higher CP, corresponding to a higher energy input per unit mass of monomer, is favorable. In the medium RF power range of 100 to 150 W, the influence of q is less pronounced, and accordingly low OTR values are achieved in the range of $q = 15 - 60$. For $P_{RF} = 100$ W, the dependence of the OTR is also explored for very low values of q down to 0 (pure HMDSO). For coatings deposited from pure HMDSO (pp-HMDSO), no barrier improvement is observed. A critical O_2/HMDSO ratio, which is around 10 at these conditions, needs to be overcome for a significant barrier performance improvement of more than one order of magnitude. Similar trends in OTR are reported in the literature [8, 20, 131]. At high $P_{RF} = 200$ W, the opposite behavior is observed as for $P_{RF} = 50$ W. Here, best barrier performance is achieved for a low q of 15, and a lower CP seems to be favorable. This interesting result suggests that both an increase in q and in P_{RF} have a similar effect on the coating properties. Consequently, a suboptimal RF power may be compensated by a high value of q in order to achieve a low OTR and vice versa. These findings will be discussed in more detail with regard to the effect on the chemical structure of the coatings in Section 5.1.2.

The dependence of the deposition rate R on q is shown in Figure 5.6 for $\dot{V}_{\mathrm{HMDSO}} = 2$ and 10 sccm at constant $P_{RF} = 100$ W. For both monomer flow rates, the dependence of the deposition rate on q follows a similar trend as it is also observed for the OTR at the corresponding P_{RF} of 100 W. High deposition rates are obtained for pure HMDSO exceeding

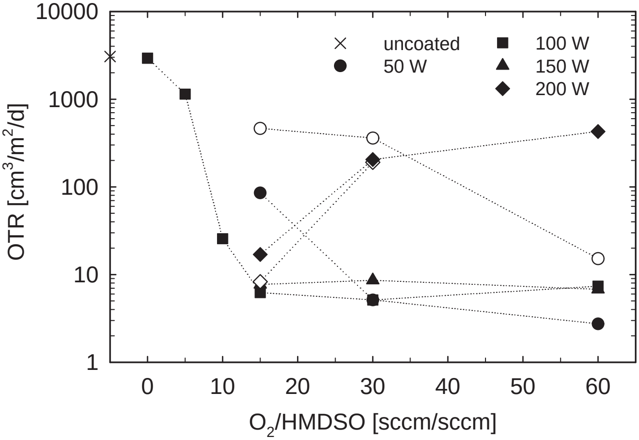

Figure 5.5: OTR as a function of the O_2/HMDSO flow rate ratio q for $P_{RF} = 50 - 200\,\mathrm{W}$ and for $CP = 50\,\mathrm{W/sccm}$ (solid symbols) and $CP = 20\,\mathrm{W/sccm}$ (open symbols).

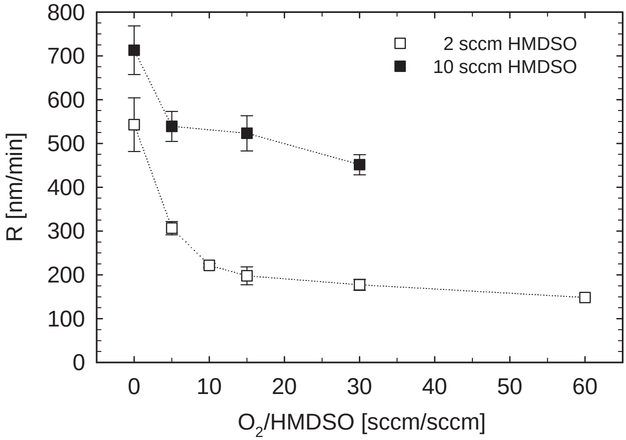

Figure 5.6: Influence of the O_2/HMDSO flow rate ratio q on the deposition rate for $\dot{V}_{\mathrm{HMDSO}} = 2$ and $10\,\mathrm{sccm}$ at constant $P_{RF} = 100\,\mathrm{W}$ and $p = 10\,\mathrm{Pa}$.

700 nm/min for $\dot{V}_{\mathrm{HMDSO}} = 10$ sccm. As q is increased to 10, the deposition rate is significantly reduced. Further increase of q results only in a minor decrease of R. The dependence of the OTR and the deposition rate on q, i.e. the existence of a critical value of q between 5 and 10, is related to changes in the gas phase and, consequently, in the film composition [45]. As will be shown in the following sections, a similar critical q is also observed in the characteristics of the mass density, the O/Si and the C/Si atomic ratio.

Process temperature

The temperature experienced by the substrate surface is very important when dealing with temperature-sensitive substrate materials such as PP. The steady state temperatures T_{gas} and T_{sub}, indicated by fiber-optical thermal probes in the gas phase and on the substrate surface, are given in Figure 5.7. Both temperatures rise considerably as P_{RF} is increased from 100 to 200 W. At high P_{RF}, the thermal load on the substrate

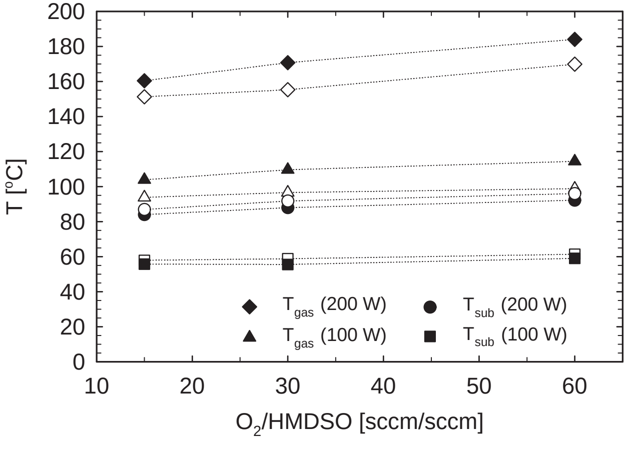

Figure 5.7: Gas phase and substrate temperature, T_{gas} and T_{sub}, as a function of the O$_2$/HMDSO flow rate ratio q for $P_{RF} = 100$ W, $\dot{V}_{\mathrm{HMDSO}} = 2$ sccm and $P_{RF} = 200$ W, $\dot{V}_{\mathrm{HMDSO}} = 4$ sccm. Open symbols denote corresponding temperatures without the addition of HMDSO.

becomes the limiting factor for the barrier performance as observed in Figure 5.1 and 5.5. Despite cooling of the RF electrode, the temperature of the substrate surface rises due to the low heat conductivity of PP. An increase of the O_2 content in the gas mixture results in an additional rise of the substrate temperature. This effect is more noticeable at high P_{RF}. An even more pronounced rise in T_{sub} with increasing oxygen content is reported in the literature if the substrate holder is not cooled [132]. The temperature characteristics explain the observed deterioration of barrier performance at high P_{RF} and high q in Figure 5.5. Accordingly, T_{sub} rises slightly if the monomer flow is completely shut off at otherwise unchanged conditions (open symbols in Figure 5.7). On the contrary, a lower T_{gas} is experienced by the thermal probes without the addition of monomer, since the oxidative gas-phase reactions of the monomer exhibit exothermic character [133].

Influence of discontinuous deposition

The influence of the discontinuous deposition mode, which is applied to keep the thermal load on the PP substrate low, is illustrated in Table 5.1 for two different sets of process parameters. Corresponding OTR results are compared for PP and PET foil. On PET, a low OTR of $0.3 - 0.5\,\mathrm{cm^3/m^2/d}$ is achieved for a wide range of P_{RF} and $\dot{V}_{\mathrm{HMDSO}}$, regardless of whether discontinuous ($15 \times 4\,\mathrm{s}$ plasma operation followed by $10\,\mathrm{s}$ off-time) or continuous ($60\,\mathrm{s}$) deposition is applied. However, continuous deposition at a high P_{RF} of 200 W (condition 2a) causes severe thermal damage of the PP substrate. Reducing the thermal load by applying discontinuous deposition and/or by lowering P_{RF} results in a low OTR of $5 - 8\,\mathrm{cm^3/m^2/d}$ on PP. This corresponds to a BIF of approximately 500, which is comparable to the best BIF achieved on PET at same process conditions. Therefore, discontinuous deposition is indispensable at high P_{RF}, while for lower P_{RF} the advantage of discontinuous deposition is diminishing. For reasons of comparability, OTR values in the preceding sections are all reported for the discontinuous deposition mode.

Table 5.1: Coating thickness h_c, average roughness S_a, and OTR of uncoated and $\mathrm{SiO_x}$ coated 30 μm PP and PET foil with corresponding deposition parameters.

	P_{RF} [W]	$\dot{V}_{\mathrm{HMDSO}}$ [sccm]	q [-]	t_{dep} [s]	h_c [nm]	S_a [nm]	OTR [$\mathrm{cm^3/m^2/d}$]	
						PP	PP	PET
	-	-	-	-	-	1.7	3061.8	86.2
1a	100	2	30	60	159	-	6.9	0.5
1b	100	2	30	15×4	177	1.9	5.1	0.3
2a	200	10	15	60	539	-	n.a.[a]	0.3
2b	200	10	15	15×4	670	3.2	8.3	0.3

[a] Thermal damage of PP substrate

Morphological analysis

The average roughness determined by AFM on $1 \times 1\,\mu$m scans is also reported in Table 5.1 for the uncoated and $\mathrm{SiO_x}$ coated PP foil. For a more profound statistical evaluation, several more scans would clearly be necessary. Good reproducibility with a deviation in S_a of 0.2 nm is observed for the uncoated PP foil. Atomic force micrographs of uncoated and $\mathrm{SiO_x}$ coated PP foil are compared in Figure 5.8. The process parameters according to condition 1b and 2b (discontinuous deposition) are applied as reported in Table 5.1. For the $\mathrm{SiO_x}$ coating deposited at condition 1b, no significant increase in roughness over the value of the uncoated PP foil is observed with $S_a < 2$ nm as shown in Figure 5.8(b). For a higher P_{RF} and $\dot{V}_{\mathrm{HMDSO}}$ (condition 2b), a higher average roughness of 3.2 nm is obtained with a more columnar-like structure as seen in Figure 5.8(c). This effect may be related to the enhanced deposition rate at condition 2b reducing the smoothing effect of the surface diffusion of adatoms.

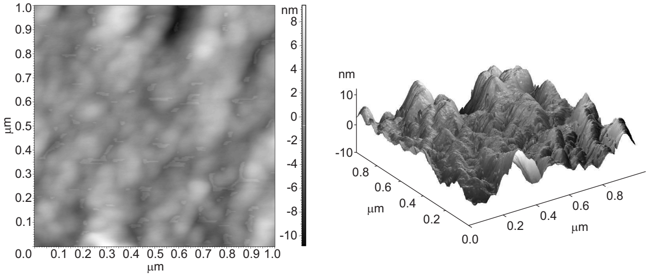

(a) uncoated PP foil, $S_a = 1.7\,\text{nm}$

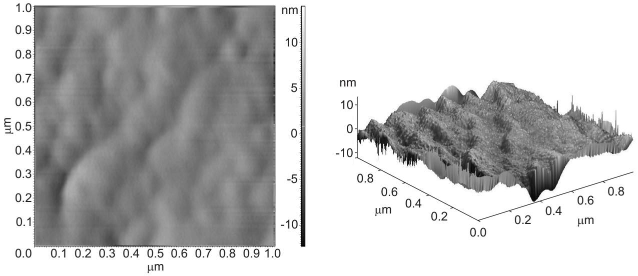

(b) SiO_x coated PP foil at condition 1b ($P_{RF} = 100\,\text{W}$, $\dot{V}_\text{HMDSO} = 2\,\text{sccm}$, $q = 30$, $t_{dep} = 15 \times 4\,\text{s}$), $S_a = 1.9\,\text{nm}$

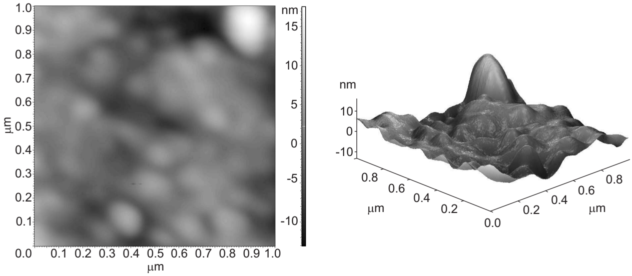

(c) SiO_x coated PP foil at condition 2b ($P_{RF} = 200\,\text{W}$, $\dot{V}_\text{HMDSO} = 10\,\text{sccm}$, $q = 15$, $t_{dep} = 15 \times 4\,\text{s}$), $S_a = 3.2\,\text{nm}$

Figure 5.8: Atomic force micrographs of $30\mu\text{m}$ PP foil uncoated and with SiO_x coatings at different conditions.

5.1.2 Chemical characterization

Fourier transform infrared spectroscopy

To explore the influence of CP on the chemical structure of $\mathrm{SiO_x}$ films, corresponding FTIR spectra of the $600-4000\,\mathrm{cm^{-1}}$ range are compared in Figure 5.9 and 5.10. In Figure 5.9, CP is varied by changing $\dot{V}_{\mathrm{HMDSO}}$ at constant $P_{RF} = 100\,\mathrm{W}$, whereas in Figure 5.10 CP is varied by changing P_{RF} at constant $\dot{V}_{\mathrm{HMDSO}} = 2\,\mathrm{sccm}$. Very similar trends are observed in both series of spectra. Peaks near 1065 and $800\,\mathrm{cm^{-1}}$ rise with increasing CP, which are characteristic for Si-O stretching and bending vibrations of the Si-O-Si bond, respectively. Regardless of whether CP is increased by lowering $\dot{V}_{\mathrm{HMDSO}}$ or by increasing P_{RF}, the Si-O stretching peak width is narrowed and the peak position is shifted towards higher wavenumbers ($\dot{V}_{\mathrm{HMDSO}} \searrow$: $1052 \rightarrow 1068\,\mathrm{cm^{-1}}$ and $805 \rightarrow 811\,\mathrm{cm^{-1}}$; $P_{RF} \nearrow$: $1061 \rightarrow 1069\,\mathrm{cm^{-1}}$ and $804 \rightarrow 813\,\mathrm{cm^{-1}}$). This peak position shift is induced by a change in the Si-O-Si bond angle due to a densification of the $\mathrm{SiO_x}$ network [24]. This effect is accompanied by a more $\mathrm{SiO_2}$-like character of the film [134]. As CP is increased, the Si-O-Si peak position approaches the peak position of thermally grown $\mathrm{SiO_2}$ at approximately $1080\,\mathrm{cm^{-1}}$ [135]. These tendencies are accompanied by decreasing absorptions at 3350 and $925\,\mathrm{cm^{-1}}$ that are assigned to OH stretching and bending vibrations in associated Si-OH species [136, 137]. The intensity of the absorption related to isolated Si-OH groups at $3650\,\mathrm{cm^{-1}}$ seems to remain constant. Similar behavior as for associated silanol species is observed for Si-H at approximately $2250\,\mathrm{cm^{-1}}$. These functionalities are terminal bonds representing cleavages in the dense $\mathrm{SiO_2}$ network and, therefore, deteriorate barrier performance of the film [138]. The organic character of the films is clearly reduced with increasing CP. The bending and stretching vibrations of $\mathrm{Si(CH_3)_x}$ at 880 and $1270\,\mathrm{cm^{-1}}$ decrease or even diminish for $CP > 50\,\mathrm{W/sccm}$. Additional bending vibrations of $\mathrm{Si(CH_3)_x}$ at 810 and $840\,\mathrm{cm^{-1}}$ are presumably superimposed by the broad Si-O bending vibration at $800\,\mathrm{cm^{-1}}$. Similar peak intensity variations are observed for C=O ($1700\,\mathrm{cm^{-1}}$), C-H asymmetric stretching in $\mathrm{CH_3}$ ($2960\,\mathrm{cm^{-1}}$), and $\mathrm{Si\text{-}(CH_2)_x\text{-}Si}$ ($1400\,\mathrm{cm^{-1}}$) [137]. High contents of carbon containing species as well as Si-OH and Si-H groups were found to deteriorate barrier performance [20, 131]. Interestingly, absorptions of $\mathrm{CO_2}$ at $2340\,\mathrm{cm^{-1}}$ are only evident for $CP > 50\,\mathrm{W/sccm}$. At these

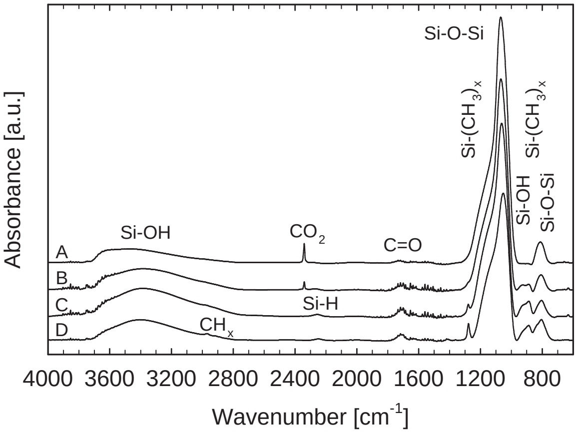

Figure 5.9: FTIR spectra of $\mathrm{SiO_x}$ coatings with varied composite parameter $CP = P_{RF}/\dot{V}_{\mathrm{HMDSO}}$ by changing $\dot{V}_{\mathrm{HMDSO}}$ at constant $P_{RF} = 100\,\mathrm{W}$. (A) 100 W/sccm, (B) 50 W/sccm, (C) 20 W/sccm, (D) 10 W/sccm.

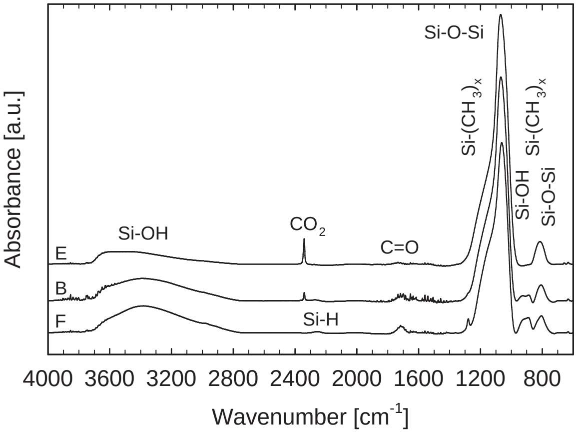

Figure 5.10: FTIR spectra of $\mathrm{SiO_x}$ coatings with varied composite parameter $CP = P_{RF}/\dot{V}_{\mathrm{HMDSO}}$ by changing P_{RF} at constant $\dot{V}_{\mathrm{HMDSO}} = 2\,\mathrm{sccm}$. (E) 75 W/sccm, (B) 50 W/sccm, (F) 25 W/sccm.

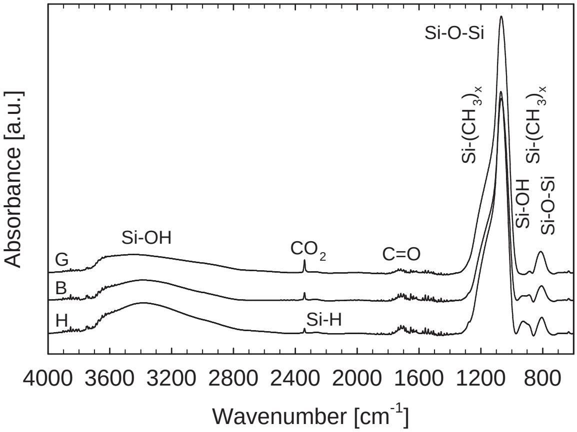

Figure 5.11: FTIR spectra of SiO_x coatings with simultaneous variation of P_{RF} and $\dot{V}_{\mathrm{HMDSO}}$ at constant $CP = P_{RF}/\dot{V}_{\mathrm{HMDSO}} = 50\,\mathrm{W/sccm}$. (G) 150 W, 3 sccm, (B) 100 W, 2 sccm, (H) 50 W, 1 sccm.

conditions, CO_2 is formed and incorporated in the growing film. Of the two characteristic bands for CO_2 at 2360 and 2340 cm^{-1} only the band at the lower wavenumber (p branch) is evidenced. This indicates that CO_2 is confined to small voids in the Si-O-Si network, hindering the rotation of the CO_2 molecule [139]. The fact that this band is only evident for $CP \geq 50\,\mathrm{W/sccm}$ indicates that a certain energy per unit mass of monomer needs to be overcome for sufficient fragmentation of the monomer molecule and oxidation of its methyl groups to form CO_2.

Spectra of films deposited at constant $CP = 50\,\mathrm{W/sccm}$ by simultaneously increasing P_{RF} and $\dot{V}_{\mathrm{HMDSO}}$ remarkably resemble each other as shown in Figure 5.11. Absorptions of CO_2 are also observed for the lowest applied P_{RF} of 50 W. The peak position of the Si-O stretching vibration in Si-O-Si (at 1065 cm^{-1}) is not shifted significantly. Nevertheless, a slightly more organic character (shoulder of Si-$(CH_3)_x$ at 1270 cm^{-1}) and a higher content of associated silanol species, at 3350 and 925 cm^{-1}, is evidenced in spectrum H of the film deposited at the lowest P_{RF} and $\dot{V}_{\mathrm{HMDSO}}$.

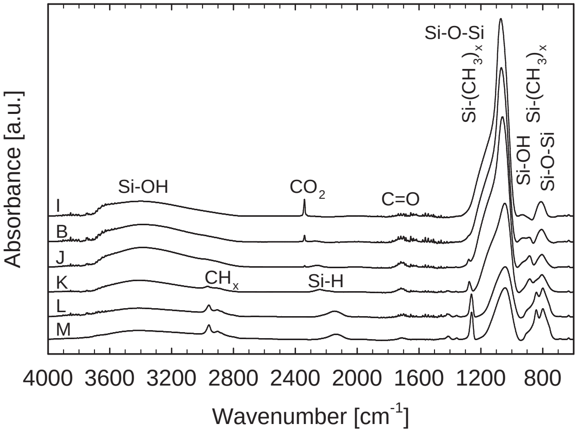

Figure 5.12: FTIR spectra of SiO_x coatings deposited at constant $P_{RF} = 100\,\mathrm{W}$ and $\dot{V}_{\mathrm{HMDSO}} = 2\,\mathrm{sccm}$ with an O_2/HMDSO flow rate ratio q of (I) 60, (B) 30, (J) 15, (K) 5, (L) 0 (pp-HMDSO), and (M) 0 (pp-HMDSO, $\dot{V}_{\mathrm{HMDSO}} = 10\,\mathrm{sccm}$).

FTIR spectra of coatings deposited under variation of q between 0 and 60 at constant $P_{RF} = 100\,\mathrm{W}$ and $\dot{V}_{\mathrm{HMDSO}} = 2\,\mathrm{sccm}$ are depicted in Figure 5.12. Vibrations of carbon containing species, such as C-H in CH_2 and CH_3 at 2880, 2900, and 2960 cm^{-1} or in Si-$(CH_3)_x$ at 810, 840, 880 and 1270 cm^{-1}, are clearly reduced with increasing q and disappear for $q \geq 30$. Similar behavior is observed for the absorption at around 2250 cm^{-1}, characteristic for the Si-H stretching vibration. The position of the absorption maximum is shifted towards higher wavenumbers from 2145 to 2241, 2258, and 2274 cm^{-1} as q is increased from 0 to 5, 15, and 30. It is known that the Si-H stretching frequency shifts towards higher frequencies with increasing sum of electronegativity of the atoms or functional groups bonded to the silicon [140, 141]. The stretching frequencies of the silicon monohydrates H-SiC_3, H-$SiOC_2$, H-SiO_2C, and H-SiO_3 were calculated to 2135, 2185, 2234 and 2283 cm^{-1} with an error of ±13 cm^{-1}, respectively [141]. Therefore, the observed frequency shift can be ascribed to a change in chemical environment of Si from mainly the two monohydrates H-SiC_3 and H-$SiOC_2$ in pp-HMDSO ($q = 0$) to H-SiO_3 in SiO_x at high values of q. A similar shift was observed for HMDSO derived SiO_x coatings in the literature [137] and the absorption around 2250 cm^{-1} was ascribed to Si-H in H-SiO_3 [142, 143]. For pp-HMDSO ($q = 0$), an increase of $\dot{V}_{\mathrm{HMDSO}}$ from 2 to 10 sccm does not induce significant changes in chemical structure as seen by comparing spectra L and M. Since the latter condition (pp-HMDSO deposited from $\dot{V}_{\mathrm{HMDSO}} = 10$ sccm) is used later on within multilayer coatings due to its high deposition rate, properties of this coating are also reported here and in the following. The peak position of the Si-O-Si stretching vibration is shifted to higher wavenumbers from 1041 to 1068 cm^{-1} and its intensity rises as q is increased from 0 to 60, indicating a densification of the Si-O network. The characteristic lower band for CO_2 at 2340 cm^{-1} is evident in the spectra for $q \geq 15$, indicating that for these conditions CO_2 is formed and confined to small voids in the network [139].

Consequently, changes in q and in CP show very similar effects on the chemical structure. Both increasing CP and q results in more SiO_2-like films, as seen by comparison of Figure 5.9 and 5.10 with Figure 5.12. An interdependence of q and P_{RF} is observed by various experimental methods in the literature [132, 138, 144]. Both increasing P_{RF} and q leads to a higher fragmentation and oxidation of monomer molecules as evidenced by mass spectrometry and optical emission spectroscopy [144]. Similar trends for both increasing P_{RF} and q are also found for other coating properties such as indentation hardness, wetting, and surface roughness [6]. These findings are consistent with results regarding the barrier performance and may explain the influence of CP and q on the diffusion barrier performance as presented in Figure 5.1 and 5.5. For good diffusion barrier performance at low P_{RF}, essential for a low thermal load on the PP substrate, a high O_2/HMDSO flow rate ratio needs to be applied in order to obtain sufficiently low organic content in the coating.

X-ray photoelectron spectroscopy

Further insight into the chemical composition of SiO_x coatings is gained by XPS analysis. The influence of q on the C/Si and O/Si atomic ratio of the resulting pp-HMDSO and SiO_x films is shown in Figure 5.13. The atomic ratios of thermal oxide grown on a Si wafer are given as a refer-

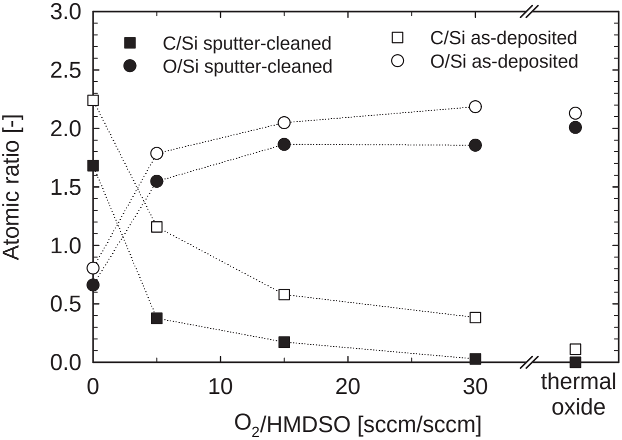

Figure 5.13: C/Si and O/Si atomic ratios from XPS analysis of as-deposited (open symbols) and sputter-cleaned samples (solid symbols) as a function of the O_2/HMDSO flow rate ratio q.

ence. In general, the as-deposited samples show higher C/Si and O/Si ratios than the sputter-cleaned films. The O/Si and C/Si ratio of the thermal oxide is reduced by sputter-cleaning from 2.13 and 0.11 to 2.01 and 0.00, respectively. The stoichiometric composition of SiO_2 after sputter-cleaning indicates that the sputter-cleaning procedure is adequate to remove organic surface contaminations and that no selective sputtering takes place. For the PECVD deposited films, the reduction of the C/Si and the O/Si atomic ratio by sputtering is more pronounced compared to the thermal oxide. This may be explained by post-deposition reactions of free radicals with hydrocarbons and residual water in the vacuum chamber of the PECVD process or the adsorption of oxygen and organic material from ambient. A C/Si ratio of 2.2 and an O/Si ratio of 0.8 is determined for as-deposited pp-HMDSO. Similar ratios are reported in the literature [145]. The precursor HMDSO exhibits theoretically a C/Si ratio of 3 and an O/Si ratio of 0.5. The lower C/Si ratio compared to the monomer is related to the formation of a crosslinked hydrocarbon network by methyl group abstraction and the higher O/Si ratio to reactions of long-lived radicals in the plasma polymer with atmospheric or residual oxygen and water in the plasma chamber [39, 145, 146]. The addition of oxygen results in a significant decrease of the C/Si ratio and in an increase of the O/Si ratio. Virtually carbon-free films are obtained for $q = 30$ with an O/Si ratio of 1.9. The observed trend is consistent with results from FTIR spectroscopy, indicating an increase of the Si-O absorption in Si-O-Si at the expense of carbon containing species (CH_x, Si-$(CH_3)_x$). A very similar trend is also observed in the OTR and deposition rate data (compare Figure 5.5 and 5.6) supporting the hypothesis that a high carbon content is detrimental for good diffusion barrier performance.

Figure 5.14 shows the detailed Si2p, C1s, and O1s spectra of as-deposited SiO_x films. Curve-fitting of the Si2p peaks is performed by four components according to four different configurations of silicon. A similar approach is frequently followed in the literature based on polydimethylsiloxane (PDMS) and quartz as reference materials [8, 147–149]. In PDMS, the silicon is bound to two carbon atoms and two oxygen atoms (SiO_2C_2 (D) configuration), while in quartz silicon is bound to four oxygen atoms (SiO_4 (Q) configuration). Binding energies in the range of $101.8 - 102.1\,\text{eV}$ are reported for PDMS and of $103.4 - 103.7\,\text{eV}$ for quartz. For the SiO_3C (T) configuration, the binding energy is estimated assuming the influence of adding one oxygen to be equal to half of the difference between these two Si2p peak positions [147]. For the case that silicon is bound to one oxygen and three carbon atoms, as in the precursor molecule HMDSO ($SiOC_3$ (M) configuration), peak positions of $100.7 - 101.5\,\text{eV}$ are reported. Accordingly, in Figure 5.14 the Si2p peaks are curve-fitted by four components at a binding energy of 100.7, 102.1, 102.9, and 103.7 eV assigned to the $SiOC_3$ (M), SiO_2C_2 (D), SiO_3C (T), and SiO_4 (Q) configuration, respectively. For all coatings good agreement of the envelope (dotted line) with the experimental data (solid line) is achieved. The concentrations of the four configurations are determined from the integrated areas of the fitted curves as an average of two lateral positions on the coatings. In Figure 5.15, the concentrations of the components are shown as proportion of the Si2p peak area in dependence of q. The PDMS-like SiO_2C_2 and the SiO_3C configuration are prevailing in pp-HMDSO, while for $q \geq 15$ silicon is predominantly found in the highly oxidized SiO_4 configuration. This supports the findings obtained

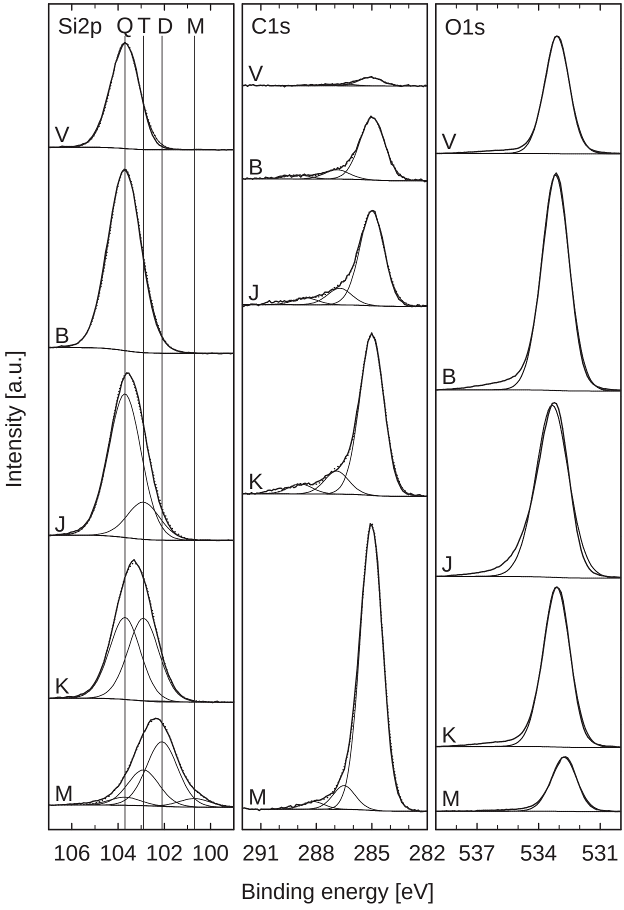

Figure 5.14: XPS Si2p, O1s, and C1s detail spectra of (V) SiO_2 (thermal oxide) and as-deposited SiO_x films with q = (B) 30, (J) 15, (K) 5, (M) 0 (pp-HMDSO, $\dot{V}_{\mathrm{HMDSO}} = 10\,\mathrm{sccm}$). Curve-fitting of the Si2p spectra by four components corresponding to SiO_4 at 103.7 eV (Q), SiO_3C at 102.9 eV (T), SiO_2C_2 at 102.1 eV (D), and $SiOC_3$ at 100.7 eV (M).

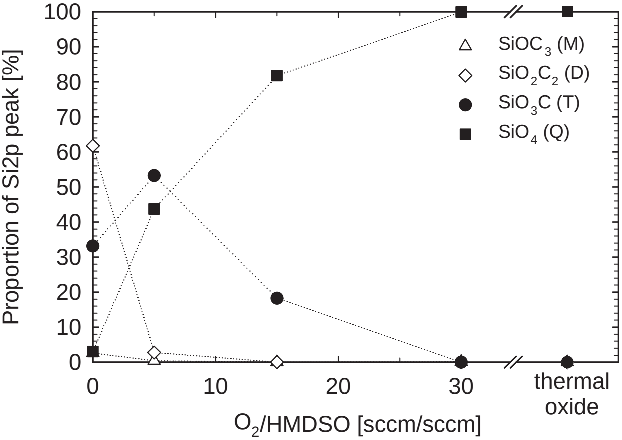

Figure 5.15: Composition of the Si functionalities determined by curve-fitting of the Si2p peak as a function of the O_2/HMDSO flow rate ratio.

by FTIR spectroscopy, where decreasing absorptions of carbon containing species, an increasing absorption of Si-O, and a shift of the Si-H peak position is observed with increasing q due to an increased oxidation state of silicon. The FWHM of the Si2p spectrum is 2.1 eV for the pp-HMDSO coating, decreases to $1.9 - 1.7$ eV with increasing oxygen content in the process gas mixture and drops to 1.5 eV for the thermally oxidized Si wafer reference sample. The FWHM of the fitted curves is constrained to be equal for the four components within a sample and varied only slightly in the range of $1.5 - 1.7$ eV among the different samples. The C1s signal, also shown in Figure 5.14, exhibits peaks of three contributions: aliphatic carbon and silicon bound to carbon at 285.0 eV, a peak at 286.7 ± 0.2 eV due to carbon bound to oxygen or nitrogen, and a peak at 288.5 ± 0.4 eV due to carbon bound to carboxylic groups, esters, or carbonates [126, 150]. The binding energy of oxygen is 532.8 ± 0.1 eV for the pp-HMDSO coating and 533.2 ± 0.1 eV for the SiO_x coatings. These are typical values for oxygen bound to organic carbon and oxygen bound to silicon [151, 152].

5.1.3 Mechanical analysis

Apart from the chemical structure, the mechanical properties of thin films deposited on PP are of great importance, since the reliability of a brittle diffusion barrier coating is controlled by its cohesion and its adhesion to the polymer both being influenced by the process-induced internal stress of the coating/polymer composite [12]. During life cycle, a high resistance of the coating to thermal and mechanical loads is essential, especially if the coating/polymer composite is exposed to elevated temperatures as they occur during autoclaving. Therefore, in the following, the mechanical properties of the coating/PP composites are explored, which are often closely related to the chemical properties of the coatings. The O_2/HMDSO flow rate ratio q is an important parameter to tailor not only the chemical but also the mechanical properties.

Tensile tests

For the analysis of the mechanical properties of coating/substrate composites, it is necessary to acquire properties of the applied substrate first. Young's modulus E_s of the 30 μm PP foil is determined by means of tensile tests to 611 ± 43 MPa from the linear part of the stress-strain curves shown in Figure 5.16. The tensile yield stress σ_Y is 18.1 ± 0.6 MPa. These values are calculated as an average of five samples cut parallel and perpendicular to the machine direction of the PP foil, respectively. Parallel to machine direction a slightly lower E_s and a higher σ_Y is found compared to the perpendicular direction. The average of both directions is considered to determine E_s and σ_Y, since these quantities are used to derive the coating toughness together with the data from fragmentation tests, which are performed in both directions without significant difference in results.

Dilatometry analysis

The dilatation behavior of PP and SiO_x/PP films during heating is investigated by means of dynamic mechanical analysis (DMA). The relative elongation of the films is shown in Figure 5.17 in the temperature range of 25 – 135°C. The CLTE of the uncoated PP film α_s was found to be equal to $2.0 \cdot 10^{-4}\,K^{-1}$ in good agreement with literature data [153, 154].

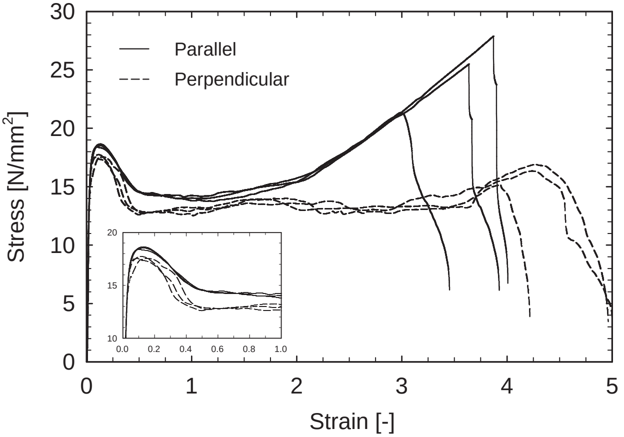

Figure 5.16: Stress-strain curves derived by tensile tests of uncoated 30 μm PP foil parallel and perpendicular to machine direction.

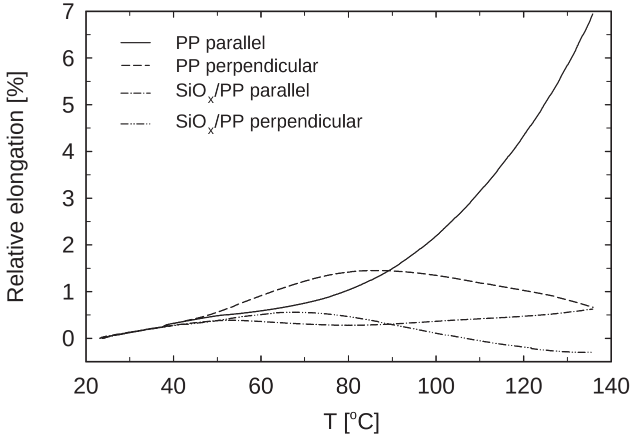

Figure 5.17: Dilatometry analysis of uncoated and SiO$_x$ coated 30 μm PP foil parallel and perpendicular to machine direction.

For the $\mathrm{SiO_x}$/PP composite, the CLTE is determined to $1.35 \cdot 10^{-4}\,\mathrm{K}^{-1}$. With increasing temperature, the influence of the coating on the dilation behavior becomes more important. The $\mathrm{SiO_x}$ coating prevents expansion of the PP film to a great extent, which is evidence for good adhesion and cohesion of the coating. A similar deviation is also observed for PET and $\mathrm{SiO_x}$/PET films above the glass transition temperature of PET, where the shrinkage is reduced by the coating [108]. The dilation behavior of the PP foil is remarkably anisotropic depending on the orientation with respect to its machine direction. Parallel to the machine direction a high elongation of several percent is observed, while at high temperatures even a slight shrinkage is noticed perpendicular to the machine direction. Therefore, at elevated temperatures a high tensile load is applied on the coatings in machine direction.

Internal stress

The internal in-plane stress is calculated from the radius of curvature of $\mathrm{SiO_x}$/PP composites according to Equation 2.26. The dependence of the internal stress on q is shown in Figure 5.18. E_s is determined by tensile tests to 611 MPa, and a Poisson's ratio of $\nu_s = 0.45$ is assumed. As a first approximation, E_c is estimated from $E_{\mathrm{SiO_2}}$ and $\alpha_{\mathrm{SiO_2}}$ values for PECVD $\mathrm{SiO_2}$ (80 GPa [111] and $1 \cdot 10^{-6}\,\mathrm{K}^{-1}$ [155]) and from the CLTE of the coatings α_c applying Equation 4.11. The CLTE of the coatings are deduced from the values for $\mathrm{SiO_2}$ and pp-HMDSO ($1.8 \cdot 10^{-5}\,\mathrm{K}^{-1}$ [107]) by linear interpolation using the C/Si atomic ratio, derived from XPS analysis, as the variable. Independent determination of E_c and α_c, applying for instance indentation techniques or thermal stress analyses, would clearly be useful [156]. Accordingly, Poisson's ratio ν_c is interpolated assuming that it is equal to 0.16 for $\mathrm{SiO_2}$ and 0.3 for pp-HMDSO [107, 157, 158]. Resulting values of E_c, ν_c, and α_c are summarized in Table 5.2. The internal in-plane stress is of compressive nature in all coatings (indicated by a negative algebraic sign). Internal stresses of the same range were determined for $\mathrm{SiO_x}$ deposited by PVD methods on PET [101, 108].

The thermal stress is calculated according to Equation 2.24 to estimate which component of the internal stress, as expressed by Equation 2.23, is prevailing in PECVD coatings on PP. Assuming a constant CLTE

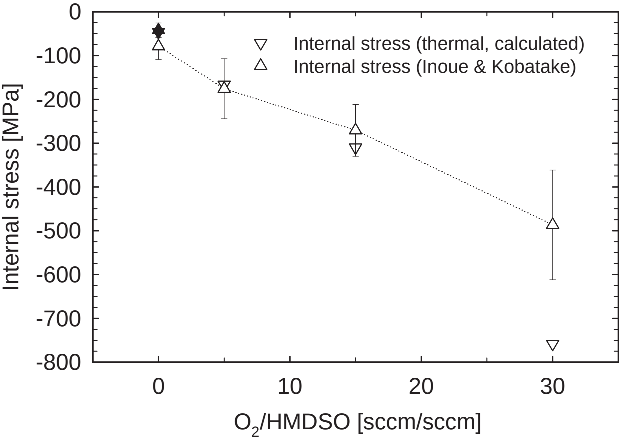

Figure 5.18: Internal in-plane stress as a function of q, $\dot{V}_{HMDSO} = 2\,\mathrm{sccm}$ (open symbols), $\dot{V}_{HMDSO} = 10\,\mathrm{sccm}$ (solid symbols).

for the substrate and the coating in the relevant temperature range, Equation 2.24 is integrated to obtain:

$$\sigma_{i,th} = \frac{E_c}{(1-\nu_c)}(\alpha_s - \alpha_c) \cdot (T_2 - T_1). \tag{5.1}$$

For a service temperature T_2 of 20°C, a process temperature T_1 of approximately 60°C, as measured during deposition at these conditions, E_c as derived by Equation 4.11, $\alpha_s = 2.0 \cdot 10^{-4}\,\mathrm{K}^{-1}$ from dilatometry analysis, and α_c from linear interpolation, $\sigma_{i,th}$ values of comparable magnitude to the measured internal stress values are calculated as indicated in Figure 5.18. In spite of the rather crude approximations, the obtained values are reasonable. This implies that for the investigated coating/substrate combination the thermal stress is the dominating component of the total internal stress.

Mass Density

The dependence of the mass density on q is illustrated in Figure 5.19. The density increases from 1.3 to 2.1 g/cm^3 as q is increased from 0 to 30. This

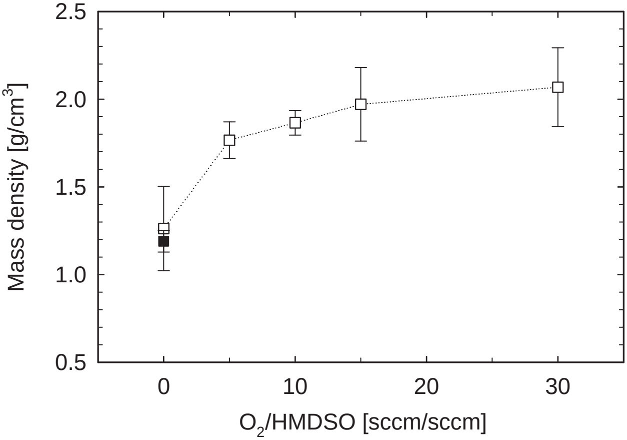

Figure 5.19: Influence of the O_2/HMDSO flow rate ratio q on the mass density at constant $P_{RF} = 100\,\mathrm{W}$, $\dot{V}_{HMDSO} = 2\,\mathrm{sccm}$ (open symbols), and $\dot{V}_{HMDSO} = 10\,\mathrm{sccm}$ (solid symbols).

effect is ascribed to the higher fragmentation of the HMDSO molecules with increasing q due to the higher abundance of atomic oxygen and the enhanced ion bombardment by mainly O_2^+ ions. Densities of SiO_x coatings produced by PECVD typically range between 1 and $2\,\mathrm{g/cm^3}$ depending on the deposition conditions [20]. The density of SiO_x obtained at $q = 30$ is close to the density of fused silica of $2.2\,\mathrm{g/cm^3}$ and compares well with densities obtained at similar process conditions [8, 159]. The dependence of the mass density on q follows a similar trend as the barrier performance at $P_{RF} = 100\,\mathrm{W}$ shown in Figure 5.5 and the C/Si atomic ratio (Figure 5.13). This suggests that a densification of the coating by removal of carbonated species is fundamental for the deposition of high performance gas diffusion barrier coatings. The mass density rises with the internal compressive stress as q is increased. A strong correlation of the internal stress with the coating density was also observed in the literature for evaporated SiO_2 films [101, 102].

Table 5.2: Deposition parameters and properties of SiO_x (B, J, K) and pp-HMDSO (L, M) coatings.

Layer	B	J	K	L	M
O_2/HMDSO ratio q [-]	30	15	5	0	0
$\dot{V}_{\mathrm{HMDSO}}$ [sccm]	2	2	2	2	10
P_{RF} [W]	100	100	100	100	100
R [nm/min]	177	198	307	543	710
OTR[a] [$cm^3/m^2/d$]	5	6	1142	> 2000	> 2000
Atomic composition					
$Si{:}O_x{:}C_y$ (x:y)	1.9:0.03	1.9:0.2	1.6:0.4	-	0.7:1.7
Mass density [g/cm^3]	2.1	2.0	1.8	1.3	1.2
Internal stress[b] [MPa]	-487	-271	-176	-79	-42
CLTE α_c [$10^{-6}\,K^{-1}$]	1.0	2.4	4.6	-	18.0
E_c [GPa]	80.0	32.8	17.4	-	4.4
ν_c [-]	0.16	0.17	0.18	-	0.30
α_{Du} [-]	0.98	0.96	0.92	-	0.73
Normalized ERR g [-]	15.4	9.6	6.3	-	2.7
COS[c] [%]	0.9	1.2	6.2	11.4	18.4
Toughness G_c [J/m^2]	20	9	77	-	77
CD_{sat} [mm^{-1}]	242	312	406	-	1334
IFSS τ [MPa]	28	21	65	-	162

[a] For constant $t_{dep} = 15 \times 4\,\mathrm{s}$ (h_c according to R).

[b] $h_c = 200\,\mathrm{nm}$.

[c] $h_c = 120\,\mathrm{nm}$.

Adhesive and cohesive properties

Adhesive and cohesive properties of SiO_x coatings are deduced from fragmentation tests. In Figure 5.20, optical micrographs of the crack pattern development are compared for SiO_x (layer B) and pp-HMDSO (layer L)

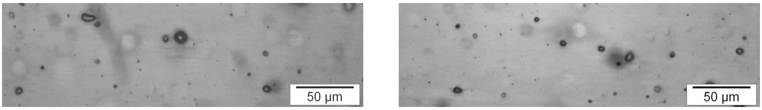

(a) 0.0%, SiO_x (b) 0.0%, pp-HMDSO

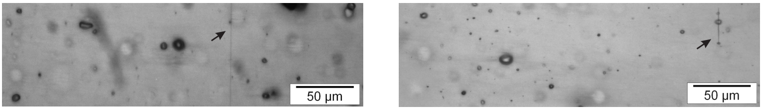

(c) 1.3%, SiO_x (COS) (d) 11.3%, pp-HMDSO (COS)

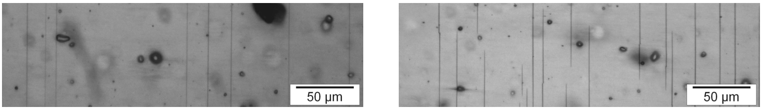

(e) 1.8%, SiO_x (f) 13.4%, pp-HMDSO

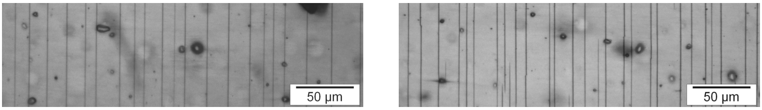

(g) 2.9%, SiO_x (h) 15.2%, pp-HMDSO

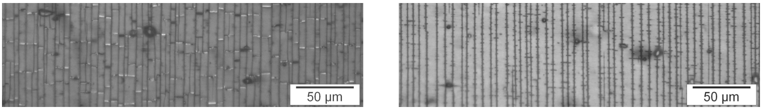

(i) 16.3%, SiO_x (j) 22.4%, pp-HMDSO

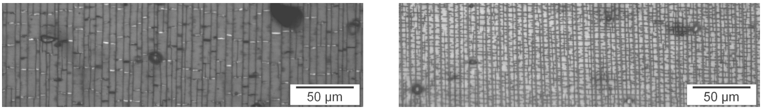

(k) 23.5%, SiO_x (l) 34.4%, pp-HMDSO

Figure 5.20: Optical micrographs of fragmentation of SiO_x ($q = 30$) and pp-HMDSO ($q = 0$) coatings on PP at various stages of applied strain ($\dot{V}_{HMDSO} = 2\,\text{sccm}$, $P_{RF} = 100\,\text{W}$).

at roughly the same positions on the sample, respectively. The tension is applied in horizontal direction. First fine cracks become visible in the SiO_x coating at 1.3% strain perpendicular to the loading direction. The first cracks in the pp-HMDSO coating appear at a much higher strain of 11.3%. As can be seen in Figures 5.20(c) and (d), the first cracks are induced by defects. Once the COS is exceeded, random cracking is observed for both coatings. At this stage, the interaction between the cracks is negligible and the crack location is determined by defects. The fragmentation rate is determined solely by the coating strength and the CD increases linearly with increasing strain. At a higher strain level, midpoint cracking occurs as the fragment width approaches the critical stress transfer length, and the fragmentation rate is markedly reduced. Similar fragmentation patterns are observed at this stage for both coatings but at different strain levels as shown in Figures 5.20(g) and (h). With further increased strain, transverse buckling failure occurs as a result of the Poisson effect, which causes lateral contraction of the PP substrate. This is observed for SiO_x in Figure 5.20(i), while for pp-HMDSO transverse buckling failure occurs at a much higher strain. Moreover, fragments are only partially cracked over the fragment width, indicating a less brittle character of this coating. Subsequently, the fragmentation process virtually stops as the IFSS is not sufficiently high to induce further cracks and delamination occurs. The crack density in the saturation regime (CD_{sat}) of pp-HMDSO clearly exceeds the CD_{sat} of SiO_x (compare Figure 5.20(k) and (l)).

Results of fragmentation tests are reported in Figure 5.21 as measured crack density with applied tensile strain for SiO_x coatings with varying q between 0 and 30. For SiO_x coatings with best barrier properties, i.e. for $q = 30$, an averaged COS of 0.9% is measured on PP, which is in reasonable agreement with values reported for SiO_x on PET [108, 160, 161]. Decreasing q results in a tremendous increase in the COS up to 18% for pp-HMDSO. The high COS is evidence for the polymeric character of pp-HMDSO with good cohesive properties. Accordingly, the CD_{sat} is increased with decreasing q. On the inset of Figure 5.21, the CD is shown as a function of the local strain at a highly strained position for a pp-HMDSO coating (layer M). An extremely high CD_{sat} of $1300\,\mathrm{mm}^{-1}$ is observed, being evidence for excellent adhesion of pp-HMDSO to the PP substrate. Properties of the investigated coatings are summarized in Ta-

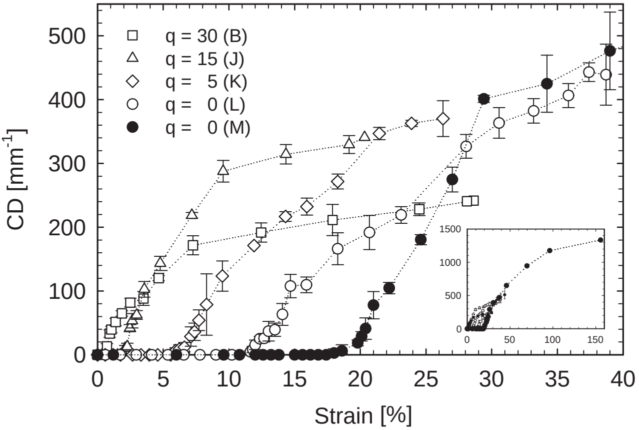

Figure 5.21: Crack density as a function of the applied strain of SiO_x coatings with varying O_2/HMDSO flow rate ratio q between 0 and 30. $P_{RF} = 100\,\mathrm{W}$, $\dot{V}_{HMDSO} = 2\,\mathrm{sccm}$ (open symbols), $\dot{V}_{HMDSO} = 10\,\mathrm{sccm}$ (solid symbols). Inset: pp-HMDSO (M) at a highly strained position.

ble 5.2. In order to calculate the coating toughness G_c according to Equation 2.33, the plain strain moduli of the coating and of the substrate $\bar{E}_c$ and $\bar{E}_s$, Dundurs' parameter α_{Du}, and the normalized ERR g are derived by Equations 2.34 to 2.36. The results are also reported in Table 5.2. The coating toughness G_c of SiO_x ($q = 30$) amounts to $20\,\mathrm{J/m^2}$. Andersons et al. [119] calculated a coating toughness of $14\,\mathrm{J/m^2}$ for SiO_x/PET of same coating thickness applying a finite fracture mechanics approach and similar values are derived experimentally for SiO_x/PI coatings from the steady-state ERR at COS. For pp-HMDSO, G_c is increased to $77\,\mathrm{J/m^2}$. The IFSS, a measure for the adhesion, also increases with increasing carbon content of the coating. The IFSS of the SiO_x/PP ($q = 30$) is found to be equal to 28 MPa, which is almost three times higher than the shear stress at yield τ_Y of the PP substrate equal to 10.5 MPa. This value was derived from the measured tensile yield stress of the polymer ($\sigma_Y = 18\,\mathrm{MPa}$) using the von Mises yield criterion $\tau_Y = \sigma_Y/\sqrt{3}$. The IFSS measured for the pp-HMDSO coating is as high as 162 MPa, even exceeding the tensile strength of the PP substrate, close to 125 MPa. This IFSS value is likely to be overestimated, essentially due to the calculation of σ_{max} which assumes that the pp-HMDSO coating is fully elastic up to strains as high as its COS equal to 18%. A very high IFSS implies that the pp-HMDSO/PP interface is capable of strain hardening. This is in fact visible in the inset of Figure 5.21, where tensile failure of the pp-HMDSO coating still operates at strain levels beyond 150%.

5.1.4 Defect analysis

The dependence of the OTR on the $\mathrm{SiO_x}$ coating thickness h_c is explored on PP substrate for a set of favorable process parameters ($\mathrm{P}_{RF} = 100\,\mathrm{W}$, $\dot{V}_{\mathrm{HMDSO}} = 2\,\mathrm{sccm}$, and $q = 30$). Results are compared in Figure 5.22 to results obtained on PET at the very same conditions. The dependence of the diffusion barrier performance on h_c follows very similar trends regardless of whether PP or PET is used as substrate. For both substrates the OTR drops by more than one order of magnitude if a critical coating thickness $h_{c,crit}$ of approximately 12 nm is exceeded. This value compares well with the critical coating thickness of $12-40\,\mathrm{nm}$ reported in the literature for $\mathrm{SiO_x}$ on PET [1, 93]. Further increase of the coating thickness improves the barrier performance only slightly. For a coating thickness of 180 nm, lowest OTR values of 0.3 ± 0.1 and $5.1 \pm 3.5\,\mathrm{cm^3/m^2/d}$ are obtained on PET and PP substrate, respectively. No further barrier improvement is achieved for $h_c > 180\,\mathrm{nm}$. On PET comparable residual OTR values were obtained in the literature and ascribed to defects in the $\mathrm{SiO_x}$ coating [1, 8, 93].

In order to estimate whether the higher residual OTR of $\mathrm{SiO_x}$ on PP substrate compared to PET may be fully attributed to defects, approximate calculations are performed based on the approach of Rossi and Nulman [86] applying Equation 2.22. The defect density n_d is for this purpose determined experimentally from multiple micrographs of chemically etched PET and PP substrate through defects in $\mathrm{SiO_x}$ coatings. Optical micrographs of defect patterns are exemplarily compared in Figure 5.23 and 5.24 for PP and PET at various coating thicknesses. The defect density is drastically reduced from approximately 4000 to $40\,\mathrm{mm^{-2}}$ as the coating thickness is increased from 6 to 180 nm. Comparable defect densities are obtained for PP and PET substrate at same

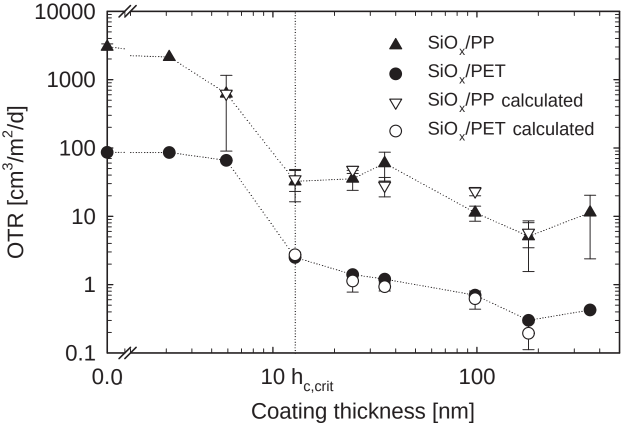

Figure 5.22: OTR as a function of the coating thickness h_c for SiO_x on 30 μm PP foil and on 12 μm PET foil.

coating thicknesses (and same applied process conditions). Measured defect densities for high-quality research-grade and commercially available evaporated aluminum coatings on PET range from 25 to 400 mm^{-2} with the maximum of the defect size distribution at $1 - 2\,\mu$m [96]. Large cavities are etched in the polymer through defects in the coating, forming even free-standing films in some cases. In Figure 5.25(a), this can be observed on the scanning electron micrograph of chemically etched cavities in PP through defects in a SiO_x coating ($h_c \approx 100\,$nm). For that reason the chemical etching technique does not allow to deduce original defect sizes or defect size distributions from the defect patterns. Therefore, the defect size is fit to the experimental data by a least square approach for PP and PET substrate separately. An average defect size of 0.5 and 0.8 μm was obtained for PP and PET, respectively. These are realistic values and compare well with the average defect size of 0.6 μm determined by reactive ion etching (RIE) with atomic oxygen of SiO_x on PET foil [98]. The higher average defect size may be related to the higher roughness of the PET foil (S_a = 38 nm) compared to the PP

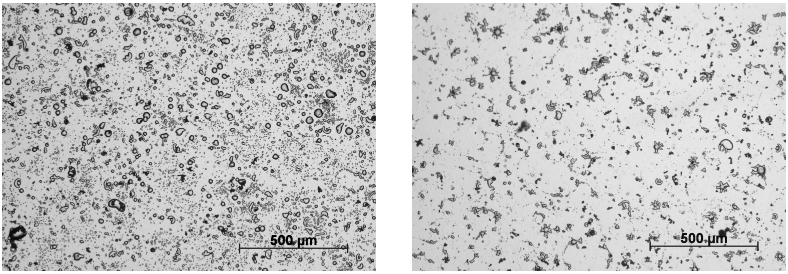

(a) $h_c = 6\,\mathrm{nm}$ (b) $h_c = 13\,\mathrm{nm}$

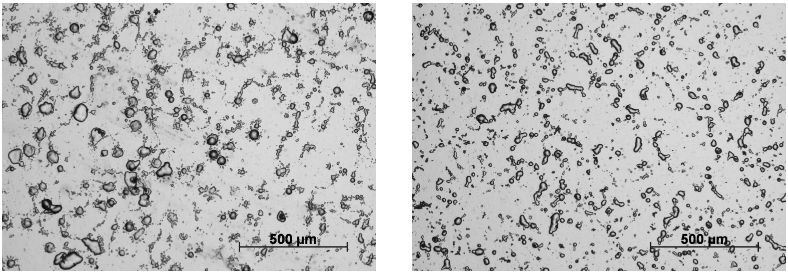

(c) $h_c = 25\,\mathrm{nm}$ (d) $h_c = 35\,\mathrm{nm}$

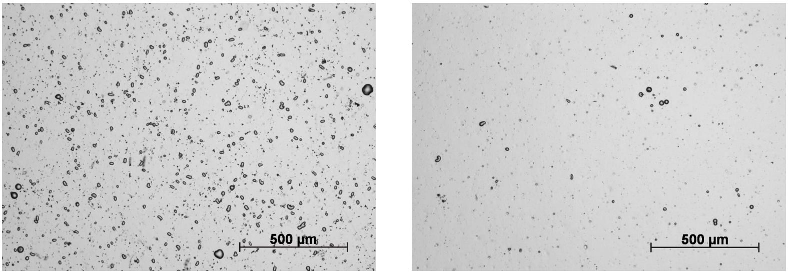

(e) $h_c = 100\,\mathrm{nm}$ (f) $h_c = 180\,\mathrm{nm}$

Figure 5.23: Optical micrographs of defect patterns in $\mathrm{SiO_x}$ coatings with varying coating thickness on PP after chemical etching with a mixture of 65 wt% H_2SO_4, 32 wt% H_3PO_4, and 3 wt% $KMnO_4$ for 48 h.

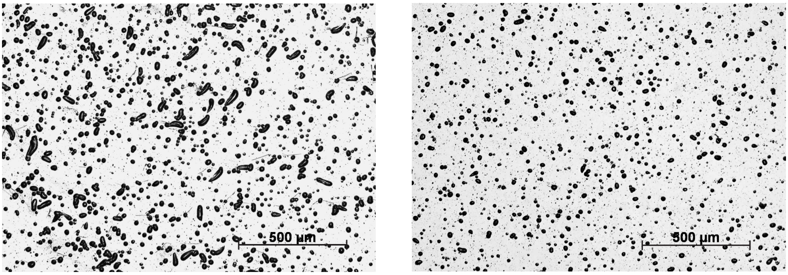

(a) $h_c = 6\,\mathrm{nm}$ (b) $h_c = 13\,\mathrm{nm}$

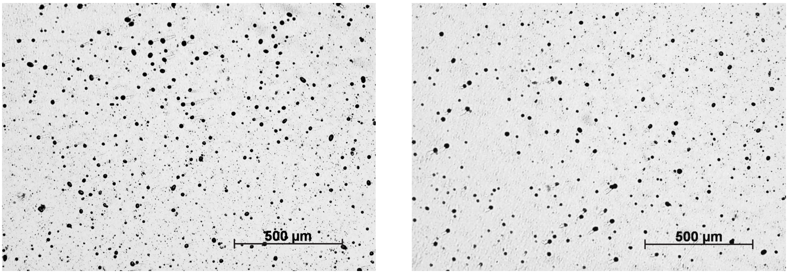

(c) $h_c = 25\,\mathrm{nm}$ (d) $h_c = 35\,\mathrm{nm}$

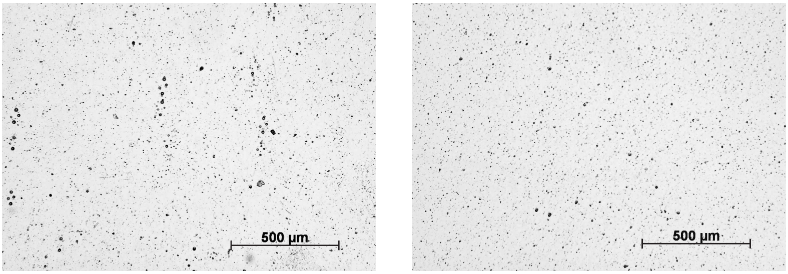

(e) $h_c = 100\,\mathrm{nm}$ (f) $h_c = 180\,\mathrm{nm}$

Figure 5.24: Optical micrographs of defect patterns in SiO_x coatings with varying coating thickness on PET after chemical etching with H_2SO_4 for 30 s.

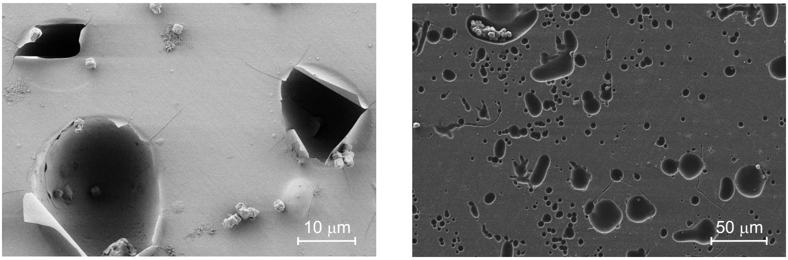

(a) $h_c \approx 98\,\text{nm}$, 5000× magnification (b) $h_c \approx 3\,\text{nm}$, 1000× magnification

Figure 5.25: Scanning electron micrographs of SiO_x coatings on PP after 48 h of chemical etching.

foil ($S_a < 2\,\text{nm}$). OTR values calculated from the defect density n_d by Equation 2.22 are compared with the measured values in Figure 5.22. Irrespective of the rather crude assumptions and simplifications, good agreement is achieved over a wide range of coating thickness. This suggests that for both PET and PP the residual permeation is due to defects in the SiO_x coating. The size of the defects is less decisive than the defect density, since good agreement of measured and calculated OTR values is obtained over a wide range of coating thickness assuming a constant average defect size. The higher residual oxygen permeation through SiO_x coated PP compared to PET is caused by the much higher substrate permeability of PP. Agreement is even found for coating thicknesses at and below the critical coating thickness with same average defect size. Figure 5.25(b) shows a scanning electron micrograph of a chemically etched SiO_x coating of approximately 3 nm thickness on PP. At a very early stage of film growth, even below the critical thickness, full coverage of the substrate is obtained on both polymer surfaces containing a very high number of defects. This shows that the deposition follows the Frank-van der Merwe (layer-by-layer) rather than the Volmer-Weber growth (island coalescence) mechanism. Consistent results are obtained in the literature for PECVD of even thinner SiO_x coatings of 2 nm on PET, PP, and PI substrate [162].

Further evidence for the residual permeation through defects is ob-

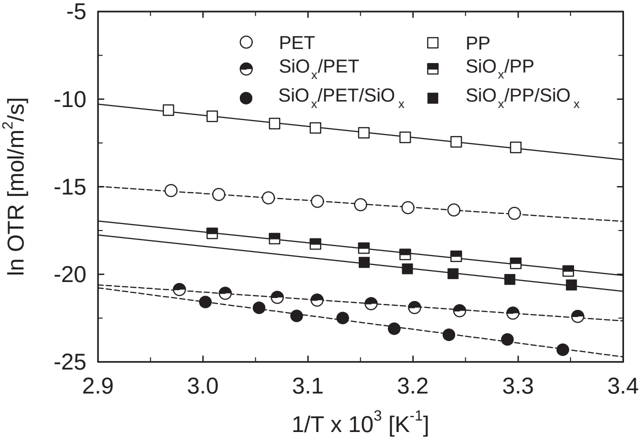

Figure 5.26: Arrhenius-type plot of the temperature dependent oxygen permeation through uncoated, single- and double-side coated PET and PP substrate in the temperature range of 25 – 60°C.

tained from activated rate theory [82, 95]. The temperature dependence of the permeation of noninteracting gases through polymers below their glass temperature follows Arrhenius behavior as described by Equation 2.18. The temperature dependence of oxygen permeation through uncoated, single- and double-side coated PP and PET substrate is shown in Figure 5.26. It is noteworthy that in the applied temperature range of 25 – 60°C the data for both PET and PP can be described by Equation 2.18, although temperatures are clearly exceeding the glass transition temperature for the latter. The apparent activation energies for permeation, compared in Table 5.3, are calculated from the slopes of the regression lines. Resulting ΔE_P values of uncoated PET and PP foil compare well with the reported values in the literature of 32.3 and 47.7 kJ/mol, respectively [163]. For both polymers, ΔE_P is not changed within the experimental error by the deposition of SiO$_x$ on one side. Similar ΔE_P values are reported for the permeation of oxygen through SiO$_x$ coated PET [82, 93, 95]. Diffusion through defect-free SiO$_x$ would implicate a much higher ΔE_P in the range of 92 – 290 kJ/mol as it is

Table 5.3: Apparent activation energy for permeation ΔE_p and OTR at 25°C through uncoated, single- and double-side SiO_x coated PET and PP foil.

Sample	ΔE_P [kJ/mol]	OTR [$cm^3/m^2/d$]
PET	33.4 ± 1.7	86.2
SiO_x/PET	33.7 ± 1.5	0.3
SiO_x/PET/SiO_x	64.7	< 0.05
PP	50.4 ± 1.7	3061.8
SiO_x/PP	53.5 ± 2.8	5.1
SiO_x/PP/SiO_x	53.4	2.2

reported for amorphous glasses [82]. This further supports the hypothesis that the SiO_x coating is defective, regardless of the substrate, with defect sizes large enough for unhindered transport of O_2 molecules. For SiO_x/PET/SiO_x, the OTR is reduced down to the measurement sensitivity limit of $0.05\,cm^3/m^2/d$ at room temperature and ΔE_P is increased significantly to 64.7 kJ/mol. This is consistent with the results of Tropsha and Harvey [82]. They report an even more pronounced increase of ΔE_P to 84.1 kJ/mol, which is almost in the ΔE_P range of amorphous glasses. Deposition of SiO_x on both sides of the PP substrate reduces the OTR to $2.2\,cm^3/m^2/d$, corresponding to an additional improvement of approximately a factor of two compared to the single-sided coating on PP. This agrees with the prediction from ideal laminate theory (Equation 2.17). Nevertheless, the ΔE_P value remains close to that of uncoated and single-side coated PP substrate. For SiO_x/PP/SiO_x the results are more consistent with those obtained by da Silva Sobrinho, who observed identical ΔE_P values for the oxygen permeation through double-side SiN and SiO_2 coated PET samples [93]. The different behavior regarding ΔE_P for double-side coated PET and PP may be related to the higher lateral diffusion in PP. On the basis of the empirical model presented by Tropsha and Harvey [82], schematic O_2 permeation pathways are proposed in Figure 5.27 for single- and double-side SiO_x coated PET and

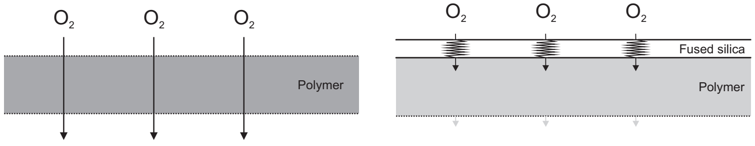

(a) uncoated, $\Delta E_{P,\mathrm{PET}} = 33.4\,\mathrm{kJ/mol}$, $\Delta E_{P,\mathrm{PP}} = 50.4\,\mathrm{kJ/mol}$

(b) hypothetical defect-free layer of fused silica, $\Delta E_P = 92 - 290\,\mathrm{kJ/mol}$

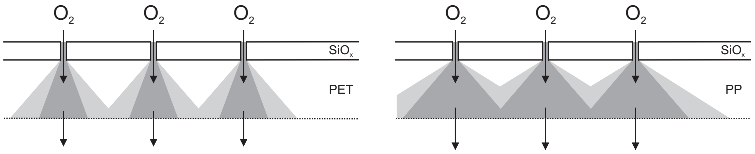

(c) SiO$_\mathrm{x}$/PET, $\Delta E_P = 33.7\,\mathrm{kJ/mol}$

(d) SiO$_\mathrm{x}$/PP, $\Delta E_P = 53.5\,\mathrm{kJ/mol}$

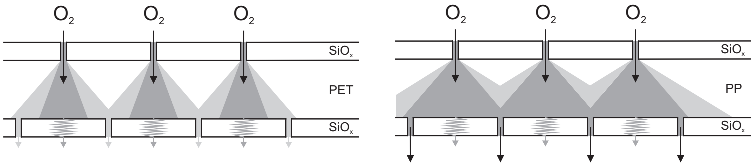

(e) SiO$_\mathrm{x}$/PET/SiO$_\mathrm{x}$, $\Delta E_P = 64.7\,\mathrm{kJ/mol}$ (defect decoupling)

(f) SiO$_\mathrm{x}$/PP/SiO$_\mathrm{x}$, $\Delta E_P = 53.4\,\mathrm{kJ/mol}$

Figure 5.27: Schematic O$_2$ permeation pathways through uncoated, single- and double-side SiO$_\mathrm{x}$ coated PET and PP foil.

PP foil, providing an explanation for the observed behavior regarding the apparent activation energy for permeation. While for PET decoupling of the defects results in an increase in ΔE_P, this effect is not observed for PP despite of similar defect densities on both polymers (i.e. a similar mean distance between the defects), since the extended lateral diffusion pathways of O$_2$ in PP still enable unhindered transport through defects on both sides of the polymer.

5.2 Amorphous carbon coatings

Amorphous carbon (a-C:H) coatings derived from a hydrocarbon source, such as CH_4 or C_2H_2, show interesting properties and are very versatile. By the addition of other gases, commonly used are Ar, He, N_2, NH_3, or CF_4, film properties like hardness, internal stress, density, wetting, optical, and structural properties can be modified [60, 130, 164]. In the following, a-C(:N):H films are investigated, since preliminary experiments showed that these films combine diffusion barrier performance with good mechanical properties. The addition of HMDSO to mixtures of C_2H_2 and N_2 may further improve mechanical film properties. Furthermore, the application of a-C:N:H and a-Si:C:O:N:H layers in a multilayer approach with a SiO_x layer may be promising to achieve diffusion barrier coatings with improved thermomechanical stability. This will be addressed in Section 5.3.

Diffusion barrier performance

Depending on the N_2/C_2H_2 flow rate ratio, a-C:N:H coatings show barrier properties with an optimal range between 3 and 7, as shown in Figure 5.28. A similar trend is observed for the OTR of a-C:H coatings from corresponding mixtures of Ar and C_2H_2, but inferior barrier performance is achieved for all flow rate ratios. This suggests that nitrogen is not only acting as a dilutant under these conditions.

Deposition rate

The dependence of the deposition rate on the N_2/C_2H_2 flow rate ratio is shown in Figure 5.29 for continuous (60 s) and discontinuous (15×4 s) deposition. Ellipsometry appears to underestimate the thickness compared to profilometry in most cases. Rates of discontinuous and continuous deposition follow the same trend. For N_2/C_2H_2 flow rate ratios between 3 and 11 an increase of deposition rate is observed with increasing N_2/C_2H_2 ratio for discontinuous deposition and a plateau for continuous deposition. Similar behavior is observed for Ar-CH_4 mixtures. It is ascribed to enhanced ionization accompanied by a higher degree of dissociation due to the addition of inert gas [42, 165, 166]. A clear decrease in deposition rate is observed at higher N_2/C_2H_2 ratios. Similar results

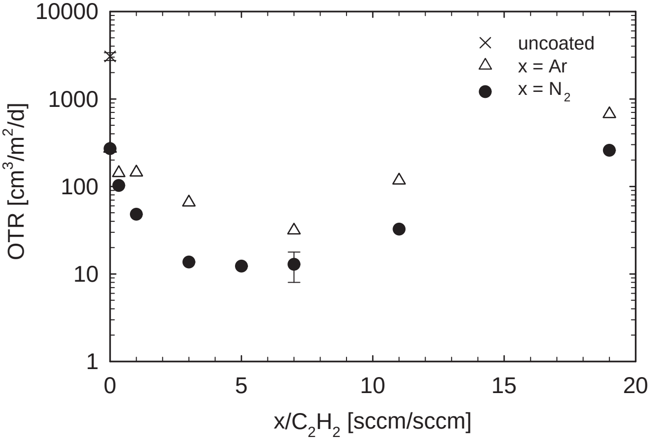

Figure 5.28: Dependence of the OTR on the N_2/C_2H_2 or Ar/C_2H_2 volumetric flow rate ratio of a-C(:N):H coatings deposited in discontinuous mode (15 × 4 s) at constant $p = 10\,\mathrm{Pa}$, $P_{RF} = 50\,\mathrm{W}$, and a total gas flow rate of $\dot{V} = 60\,\mathrm{sccm}$.

are obtained by other authors and are explained not only by the dilution of the precursor, but also by the etching effect of N_2^+ ions [71, 167]. For other hydrocarbon precursors (e.g. CH_4) or other nitrogen containing gases (e.g. NH_3), the ion induced effects are even more pronounced [28, 42, 168]. A competition of deposition and etching is claimed to be the reason for the existence of a maximum in nitrogen content, which is reported to be around 22 at.%, reached for a N_2/C_2H_2 flow rate ratio of 13 [167]. For other hydrocarbon precursors, the highest possible nitrogen incorporation is even lower. Irrespective of the N_2/C_2H_2 flow rate ratio, higher deposition rates are observed for discontinuous (15 × 4 s) compared to continuous (60 s) deposition. A plausible explanation is the possibility of recovery from C_2H_2 depletion during off-time. Depletion of the fast reacting precursor is more likely at high N_2/C_2H_2 ratios and might occur additionally to the etching effect of N_2^+ ions. Another possibility is post-plasma polymerization, which was observed by Inagaki and Yasuda for N_2-C_2H_2 mixtures applying a thickness monitor [169].

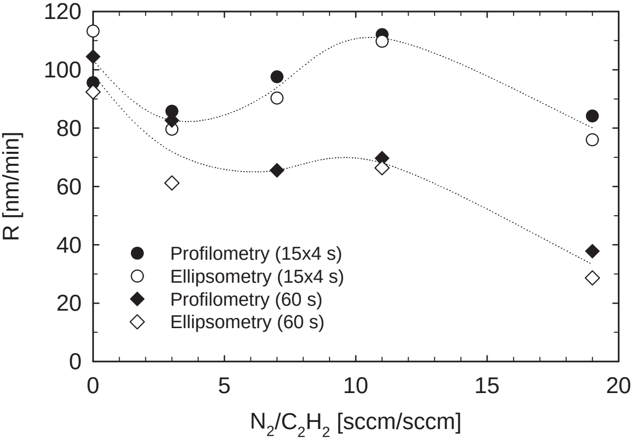

Figure 5.29: Dependence of deposition rate R on the N_2/C_2H_2 volumetric flow rate ratio for continuous (60 s) and discontinuous (15×4 s) deposition of a-C(:N):H at constant $p = 10\,\mathrm{Pa}$, $P_{RF} = 50\,\mathrm{W}$, and a total gas flow rate of $\dot{V} = 60\,\mathrm{sccm}$.

Plasma polymerization may initiate post-plasma polymerization due to high concentrations of trapped free radicals and the absence of etching N_2^+ ions during plasma off-time. From the experimental data, it is impossible to deduce which effect is prevailing.

Analysis of chemical structure

Further evidence for the incorporation of nitrogen into coatings from mixtures of N_2 and C_2H_2 is obtained by ATR FTIR spectroscopy. In Figure 5.30 spectra of a-C(:N):H coatings are shown, which were deposited with varying N_2/C_2H_2 ratio from 0 to 19. Strong absorption bands at $1374\,\mathrm{cm}^{-1}$ and $1450\,\mathrm{cm}^{-1}$ can be assigned to C-H bending of CH_3 and CH_2, respectively. These absorptions as well as symmetric and asymmetric CH_x stretching absorptions at 2834, 2864, $2913\,\mathrm{cm}^{-1}$ and $2948\,\mathrm{cm}^{-1}$ originate predominantly from the PP substrate. At $1600\,\mathrm{cm}^{-1}$ a growing absorption band with increasing N_2/C_2H_2 ratio can be ob-

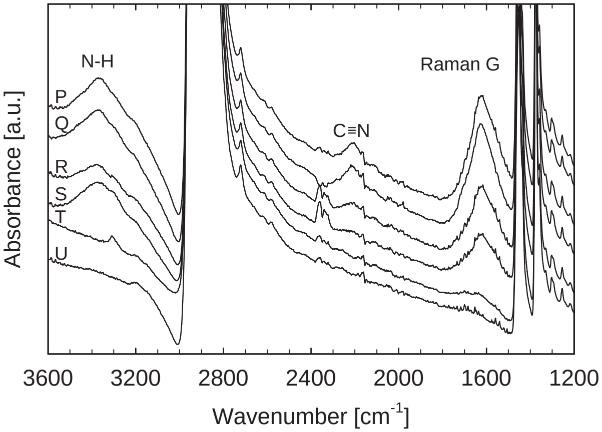

Figure 5.30: ATR FTIR spectra of a-C(:N):H coatings deposited at $p = 10\,\mathrm{Pa}$, $P_{RF} = 50\,\mathrm{W}$, and $\dot{V}_{tot} = 60\,\mathrm{sccm}$ as a function of the N_2/C_2H_2 volumetric flow ratio of (P) 19, (Q) 11, (R) 7 (S) 3, (T) 0 (a-C:H), and (U) uncoated PP substrate.

served. It is characteristic for the Raman G band, which becomes IR active due to the charge distribution symmetry breaking, introduced by the incorporation of nitrogen [170]. The addition of nitrogen can also result in the formation of C=N (imino) groups and the absorption near $1600\,\mathrm{cm}^{-1}$ may be a convolution of C=N stretching, N-H bending, and C=C stretching vibrations [171]. At $2200\,\mathrm{cm}^{-1}$ a smaller band related to the C≡N (nitrile) group also rises with increasing nitrogen content as well as a broader absorption with a maximum at $3365\,\mathrm{cm}^{-1}$ which is characteristic for the N-H stretching mode. The nitrile as well as the amino group are terminating groups, thus reducing the degree of overconstraining in the amorphous carbon network and, therefore, reducing the internal stress in the coating up to 50% [167, 172, 173]. The maximum in nitrogen incorporation of approximately 22 at.%, observed by Jacobsohn et al. [71, 172] for N_2/C_2H_2 flow rate ratios exceeding 13, is consistent with results from FTIR analysis shown in Figure 5.30. The prominent absorptions of nitrogen containing groups at 1600, 2200, and

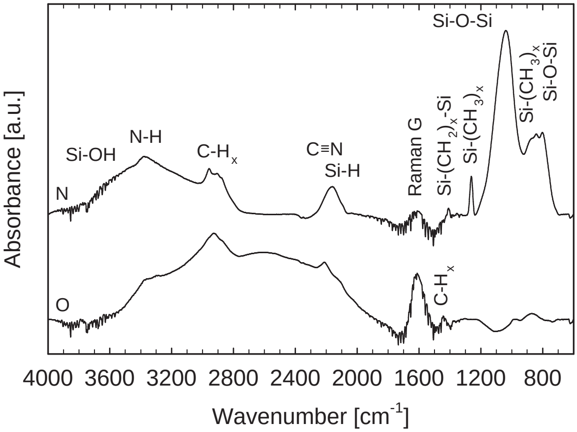

Figure 5.31: FTIR spectra of (N) a-Si:C:O:N:H and (O) a-C:N:H ($N_2/C_2H_2 = 7$) on Si wafers.

3365 cm^{-1} are not enlarged by increasing the N_2/C_2H_2 ratio from 11 to 19. An a-Si:C:O:N:H film was produced by adding HMDSO to N_2 and C_2H_2. Corresponding process parameters are given in Table 5.4. The FTIR spectrum of this material is shown in Figure 5.31 and compared to the spectrum of a-C:N:H. Both spectra are obtained in transmission mode of films deposited on a Si wafer. Additionally to the features observed in the spectrum of a-C:N:H (spectrum O), Si containing species are observed in a-Si:C:O:N:H (spectrum N), which resembles the spectrum of pp-HMDSO (spectra L and M) shown in Figure 5.12. The Si-O stretching peak position is shifted down to 1030 cm^{-1} and the absorption overlaps with the absorption at 930 cm^{-1}, which can be ascribed to both the bending vibration of Si-N and Si-OH. Absorptions of Si-$(CH_3)_x$ are observed at 810, 840, and 1260 cm^{-1} as well as in the spectrum of pp-HMDSO. A smaller absorption of C≡N at 2200 cm^{-1} is presumably superimposed by the more pronounced absorption of Si-H at 2150 cm^{-1}, both being terminal bonds. Therefore, films of a-Si:C:O:N:H show a high carbon content, a high fraction of terminating bonds, and a low degree of crosslinking with a similar structure to pp-HMDSO.

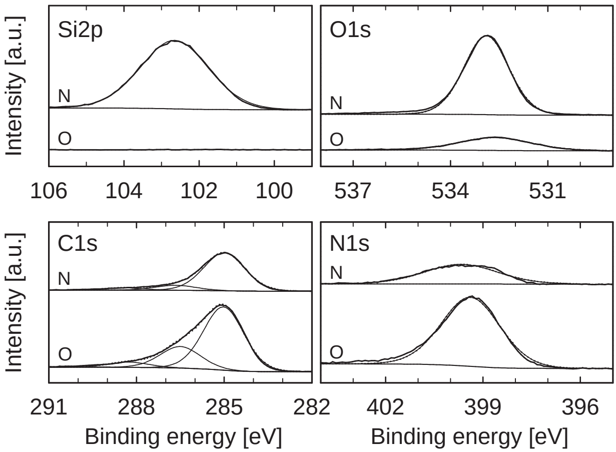

Figure 5.32: XPS Si2p, O1s, C1s, and N1s detail spectra of (N) a-Si:C:O:N:H and (O) a-C:N:H (N_2/C_2H_2 ratio = 7).

XPS Si2p, O1s, C1s, and N1s detail spectra of a-Si:C:O:N:H and a-C:N:H are shown in Figure 5.32. The derived atomic composition is reported in Table 5.4. The Si2p peak position and the FWHM of a-Si:C:O:N:H (spectrum N) is found at 102.7 eV and 2.1 eV, respectively. Very similar values are observed for pp-HMDSO (102.4 eV and 2.1 eV). Accordingly, the same O1s binding energy of 532.8 ± 0.1 eV is found for a-Si:C:O:N:H and pp-HMDSO. This supports the similarity in chemical structure to pp-HMDSO observed by FTIR spectroscopy. Additionally, nitrogen containing functionalities are present within this material. For the a-C:N:H and the a-Si:C:O:N:H layer, N1s was found at 399.4 eV and at 399.7 eV, respectively, a binding energy typical for organic nitrogen [126, 150].

The COS and the CD_{sat} of the a-C:N:H and the a-Si:C:O:N:H coating are summarized in Table 5.4 as well as their OTR. The high COS of a-C:N:H and a-Si:C:O:N:H compared to SiO_x indicates improved cohesion, while the CD_{sat}, related to the adhesive properties of the coatings, is not increased significantly. The higher COS of a-Si:C:O:N:H compared

Table 5.4: Deposition parameters and properties of (N) a-Si:C:O:N:H and (O) a-C:N:H coatings.

Layer	N	O
$\dot{V}_{\mathrm{HMDSO}}$ [sccm]	2	-
$\dot{V}_{\mathrm{N_2}}$ [sccm]	55	52.5
$\dot{V}_{\mathrm{C_2H_2}}$ [sccm]	3	7.5
P_{RF} [W]	75	50
R [nm/min]	207	94
OTR [cm^3/m^2/d]	100	14
Atomic composition	$\mathrm{SiO_{1.0}C_{1.5}N_{0.2}}$	$\mathrm{C_{1.0}N_{0.05}}$
COS [%]	3.8	2.7
CD_{sat} [mm^{-1}]	265	210

to a-C:N:H is accompanied by an inferior diffusion barrier performance. For these coatings, a similar trade-off between mechanical properties and barrier performance seems to exist as for $\mathrm{SiO_x}$ and pp-HMDSO coatings with varying $\mathrm{O_2}$/HMDSO flow rate ratio q.

5.3 Multilayer coatings

The combination of coating layers showing superior mechanical properties with a coating layer of good diffusion barrier performance in a multilayer approach may result in barrier coatings with improved temperature durability. The explored multilayer coatings are schematically illustrated in Figure 5.33.

5.3.1 Temperature durability

Results of dry heat and autoclaving tests of single- and multilayer coatings are summarized in Figure 5.34. Temperatures up to 100°C do not induce significant changes in barrier properties of all investigated coatings. However, after 30 min at 120°C the single SiO_x coating shows the beginning of deterioration in barrier performance with a relatively high standard deviation. This might indicate that the SiO_x coating is at the limitation of its thermomechanical durability. After extended exposure to 140°C, cracks are induced in the brittle SiO_x coating perpendicular to the machine direction as evidenced by OM in Figure 5.35(a). These cracks are caused by the tensile stress induced by the high dilatation of the PP foil in machine direction and result in a drastic increase in OTR as shown in Figure 5.34. For SiO_x coatings by PVD on PET, extended exposure to temperatures as low as 60°C is reported to induce cracks related to an adverse alteration of barrier properties [174].

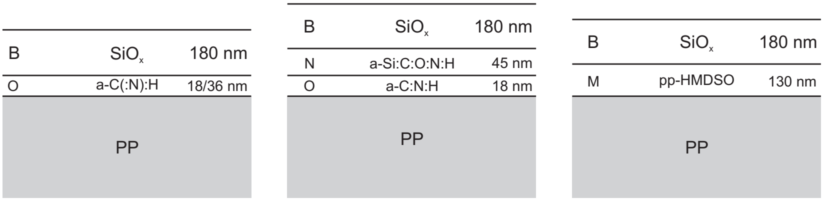

(a) SiO_x/a-C(:N):H

(b) SiO_x/ a-Si:C:O:N:H/a-C:N:H

(c) SiO_x/pp-HMDSO

Figure 5.33: Multilayer coatings on PP foil.

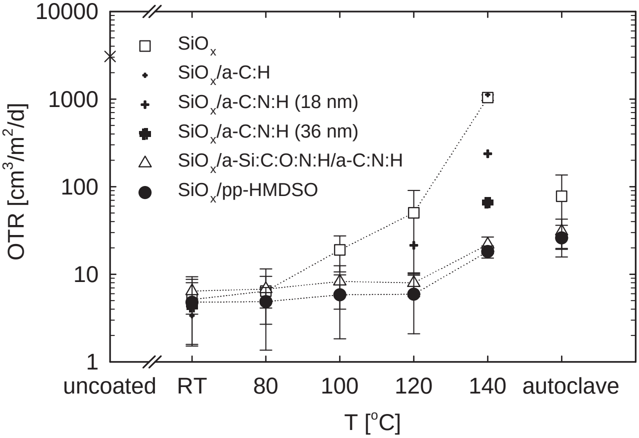

Figure 5.34: OTR of single- and multilayer coatings on PP foil after deposition, after 30 min at 80, 100, 120, 140°C, and after 30 min autoclaving at 121°C and 2.1 bar of steam. SiO_x (layer B), SiO_x/pp-HMDSO (layer B/M), SiO_x/a-C:N:H (layer B/O), and SiO_x/a-Si:C:O:N:H/a-C:N:H (layer B/N/O).

The SiO_x/a-Si:C:O:N:H/a-C:N:H coating shows an improved temperature durability. Even after exposure to 140°C for 30 min cracks are absent as shown in Figure 5.35(b), and the OTR increases only to 22 $cm^3/m^2/d$ compared to more than 1000 $cm^3/m^2/d$ for the single SiO_x coating. An a-C:H interlayer (Ar/C_2H_2 ratio = 7) does not improve temperature durability after exposure to 140°C. In contrast, at same conditions, improved temperature durability is observed for SiO_x/a-C:N:H coatings. However, the loss of barrier performance depends on the thickness of the a-C:N:H layer as seen in Figure 5.34 by comparing the OTR of the two SiO_x/a-C:N:H coatings with an a-C:N:H interlayer thickness of 18 and 36 nm. This suggests that a reduction of the thermal expansion mismatch by the interlayer, rather than the adhesion to the substrate, is responsible for the improved temperature durability of the multilayer coatings. Autoclaving in steam at 121°C and 2.1 bar for 30 min affects the SiO_x coating less than the exposure to 140°C, and a similar OTR is measured

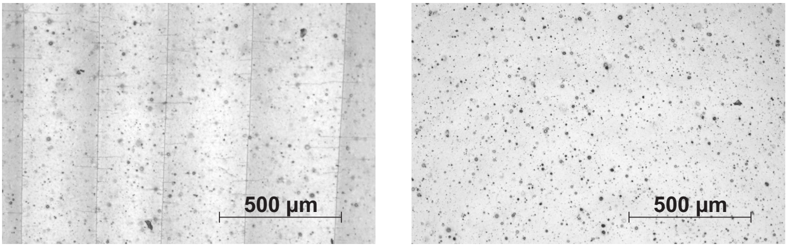

(a) Cracks in SiO_x coating

(b) SiO_x/a-Si:C:O:N:H/a-C:N:H coating

Figure 5.35: Optical micrographs of coatings after exposure to 140°C for 30 min.

as for the exposure to 120°C under dry conditions. Therefore, the temperature and the resulting thermal expansion mismatch seem to be crucial for barrier performance deterioration rather than the humidity.

Alternatively, pp-HMDSO can be applied as interlayer material between the brittle SiO_x diffusion barrier layer and the PP substrate. Comparison of the results for the SiO_x/a-Si:C:O:N:H/a-C:N:H and the SiO_x/pp-HMDSO coating shows a very similar behavior with slightly superior barrier performances of the latter at all conditions. Moreover, pp-HMDSO provides the advantage that only one precursor needs to be employed. In order to change from interlayer to barrier layer conditions, in principle only oxygen needs to be added to the process gas mixture, while other process parameters may remain constant. The high deposition rate of pp-HMDSO is of importance with respect to the industrial applicability as short process times are aspired. As another advantage, pp-HMDSO is transparent, irrespective of its thickness, while for a-C:N:H a brownish appeal is observed if a certain thickness is exceeded. Fragmentation tests of multilayer coatings comprising a brittle SiO_x top layer show no significant increase of the COS and the CD_{sat} compared to the brittle SiO_x layer alone. This observation is consistent with experimental results and theoretical considerations by McGuigan [122] as discussed in Section 2.4.2. A CLTE of $1.8 \cdot 10^{-5}\,K^{-1}$ is reported for pp-HMDSO [107]. This value is between the CLTE of the PP substrate ($2.0 \cdot 10^{-4}\,\mathrm{K}^{-1}$) and that of SiO_2 at $0.5 - 1.0 \cdot 10^{-6}\,\mathrm{K}^{-1}$ [155, 175]. Therefore, polymeric interlayers may act as buffer layers, which reduce the thermal expansion mismatch and prevent the SiO_x diffusion barrier layer to a certain extend from cracking.

5.3.2 XPS depth profiles

XPS depth profiles of the two multilayer coatings providing the highest temperature durability on PP substrate, the SiO_x/pp-HMDSO and the SiO_x/a-Si:C:O:N:H/a-C:N:H coating, are shown in Figure 5.36 and 5.38. The top SiO_x layer of the SiO_x/pp-HMDSO multilayer coating was reduced in thickness to approximately 60 nm as determined by ellipsometry of single-layer films on Si wafers applying the same deposition parameters. In the bulk of the SiO_x top layer, constant atomic concentrations close to those of the sputter-cleaned SiO_x reference sample with $q = 30$ are obtained. Between the SiO_x and the pp-HMDSO layer a broad gradual transition in chemical composition is observed. The formation of similar extended interphases between SiO_x and carbon-rich layers is reported in the literature and ascribed to rival etching/redeposition processes [176]. This gradual interphase provides a smooth transition of material properties from the polymer-like pp-HMDSO layer to the oxidic SiO_x layer. The formation of extended interphases may account for the superior thermomechanical durability of PECVD compared to PVD derived coatings, since for PVD derived coatings the interphase appears much narrower [7]. The pp-HMDSO layer shows a high constant carbon content of approximately 40% resulting in a slightly lower C/Si ratio and a higher O/Si ratio compared to the sputter-cleaned pp-HMDSO reference sample (layer M). Higher XPS sputter rates by a factor of 1.5 are reported for pp-HMDSO compared to SiO_x in the literature [176]. A similar factor is observed comparing the respective sputter times of the SiO_x and the pp-HMDSO layer with the measured thicknesses of approximately 60 and 130 nm by means of ellipsometry and profilometry on single-layer reference samples produced at same conditions. At the pp-HMDSO/PP transition, a gradual change in composition is observed as well. The thickness of this interphase is related to the substrate roughness [159]. In this case, the interphase is rather thin affirming that the surface of

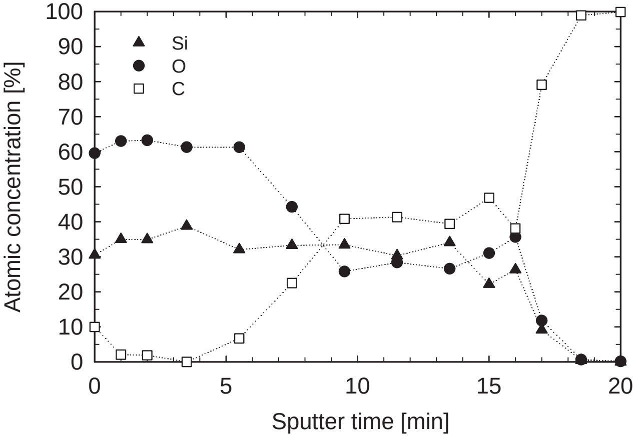

Figure 5.36: XPS depth profile of SiO_x/pp-HMDSO (layer B/M) on PP.

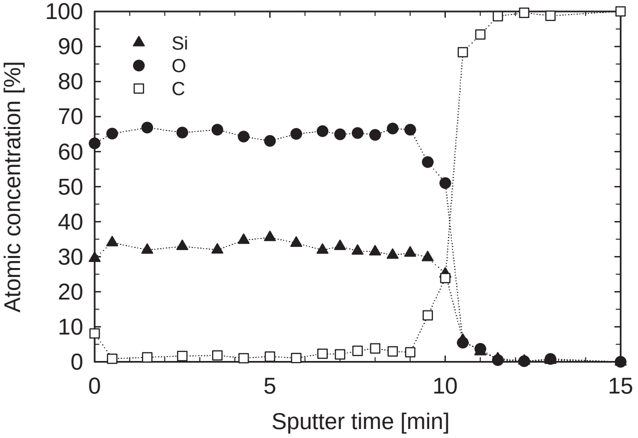

Figure 5.37: XPS depth profile of SiO_x (layer B) on PP.

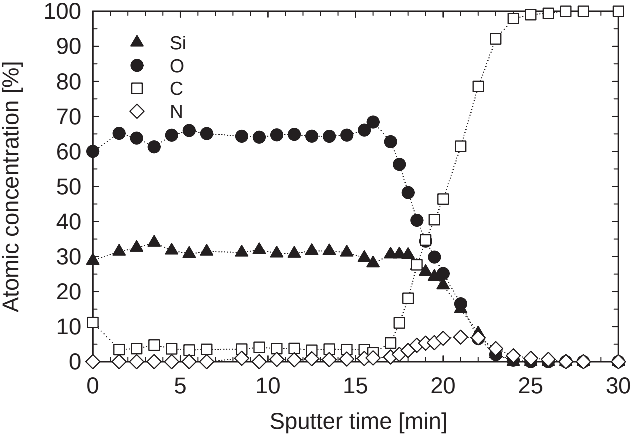

Figure 5.38: XPS depth profile of SiO_x/a-Si:C:O:N:H/a-C:N:H (layer B/N/O) on PP.

the PP foil is smooth ($S_a < 2\,\mathrm{nm}$). In Figure 5.37, the XPS depth profile of SiO_x/PP (layer B) deposited applying the same deposition time as in the SiO_x/pp-HMDSO/PP coating is shown as reference. Similar atomic concentrations are obtained as in the top layers of the multilayer coatings. Between the SiO_x coating and the PP substrate a sharp transition in atomic composition is observed with a thin interphase comparable to the pp-HMDSO/PP substrate transition in SiO_x/pp-HMDSO/PP.

For the depth profile of the SiO_x/a-Si:C:O:N:H/a-C:N:H multilayer coating, shown in Figure 5.38, the original thickness of the SiO_x barrier layer (layer B) of approximately 180 nm was applied. The a-C:N:H layer was kept as thin as possible due to the low deposition rate of a-C:N:H and its brownish appeal, which becomes noticeable for thick layers. As a consequence of the rival etching/redeposition processes, it is impossible to distinguish the thin a-C:N:H and the a-Si:C:O:N:H layer of approximately 19 and 45 nm as it is expected for the applied deposition time of 3 × 4 s, respectively. Moreover, a gradual transition with steadily decreasing silicon content, increasing carbon content, and a maximum in nitrogen content of 7% is observed.

5.4 Injection molded 2D/3D substrates

In a preliminary study, circular injection molded discs of several PP resins (homopolymers, copolymers, and block copolymers) were tested regarding their applicability as substrate for the deposition of diffusion barrier coatings with high thermal durability, since the substrate material showed to play a major role. The transferability of process conditions optimized on PP foil to injection molded 2D and 3D substrates was explored more in detail for the two most promising resins, a block copolymer (EC440) and a copolymer (RM1099).

Dry heat and sterilization tests

The application of optimized process conditions (as reported for the $\mathrm{SiO_x}$/pp-HMDSO coating on PP foil) applied on injection molded PP discs results in OTR values of approximately $20\,\mathrm{cm^3/m^2/d}$ and a severe loss of barrier performance is observed after exposure to only 100°C. Further optimization of the multilayer coating for improved temperature durability on injection molded substrates was performed. Best results regarding their temperature durability are achieved for a modified $\mathrm{SiO_x}$/pp-HMDSO coating by

- increasing t_{dep} for the pp-HMDSO layer from $3 \times 4\,\mathrm{s}$ to $6 \times 4\,\mathrm{s}$
- lowering the $\mathrm{O_2}$/HMDSO flow rate ratio for the $\mathrm{SiO_x}$ barrier layer from 30 to 25 to shift the trade-off between barrier performance and mechanical properties towards the latter
- adding thin layers below and above the $\mathrm{SiO_x}$ barrier layer with an $\mathrm{O_2}$/HMDSO flow rate ratio of 6. This results in properties between pp-HMDSO and the applied $\mathrm{SiO_x}$ barrier layer and may approach the ‘optimal’ coating structure as proposed by Schwarzer [13].

The process parameters are detailed in the Appendix in Table A.1. Results of dry heat and autoclaving tests of this multilayer coating deposited on injection molded discs of two PP grades are shown in Figure 5.39. Similar OTR values as for the single $\mathrm{SiO_x}$ coating of approximately $20\,\mathrm{cm^3/m^2/d}$ are measured directly after deposition, while the

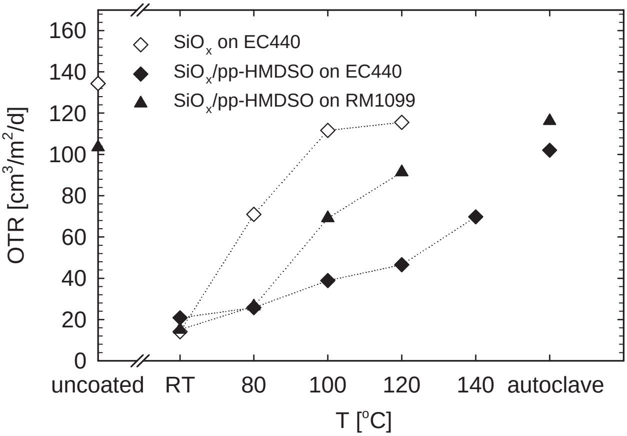

Figure 5.39: OTR of single- and multilayer coatings on injection molded PP discs after deposition, after 30 min at 80, 100, 120, 140°C, and after 30 min autoclaving at 121°C and 2.1 bar of steam.

multilayer coating provides a considerably lower OTR on the block copolymer (EC440) than on the copolymer (RM1099) after exposure to elevated temperatures. Even more evident is the improvement in temperature durability for the optimized multilayer coating compared to the single-layer SiO$_x$ coating both on EC440 substrate. Severe deterioration of barrier performance of the single-layer SiO$_x$ coating appears after exposure to only 80°C. Nevertheless, after exposure to 140°C or after autoclaving a loss of barrier performance is inevitable also for the optimized multilayer coating in combination with the most suitable injection molded substrate.

Differential scanning calorimetry

The phase transitions of the different PP grades are explored by DSC. In Figure 5.40, DSC thermograms of the applied PP grades are compared with the thermogram of the PP foil. The peak fusion temperature of RM1099 is determined to 138°C with an onset temperature of 122°C,

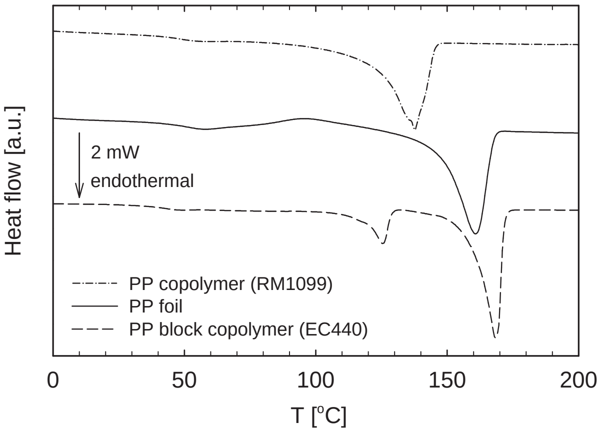

Figure 5.40: DSC thermogram of PP injection molding resins, block copolymer (EC440) and copolymer (RM1099), and of PP foil at a heating rate of 10 K/min.

while a considerably higher peak fusion temperature of 161°C is found for the PP foil. A low fusion onset temperature, close to the temperature experienced in the deposition process or the autoclave, has an adverse effect and may be related to the observed inferior temperature durability of coatings on the RM1099 PP substrate. In the thermogram of the block copolymer (EC440) two distinct endothermal peaks are observed at 125°C and 168°C, of which the latter is the more prominent one. The peak fusion temperature of the smaller first transition, corresponding to the component of the block copolymer with the lower melting temperature, is in the range of the sterilization temperature as well, whereas the peak fusion temperature of the main component even exceeds the peak fusion temperature of the PP foil. The high peak fusion temperature of the main component seems to be beneficial for the use as substrate regarding the thermomechanical properties of the composite.

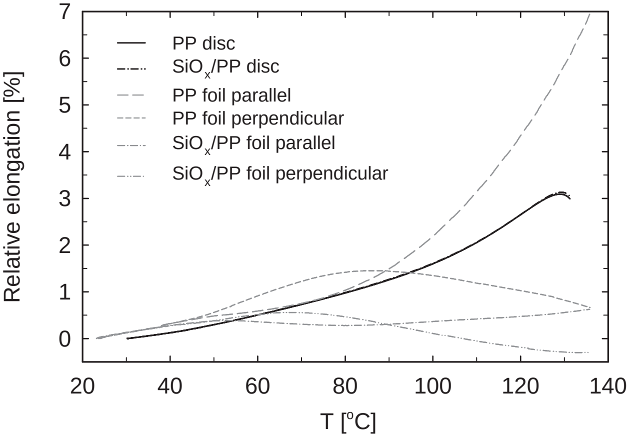

Figure 5.41: Dilatometry analysis of uncoated and SiO$_x$ coated injection molded PP discs (RM1099) compared to results obtained on PP foil.

Dilatometry analysis

Results from dilatometry analysis of uncoated and SiO$_x$ coated injection molded PP substrate (RM1099) are compared to corresponding results of the PP foil in Figure 5.41. The dilatometry behavior of the injection molded substrate is isotropic with an elongation at elevated temperatures between the elongations of the PP foil in machine direction and perpendicular to machine direction. Unfortunately, corresponding results of the block copolymer, which could explain the improved temperature durability, are not available here. In contrast to the PP foil, the expansion of the injection molded disc is not affected by the SiO$_x$ coating. The cohesive strength of the SiO$_x$ coating, high enough to prevent expansion of the 30 μm thick PP foil, is not sufficient for the 400 μm thick injection molded substrate material. In general, this discrepancy needs to be considered for the transfer of results from PP foil to the injection molded substrates.

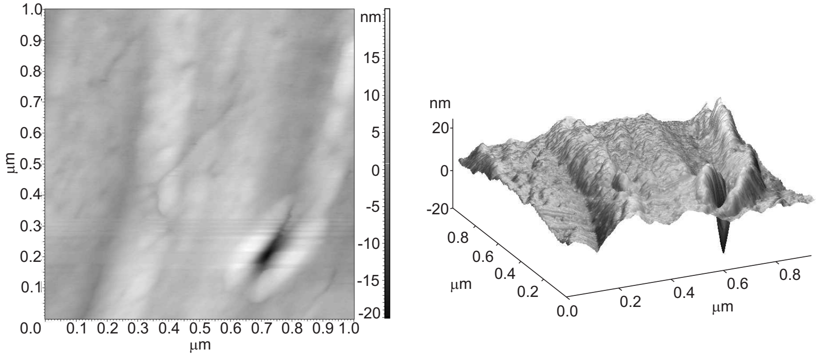

Figure 5.42: Atomic force micrograph of uncoated injection molded substrate (RM1099), $S_a = 2.7\,\mathrm{nm}$.

Morphological analysis

The quality of a coating also depends on the surface morphology of the substrate. An atomic force micrograph of a representative uncoated injection molded PP sample (RM1099) is depicted in Figure 5.42. A higher average roughness of 2.7 nm is evidenced compared to 1.7 nm of the PP foil. The increased roughness is caused by characteristic surface flaws as observed in the lower right section of the AFM image. These surface flaws are frequently found on the injection molded substrate surface and may originate from the injection molding form of the manufacturing process. Additionally, a certain waviness is evident with a spacing of approximately 0.5 μm, presumably due to residual traces from polishing. While the waviness is not crucial for the deposition process, the flaws may induce additional defects in the coating and result in a higher OTR of the coatings on injection molded substrates.

Homogeneity of deposition on 3D substrates

The homogeneity of deposition is investigated on a model substrate container as a first step towards the deposition of 3D substrates. For the successful deposition of diffusion barrier coatings on 3D substrates, sufficient coating thickness is required, i.e. at least the critical thickness,

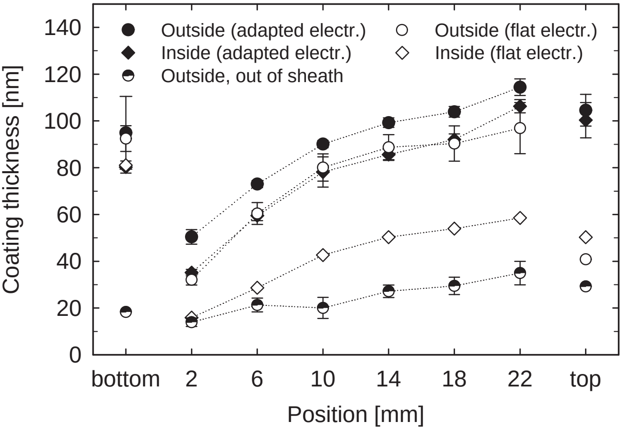

Figure 5.43: Homogeneity of $\mathrm{SiO_x}$ coating thickness on the outside and the inside of the polymer container applying adapted electrodes ($P_{RF} = 100\,\mathrm{W}$, $\dot{V}_{\mathrm{HMDSO}} = 2\,\mathrm{sccm}$, $\dot{V}_{\mathrm{O_2}} = 60\,\mathrm{sccm}$, $t_{dep} = 60\,\mathrm{s}$) compared to the deposition of the container in and out out of the plasma sheath on the flat electrode.

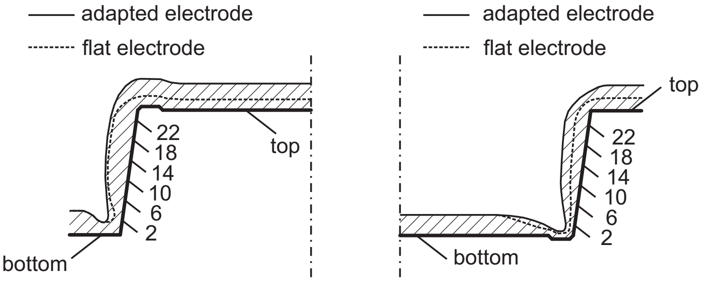

(a) Outside coating (b) Inside coating

Figure 5.44: Positions for coating thickness homogeneity measurements on PP food container substrate with schematic representation of the coating thickness distribution.

at every position of the substrate. The critical thickness is expected to depend on the substrate roughness. For the injection molded substrates it may exceed the critical thickness of 12 nm determined for the PP foil. The homogeneous deposition of the side walls is particularly problematic. The formation of a sheath region over the RF powered electrode and the related self-bias voltage are essential for the deposition of dense $\mathrm{SiO_x}$ coatings with good diffusion barrier performance. To influence the shape of the sheath, adapted electrodes, matching the container geometry, are used for the coating of the outside and the inside of the container, respectively. The influence of these electrodes and the influence of the sheath on the coating thickness homogeneity is shown in Figure 5.43 for the outside and inside deposition of the container at constant process conditions ($P_{RF} = 100\,\mathrm{W}$, $\dot{V}_{\mathrm{HMDSO}} = 2\,\mathrm{sccm}$, $q = 30$, $t_{dep} = 60\,\mathrm{s}$). A coating thickness of approximately 160 nm is obtained on the 30 μm PP foil at these conditions. The measurement positions are schematically illustrated in Figure 5.44 for the outside and the inside deposition of the substrate container. Results support the importance of the plasma sheath, since only a very low coating thickness, even though the most homogeneous one, is achieved if the polymer container is positioned apart from the flat RF electrode by spacers out of the plasma sheath region. In general, the deposition on the outside of the container, which is also the favored one to avoid direct contact of the coating and the packaging content, results in a higher coating thickness compared to the inside. The adaptation of the electrode geometry proved to be beneficial for the deposition at all positions compared to the flat electrode geometry. The improvement is more pronounced in the case of the inside deposition. Surprisingly, for the outside deposition of the container relatively high coating thicknesses are also achieved on the side walls without the adapted electrode. The difference in coating thickness of the flat and the adapted electrode setup is most obvious at the top. Here, very low deposition rates are achieved with the flat electrode setup, since in this case the top protrudes from the plasma sheath. Unfortunately, the top position corresponds to the base area for the outside deposition, which accounts for the main fraction of the total area of the container. Towards the lower edge (i.e. the position 2 mm from the bottom), a drop in coating thickness is observed for all configurations, which may be related to the influence of the flow field and the deflection of ions towards the horizontal surface due to the bias voltage. Nevertheless, the application of adapted electrodes yields coating thicknesses well above the critical coating thickness at all positions. Especially at the top, the homogeneity is improved significantly. This also affects the barrier performance of SiO_x coated PP containers. The OTR is reduced from 99.6 to 11.6 $cm^3/m^2/d$ by deposition of the PP container on the outside with the adapted electrode, while the deposition applying the same parameters without adapted electrode leads to an inferior barrier coating with an OTR of 63.5 $cm^3/m^2/d$.

Lacquer application

For mechanical protection of the coating, i.e. to prevent scratching during life cycle of the packaging, a protective lacquer layer is applied, since this step is also intended for the industrial application of the process. Moreover, OTR measurements on injection molded PP discs showed that barrier performance of the as-deposited coatings and, more importantly, after exposure to elevated temperatures is not satisfactory due to the higher demands on the coating of injection molded substrates compared to PP foil. By application of sol-gel derived ORMOCER materials on SiO_x coatings, a synergistic improvement of barrier performance can be achieved as well as good adhesion, scratch and abrasion resistance [177]. Thermally curable systems can be synthesized as well as UV curable ORMOCER lacquers. Apart from these advantages, for industrial application the recovery of the overspray, a low content of solvent, and, for applications in contact with food products, reduced emission and ecological compatibility are desired. Therefore, also a commercial cationic epoxy resin lacquer (HOBA Lacke und Farben GmbH, Germany) combining these properties was tested for its applicability on SiO_x coatings. The wetting properties of the lacquer on the SiO_x coating is an important issue. Preliminary tests showed that for the ORMOCER lacquer a high surface free energy of the coating surface is favorable. The wetting is significantly improved by short exposure of the SiO_x coating to a pure O_2 plasma after deposition and directly before spraying of the ORMOCER lacquer (contact angle of ORMOCER lacquer not measurable). On the contrary, best results are obtained for the commercial lacquer if it is directly applied on SiO_x coatings with q in the range of $15 - 30$. The OTR of uncoated, lacquer coated, SiO_x/pp-HMDSO coated, and

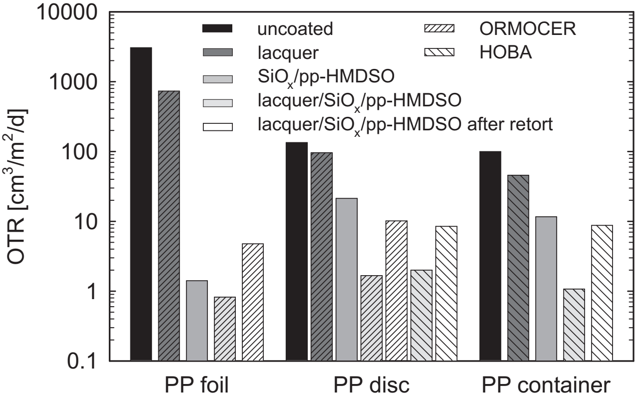

Figure 5.45: Oxygen transmission rate of uncoated, lacquer, SiO_x/pp-HMDSO, and lacquer/SiO_x/pp-HMDSO coated PP foil, PP disc, and PP container (EC440) before and after autoclaving.

lacquer/SiO_x/pp-HMDSO coated substrates is compared before and after retort for different PP substrates in terms of best achieved values in Figure 5.45. The application of the lacquer directly on the substrates (after pretreatment to enable wetting) shows only minor barrier improvement for all investigated substrates and lacquers. A synergistic barrier improvement effect is observed by applying a lacquer layer on top of the SiO_x coating. This effect is more pronounced for the injection molded PP substrates compared to the PP foil and may be related to a higher residual defect density or a larger average defect size of the SiO_x coating on the injection molded substrates, since the lacquers reduce the deteriorative effect of the defects by covering or even filling the macroscopic defects in the SiO_x film as proposed in the literature [15]. Applying a thermally curable inorganic-organic polymer system on SiO_x, an even more pronounced synergistic permeation reduction from 1620 to below $0.05\,cm^3/m^2/d$ was achieved on BOPP film by Amberg-Schwab and Hoffmann. They ascribed it to the compensation of macroscopic defects and the formation of covalent Si-O-Si bonds at the hybrid polymer/SiO_x interface leading to a high inorganic network density. A similar OTR of approximately $2\,\mathrm{cm}^3/\mathrm{m}^2/\mathrm{d}$ is reached with the ORMOCER and the commercial lacquer on injection molded PP discs in the best case. Accordingly, a similar improvement of the thermomechanical properties is observed for the two investigated lacquers. While retort induced a severe increase in OTR for the $\mathrm{SiO_x}$/pp-HMDSO coating on injection molded PP discs up to the level of the uncoated substrate, autoclaving with an additional protective lacquer layer results in an OTR of approximately $10\,\mathrm{cm}^3/\mathrm{m}^2/\mathrm{d}$. The improvement in thermomechanical properties, accompanying the enhanced barrier performance, may be related to the formation of highly crosslinked regions within the flaws of the $\mathrm{SiO_x}$ coating, which prevent crack initiation under thermal stress. This effect is referred to as 'flaw healing' in the literature [178]. Since the ORMOCER lacquer showed no advantage over the commercial lacquer on injection molded PP discs, neither regarding the barrier nor the thermomechanical properties, only the commercial lacquer was explored for the PP containers due to its better industrial applicability. Further improvement of the overall barrier performance of the commercial lacquer/$\mathrm{SiO_x}$/pp-HMDSO coating on the PP container (EC440) is achieved by reducing P_{RF} and increasing t_{dep} to 180 s at constant $CP = 50\,\mathrm{W/sccm}$ and $q = 30$ for the more temperature-sensitive injection molded substrates. The lowest OTR values achieved at these conditions are reported in Figure 5.45 for the outside deposition of the PP container with the adapted electrode. Very similar results are achieved on the PP container and the flat injection molded PP substrate before and after lacquer application as well as after retort. The combination of the optimized $\mathrm{SiO_x}$/pp-HMDSO coating with a commercial UV curable lacquer results in an OTR of $1.7 \pm 0.5\,\mathrm{cm}^3/\mathrm{m}^2/\mathrm{d}$ on the 3D substrate. The lowest achieved OTR corresponds to $0.01\,\mathrm{cm}^3/\mathrm{pack}/\mathrm{d}$ and meets the requirements for most food packaging applications [1, 12, 83].

Chapter 6

CFD modeling

6.1 Introduction

For the design of PECVD reactors, fluid dynamics is a relevant aspect. Coating inhomogeneities may be related to a nonuniform gas velocity and unfavorable flow conditions in the vicinity of the substrate. Incomplete mixing of the process gases, especially in the case of complex (3D) substrate geometries, small reactor dimensions, or inadequate gas distribution in the reactor volume may result in a nonuniform coating composition. Modeling of plasma processes is in general rather complex due to the electrostatic interactions of electrons and ions and the influence of the plasma on the (thermophysical) material properties. The simultaneous solution of the partial differential equations to capture the flow field (Navier-Stokes equations) and the electric field distribution (Poisson equation) is computationally still not traceable for technically relevant problems. Another difficulty arises from the multitude of neutral and charged species which are involved in several homo- and heterogeneous reactions with mostly unknown rate constants. To overcome these problems, the calculation of the flow and the electric field was performed separately and combined in a cascade approach with still considerable computational effort in the literature [179]. Reducing the number of reactions to a few homo- and heterogeneous model reactions shows often only limited success in the prediction of experimental data, e.g. coating thickness distributions [180]. Alternatively, (semi-)empirical models are employed to fit the reaction rates to experimental data [181]. This may result in unreliable predictions for operating conditions which are not in the range of the provided experimental data.

In this work, the modeling effort was therefore restricted to computational fluid dynamics (CFD) simulations as a valuable tool for the evaluation of the flow field, i.e. the steady-state condition ‘before plasma ignition’, of the existing reactor geometry and for the proposal of new reactor designs. The Knudsen number, which is determined from the mean free path and a characteristic length scale according to Equation 2.7, is a dimensionless quantity for the characterization of the flow regime. Considering the reactor diameter of 160 mm as characteristic length and a pressure of 10 Pa the Knudsen number is $Kn = 0.005 < 0.1$. Therefore, the physical laws of continuum mechanics are still valid. Reynolds numbers are typically below 10 in the applied flow rate range and laminar flow can be assumed (Equation 2.8). Furthermore, gases are assumed ideal and viscous heating due to dissipation is neglected, since velocity gradients are expected to be small.

6.2 Reactor design and mesh generation

6.2.1 Existing reactor geometry

A detailed 3D model of the existing laboratory scale reactor, shown in Figure 6.1, was built. The total volume of the reactor amounts to 19.4 l. Due to symmetry reasons, only half of the reactor volume was modeled to reduce the number of cells to 4 437 111. A tetrahedral scheme with low skewness of the cells was applied. The grid was refined in the vicinity of the substrate and the gas shower inlet holes.

6.2.2 Adapted reactor designs

Based on the following criteria, two adapted reactor geometries are designed to improve the process regarding its industrial applicability:

(1) The exhaust gas outlet, connected to the pumping unit, is arranged symmetrically to assure symmetric flow conditions.

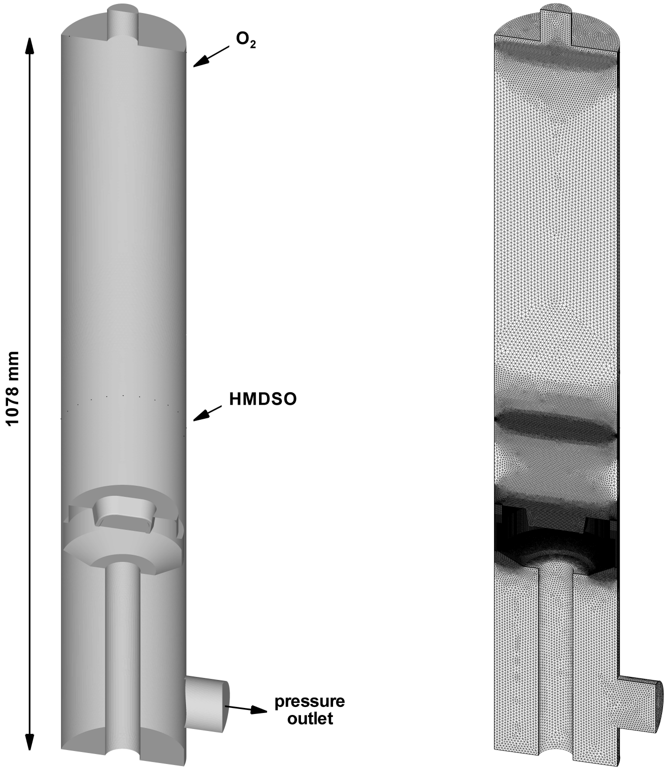

(a) Geometry (b) Mesh

Figure 6.1: Geometry and mesh of existing labscale reactor.

(2) The substrate is placed in the reactor with the surface to be coated facing downwards to reduce dust sedimentation on the substrate.

(3) The reactor volume is reduced to shorten the pump-down time until the base pressure is reached.

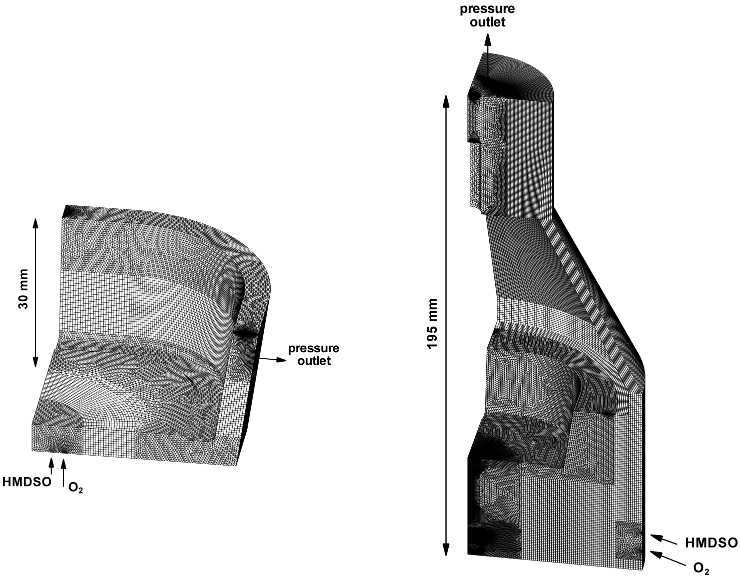

(a) Design A (b) Design B

Figure 6.2: Mesh of adapted reactor designs.

The mesh of Design A and B is illustrated in Figure 6.2. In Design A, the reactor volume is drastically reduced to 0.067 l. It basically consists of an approximately 5 mm wide gap surrounding the substrate. Design B provides more space for mixing of the process gas components resulting in a total reactor volume of 1.0 l. Here, the cross section is reduced above the substrate towards the pump similar to the design of the laboratory reactor. A mesh consisting of 410 305 cells was generated for Design A, while 2 676 888 cells were applied for Design B. A structured (map) scheme was used where applicable and a tetrahedral scheme with low skewness of the cells elsewhere. In both cases, only a quarter of the reactor volume was modeled and symmetric boundary conditions were applied due to the additional symmetry provided by the exhaust outlet.

6.3 Numerical details

The 3D Navier-Stokes equations for steady laminar flow of viscous compressible multicomponent (O_2-HMDSO) mixtures were solved in the whole reactor domain for all models. The discretization of the conservation equations for mass, momentum, energy, and the mass concentration of the species was implemented by a second order upwind scheme. The calculations were performed with the commercial fluid modeling software package FLUENT 6.3.26 (ANSYS, Inc., USA) with the geometry and mesh generation software GAMBIT 2.2.30 on a 64-bit Dell Precision T7400 workstation equipped with four 2.66 GHz processors and 16 GB RAM until the convergence criterion (residuals below 10^{-3}) was reached.

6.4 Material properties and boundary conditions

Material properties of HMDSO and oxygen were derived from the Chemical Properties Handbook [182] and from the Fluent database. The heat capacity, the thermal conductivity, and the dynamic viscosity are implemented as higher order polynomials as a function of the temperature, which are reported in Table A.2 in the Appendix. The values for the molar mass of oxygen and HMDSO are given in Table 3.1. The heat capacity, the thermal conductivity, and the viscosity of the mixture was calculated applying a (mass-weighted) mixing law for the components oxygen and HMDSO. Ideal gas behavior of the mixture was assumed for the density. The mass diffusivity was calculated applying the Chapman-Enskog-Wilke-Lee model [183] using the process modeling tool Aspen Plus (Aspen Technology, Inc., USA). The linear fit to the resulting data in the temperature range of interest is also reported in Table A.2 in the Appendix.

In a preliminary study on a detailed model of the gas shower including the supply to the distributor ring, which contains the injection holes, it was shown that a uniform distribution of the monomer is achieved. Therefore, the inlet boundary condition was defined as a mass flow rate for oxygen and HMDSO, equally distributed over the injection holes of the gas shower. The mass flow rate was calculated from the volumetric flow rate for $i = \mathrm{O_2}$ and HMDSO according to

$$\dot{m}_i = \frac{p_{\mathrm{STP}} \cdot \dot{V}_i \cdot M_i}{\Re \cdot T_{\mathrm{STP}}}, \tag{6.1}$$

where T_{STP} and p_{STP} are the standard temperature and pressure. For the applied volumetric flow rates of $\dot{V}_{\mathrm{O_2}} = 60\,\mathrm{sccm}$ and $\dot{V}_{\mathrm{HMDSO}} = 2\,\mathrm{sccm}$, mass flow rates are calculated to be $\dot{m}_{\mathrm{O_2}} = 1.4 \cdot 10^{-6}\,\mathrm{kg/s}$ and $\dot{m}_{\mathrm{HMDSO}} = 2.4 \cdot 10^{-7}\,\mathrm{kg/s}$. In the model of the existing reactor, oxygen and HMDSO are introduced to the reactor via 10 and 24 injection holes of 1.0 and 0.6 mm in diameter, equally distributed over the circumference. The mass flow is directed downwards by 45°. In Design A, oxygen and HMDSO are introduced through 8 and 6 injection holes of 0.5 and 1.0 mm from the bottom pointing vertically upwards, while in Design B 12 inlet holes of 0.5 and 1.0 mm in diameter are provided on the circumference for oxygen and HMDSO, respectively. Here, the mass flow is oriented upwards by 45°. At the outlet a constant (gauge) pressure of 10 Pa is defined with the constant off-gas composition of the perfect mixture (2 sccm HMDSO in 60 sccm $\mathrm{O_2}$ corresponds to a HMDSO concentration of $c_{\mathrm{HMDSO}} = 0.145\,\mathrm{wt.\%}$). While in the existing reactor model the outlet is asymmetrically placed at the side wall of the bottom part, the exhaust gas is pumped-off through 8 circular holes at the top part of the side wall in Design A and through a central outlet at the top in Design B. A constant wall temperature of 50°C was applied for the heated walls and 25°C elsewhere. Symmetric boundary conditions were defined for the vertical surfaces representing no walls. The magnitude of the velocity vector $|\mathbf{v}|$ was calculated according to

$$|\mathbf{v}| = \sqrt{v_x^2 + v_y^2 + v_z^2}, \tag{6.2}$$

where v_x, v_y, and v_z are the components of the velocity vector $\mathbf{v}$ in x, y, and z direction.

6.5 Results and discussion

Velocity and HMDSO concentration fields are shown in Figure 6.3 for the existing reactor model in cross-sectional planes. After expansion of

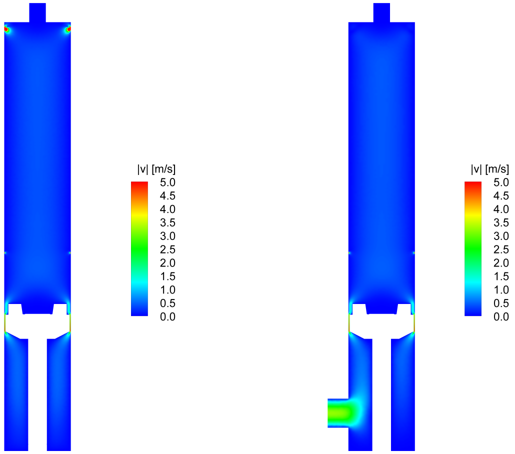

(a) Magnitude of velocity (xz-plane)

(b) Magnitude of velocity (yz-plane)

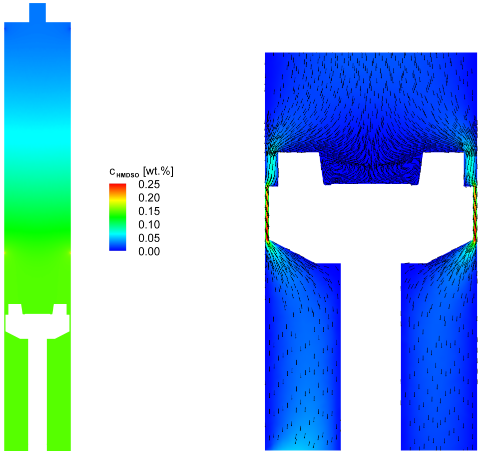

(c) HMDSO concentration (xz-plane)

(d) Velocity vectors (vicinity of substrate holder, yz-plane)

Figure 6.3: Magnitude of velocity and HMDSO concentration field for the existing reactor geometry (for inside coating of the container).

the gas through the injection holes of the gas shower, the gas is decelerated within a short distance as seen in the plot of the xz-plane in Figure 6.3(a). The magnitude of velocity is below 0.3 m/s in the vicinity of the substrate. Therefore, no disturbing effects on the deposition process may be expected. Despite the asymmetric exhaust gas outlet, a symmetric velocity field is obtained in and above the annulus around the substrate holder as shown in Figure 6.3(b). From the HMDSO concentration field of the O_2-HMDSO mixture, depicted in Figure 6.3(c), it is evident that the top of the reactor is not reached by HMDSO. This is in agreement with observations from experiments, since wall deposits are only found up to the middle of the MW cylinder. This coincides with the position in height of a rapid decrease in HMDSO concentration. A backflow is observed in the volume of the substrate container, but velocities are very small as seen in Figure 6.3(d). This is one reason for the observed inhomogeneity in coating thickness, which decreases towards the lower edge of the container (Figure 5.43).

The velocity field of Design A is shown in Figure 6.4(a) as a contour plot of the magnitude of velocity $|\mathbf{v}|$. The drastic reduction in reactor volume leads to high velocities in the vicinity of the substrate and may have a deteriorative effect on the deposition process as the flow is directed parallel to the substrate surface. Moreover, coating thickness and composition inhomogeneities may occur, particularly in the center of the container, due to the insufficient distance between the gas injection holes of the gas shower and the substrate surface for mixing of the process gases (Figure 6.4(b)). On the contrary, similar flow conditions as for the existing reactor geometry are observed for Design B in Figure 6.4(c). Sufficient space is given for expansion and deceleration of the process gases. Good mixing of oxygen and HMDSO is ensured after expansion through the injection holes of the gas shower as seen in Figure 6.4(d). This reactor design combines a small reactor volume, enabling a short pump-down time, while the flow conditions are not considerably changed and good mixing of the process gases is still provided.

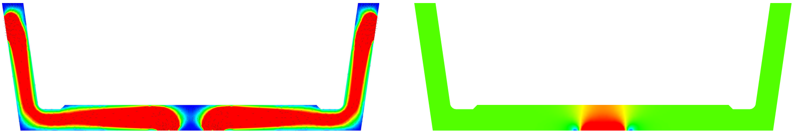

(a) Design A, magnitude of velocity (b) Design A, HMDSO concentration

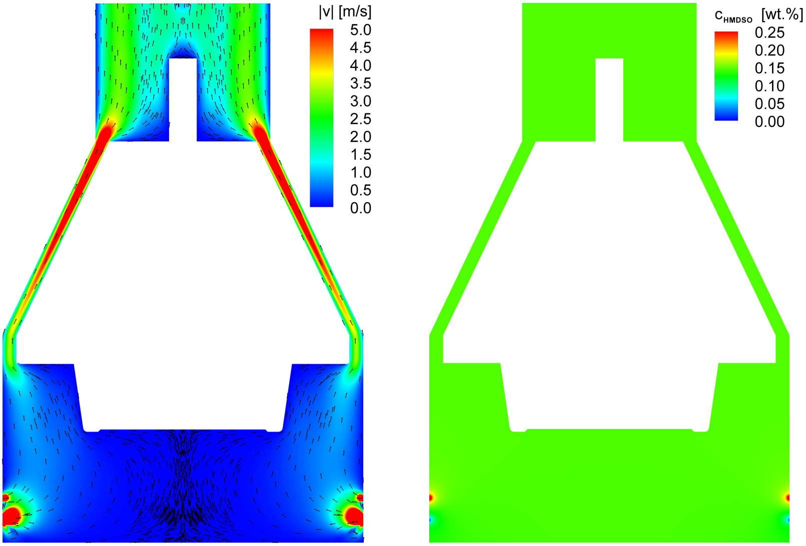

(c) Design B, magnitude of velocity (d) Design B, HMDSO concentration

Figure 6.4: Magnitude of velocity and HMDSO concentration field of adapted reactor designs (for outside coating of the container).

Chapter 7

Conclusions

Investigation of PECVD process for SiO_x deposition on PP

In order to achieve SiO_x coatings from O_2-HMDSO mixtures on PP substrate with good diffusion barrier performance, special attention must be paid to the thermal load during deposition due to the high thermal expansion and the low glass transition temperature of PP. Therefore, discontinuous deposition at low RF power is favorable for PP, while for the deposition on PET the substrate temperature is much less crucial. For the case that the thermal load is not the limiting factor, the RF power may not be considered independent from the monomer flow rate. It was shown that the energy per mass of monomer, here expressed by the composite parameter $CP = P_{RF}/\dot{V}_{\mathrm{HMDSO}}$, is applicable for the description of plasma conditions at constant q with regard to barrier performance and chemical structure of the resulting films. A threshold value of $50\,\mathrm{W/sccm}$, corresponding to 4.1×10^5 J/g, was found (at $q = 30$) to be exceeded for adequate fragmentation of the precursor, low carbon and silanol content in the film, and, therefore, good diffusion barrier performance. Increasing the composite parameter, either by increasing P_{RF} or by lowering $\dot{V}_{\mathrm{HMDSO}}$, results in more SiO_2-like films with low carbon content. Considering the conversion ratio $CR = R/\dot{V}_{\mathrm{HMDSO}}$, a transition from an energy-deficient to a monomer-deficient regime is noticed at $CP = 50\,\mathrm{W/sccm}$.

Similar effects, as for CP, are observed for the O_2/HMDSO flow rate ratio q. In order to obtain SiO_2-like coatings with good diffusion barrier properties, low P_{RF} (and CP) can be compensated by high values of q. On the other hand, lower values of q are favorable at high P_{RF}. Substrate temperature is mainly dependent on P_{RF}, but high oxygen contents further increase the substrate temperature and deteriorate barrier performance. Mechanical and structural coating properties are modified significantly by changing q. At high oxygen dilution, brittle, SiO_2-like coatings with high mass and network density, high compressive stress and good barrier performance are obtained. An increase of $q > 30$ does not succeed in further improvement of barrier performance. At these conditions the coating is virtually carbon-free with an atomic composition of $SiO_{1.9}C_{0.03}$. A high density of $2.1\,g/cm^3$ and a high compressive stress of $-487\,MPa$ are determined at these conditions accompanied by a low COS of only 0.9%. Pure HMDSO feed to the discharge results in polymer-like coatings with a high carbon content showing an atomic composition of $SiO_{0.7}C_{1.7}$. FTIR spectra revealed pronounced absorptions of CH_x, $Si\text{-}(CH_3)_x$ and Si-H species, while the Si-O-Si peak intensity is drastically reduced and the peak position is shifted towards lower wavenumbers. This indicates a low Si-O network density as a result of low monomer fragmentation. For these coatings, referred to as pp-HMDSO, a low internal stress is measured accompanied by a low mass density of $1.2\,g/cm^3$. Fragmentation tests on pp-HMDSO coatings indicate a high COS of 18% and a high CD_{sat} of $1300\,mm^{-1}$. Estimates of the fracture toughness and the IFSS are found to be close to $80\,J/m^2$ and 160 MPa, i.e., four and six times higher than the respective values for the SiO_x coating. Therefore, the obtained pp-HMDSO coatings show excellent cohesive and adhesive properties. Unfortunately, these properties of pp-HMDSO are achieved at the expense of barrier performance.

The dependence of the OTR on the coating thickness follows a very similar trend for PP and PET substrate. For both substrates the OTR decreases by more than one order of magnitude, if a critical coating thickness of approximately 12 nm is exceeded. Further increase of coating thickness results in an asymptotic behavior of the barrier performance with a residual OTR of 0.3 ± 0.1 and $5.1 \pm 3.6\,cm^3/m^2/d$ on PET and PP substrate, respectively. Defect densities, determined on chemically etched PET and PP substrate through SiO_x coatings, decrease from 4000 to 40 mm^{-2} as the coating thickness is increased from 6 to 180 nm. Good agreement of measured and calculated OTR values is obtained by means of simple calculations from the determined defect densities with an average defect size of 0.8 μm for PET and 0.5 μm for PP even below the critical coating thickness. Therefore, the permeation can be attributed to defects, even at the early stage of deposition. The hypothesis of permeation through defects is supported by the activated rate theory. The apparent activation energy of oxygen permeation remains unchanged by the deposition of SiO_x on both substrates and is well below typical values for fused silica.

Multilayer coatings

A multilayer approach is followed in order to improve the temperature durability of diffusion barrier coatings for autoclaving. Thin carbon-rich interlayers, such as a-C:N:H from mixtures of N_2 and C_2H_2 or coatings from N_2, C_2H_2, and HMDSO, are capable of efficiently improving temperature durability, even for substrates showing high thermal expansion such as PP. Nitrogen incorporation in a-C:H, which was evidenced by ATR-FTIR spectroscopy, reduces the over-constraining of the carbon network by the formation of terminating groups. This reduces stress and hardness of the coating and may account for the high crack onset strain of a-C:N:H as well as for the low OTR of the SiO_x/a-SiC:O:N:H/a-C:N:H coating after exposure to 140°C of 22 cm^3/m^2/d. The same conditions result in a severe loss of barrier performance of the respective single SiO_x coating with an OTR of $>$ 1000 cm^3/m^2/d due to the formation of cracks. These cracks are formed perpendicular to machine direction of the PP substrate, for which the highest relative elongation is observed by means of dilatometry analysis. The thermal expansion is significantly reduced by the SiO_x coating, which is evidence for its good adhesive and cohesive properties.

Alternatively, pp-HMDSO interlayers efficiently improve temperature durability during autoclaving by crack prevention of the SiO_x diffusion barrier layer. After exposure to 140°C only a minor loss of barrier performance from 5 to 18 cm^3/m^2/d is observed. Plasma polymerized HMDSO interlayers show several advantages over the alternative interlayer materials a-C:N:H and a-Si:C:O:N:H. Shorter deposition times can be realized due to the much higher deposition rate of 710 nm/min compared to only 110 nm/min for a-C:N:H. Unlike a-C:N:H, pp-HMDSO is transparent irrespective of the interlayer thickness. Furthermore, the SiO_x/pp-HMDSO coating can be deposited with HMDSO as the only precursor at constant P_{RF} by simply adding oxygen in a one-stage process. A broad gradual transition in chemical composition is observed in the XPS depth profile of the SiO_x/pp-HMDSO coating between pp-HMDSO and SiO_x because of rival etching/redeposition processes. The gradual transition in material properties provides improved stress distribution and, therefore, prevents cracking of the SiO_x layer when subjected to thermal cycling.

Coating of 3D injection molded substrates

Improved temperature durability is achieved by further optimization of process conditions of SiO_x/pp-HMDSO coatings for injection molded substrates. Affirming the great importance of the substrate, the choice of PP grade is crucial for the temperature durability of the composite. A PP block copolymer proved to be more suitable than PP co- and homopolymers. Nevertheless, after autoclaving no satisfactory barrier performance is achieved. Dilatometry analysis shows that the coating does not influence the thermal expansion behavior of the injection molded substrate due to the much greater substrate thickness compared to the thin PP foil of approximately 400 μm. A relative elongation of 3% is determined at 130°C. The homogeneity of the coating thickness on 3D substrates is significantly improved by adaptation of the electrode to the substrate geometry as the plasma sheath formation is influenced. Applying the adapted electrode, comparable barrier performance is achieved on 2D and 3D injection molded PP substrate. The application of a protective lacquer on the multilayer barrier coating results in a synergistic barrier improvement effect and enhanced thermal durability. A low OTR of $1.7 \pm 0.5\,\mathrm{cm^3/m^2/d} = 0.017\,\mathrm{cm^3/pack/d}$, sufficient for most food packaging applications, is achieved on injection molded PP containers applying a commercially available, UV curable lacquer on the optimized SiO_x/pp-HMDSO coating. This composite withstands standard thermal sterilization cycling at 121°C with minor deterioration of barrier properties.

CFD calculations show that the reactor volume may be reduced from

19 to 1 l without considerably changing flow conditions in order to achieve a shorter pump-down time for industrial application.

For further improvement of the process or for transfer to other applications and requirements, an integral consideration of the problem, starting with the choice of substrate material, the optimization of the (multilayer) coating for the specific substrate, and, where appropriate, the application of a protective lacquer layer is necessary to find the best solution.

Appendix A

A.1 Drawings

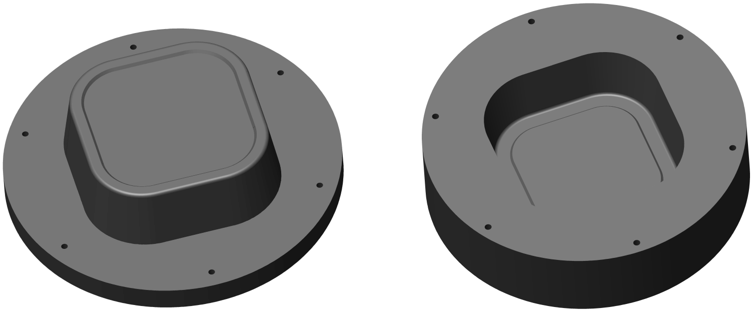

(a) Outside coating (b) Inside coating

Figure A.1: Adapted electrode geometries for the outside and the inside coating of PP model substrate containers.

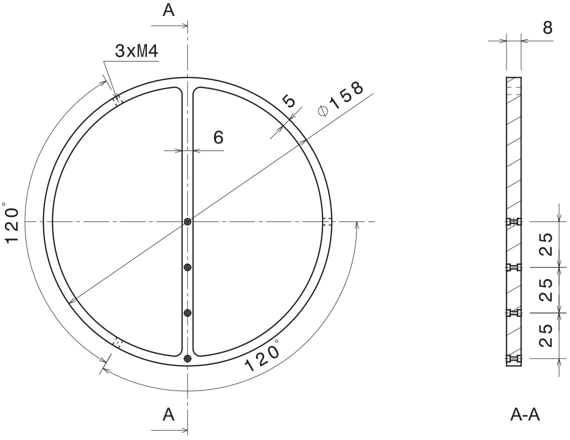

Figure A.2: Front and sectional view of fiber-optical thermal probe fixture for temperature measurements in the gas phase made of PEEK.

A.2 Matching network

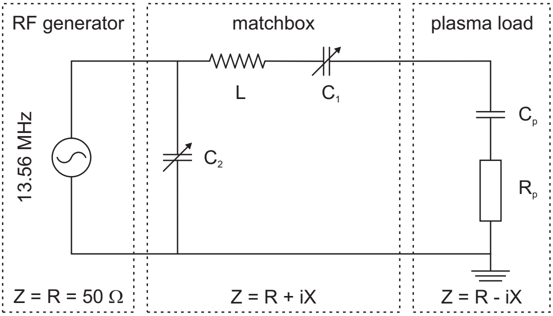

Figure A.3: Schematic diagram of impedance matching network. To minimize the reflected RF power, the impedance of the matchbox is adapted by two tunable capacitors C_1 and C_2 so that it corresponds to the complex conjugate of the plasma load. This enables matching of the purely resistive impedance of the RF generator ($R = 50\,\Omega$) to the reactor impedance.

A.3 Experimental data

Table A.1: Deposition parameters for SiO_x/pp-HMDSO coating with improved temperature durability on injection molded discs.

Layer	P_{RF} [W]	$\dot{V}_{\text{HMDSO}}$ [sccm]	q [-]	p [Pa]	t_{dep} [s]
1 (top)	100	10	6	10	3 × 4
2	100	2	25	10	12 × 4
3	100	10	6	10	3 × 4
4 (bottom)	100	10	0	10	6 × 4

A.4 Material properties for CFD modeling

Table A.2: Material properties of O_2 and HMDSO for CFD simulations.

Material data for O_2	Fluent database
Heat capacity [J/kg/K]	$8.11 \cdot 10^2 + 4.11 \cdot 10^{-1}T - 1.75 \cdot 10^{-4}T^2$ $+3.76 \cdot 10^{-8}T^3 - 2.97 \cdot 10^{-12}T^4$
Thermal conductivity [W/m/K]	$3.92 \cdot 10^{-3} + 8.08 \cdot 10^{-5}T - 1.35 \cdot 10^{-8}T^2$ $-2.22 \cdot 10^{-12}T^3 - 1.42 \cdot 10^{-16}T^4$
Dynamic viscosity [kg/m/s]	$7.88 \cdot 10^{-6} + 4.92 \cdot 10^{-8}T - 9.85 \cdot 10^{-12}T^2$ $+1.53 \cdot 10^{-15}T^3 - 9.42 \cdot 10^{-20}T^4$
Material data for HMDSO	**Chemical Properties Handbook [182]**
Heat capacity [J/kg/K]	$5.96 \cdot 10^2 + 3.264T - 7 \cdot 10^{-4}T^2$ $-6.00 \cdot 10^{-7}T^3 + 3.00 \cdot 10^{-10}T^4$
Thermal conductivity [W/m/K]	$1.70 \cdot 10^{-2}$
Dynamic viscosity [kg/m/s]	$-3.50 \cdot 10^{-6} + 2.35 \cdot 10^{-7}T$
Diffusion	**Aspen Plus calculation**
Mass diffusivity [m^2/s]	$-6.054 \cdot 10^{-2} + 4.035 \cdot 10^{-4}T$

Bibliography

[1] H. Chatham. Oxygen diffusion barrier properties of transparent oxide coatings on polymeric substrates. *Surface & Coatings Technology*, 78(1–3):1–9, 1996.

[2] G. Pritchard. *Plastics Additives: A Rapra Market Report.* Rapra Technology, Shrewsbury, 2005.

[3] T. S. Ramu, M. R. Wertheimer, and J. E. Klemberg-Sapieha. Dielectric properties of plasma-polymerized hexamethyldisiloxane films. 1. Complex permittivity. *IEEE Transactions on Electrical Insulation*, 21(4):549–556, 1986.

[4] G. Czeremuszkin, M. Latreche, and M. R. Wertheimer. Plasma-enhanced chemical vapor deposition of transparent barrier coatings. *46th Annual Technical Conference Proceedings of the Society of Vacuum Coaters*, pages 586–591, 2003.

[5] J. S. Lewis and M. S. Weaver. Thin-film permeation-barrier technology for flexible organic light-emitting devices. *IEEE Journal of Selected Topics in Quantum Electronics*, 10(1):45–57, 2004.

[6] P. Mandlik, J. Gartside, L. Han, I. C. Cheng, S. Wagner, J. A. Silvernail, R.-Q. Ma, M. Hack, and J. J. Brown. A single-layer permeation barrier for organic light emitting displays. *Applied Physics Letters*, 92(10):103309/1–103309/3, 2008.

[7] A. S. Da Silva Sobrinho, N. Schuhler, J. E. Klemberg-Sapieha, M. R. Wertheimer, M. Andrews, and S. C. Gujrathi. Plasma-deposited silicon oxide and silicon nitride films on poly(ethylene terephthalate): A multitechnique study of the interphase regions. *Journal of Vacuum Science & Technology, A: Vacuum, Surfaces, and Films*, 16(4):2021–2030, 1998.

[8] A. Grüniger, A. Bieder, A. Sonnenfeld, Ph. Rudolf von Rohr, U. Müller, and R. Hauert. Influence of film structure and composition on diffusion barrier performance of SiO_x thin films deposited by PECVD. *Surface & Coatings Technology*, 200(14–15):4564–4571, 2006.

[9] A. S. Da Silva Sobrinho, M. Latreche, G. Czeremuszkin, J. E. Klemberg-Sapieha, and M. R. Wertheimer. Transparent barrier coatings on poly(ethylene terephthalate) by single- and dual-frequency plasma-enhanced chemical vapor deposition. *Journal of Vacuum Science & Technology, A: Vacuum, Surfaces, and Films*, 16(6):3190–3198, 1998.

[10] J. T. Felts and A. D. Grubb. Commercial-scale application of plasma processing for polymeric substrates: from laboratory to production. *Journal of Vacuum Science & Technology, A: Vacuum, Surfaces, and Films*, 10(4):1675–1681, 1992.

[11] N. Inagaki, S. Tasaka, and H. Hiramatsu. Preparation of oxygen gas barrier poly(ethylene terephthalate) films by deposition of silicon oxide films plasma-polymerized from a mixture of tetramethoxysilane and oxygen. *Journal of Applied Polymer Science*, 71(12):2091–2100, 1999.

[12] Y. Leterrier. Durability of nanosized oxygen-barrier coatings on polymers. *Progress in Materials Science*, 48(1):1–55, 2003.

[13] N. Schwarzer. Coating design due to analytical modelling of mechanical contact problems on multilayer systems. *Surface & Coatings Technology*, 133–134:397–402, 2000.

[14] W. Lohwasser. Large scale electron beam web coating not only for packaging. *43^{rd} Annual Technical Conference Proceedings of the Society of Vacuum Coaters*, pages 362–367, 2000.

[15] S. Amberg-Schwab, M. Hoffmann, H. Bader, and M. Gessler. Inorganic-organic polymers with barrier properties for water vapor, oxygen and flavors. *Journal of Sol-Gel Science & Technology*, 13(1–3):141–146, 1998.

[16] M. A. Lieberman and A. J. Lichtenberg. *Principles of Plasma Discharges and materials Processing.* Wiley & Sons, New York, 1994.

[17] J. D. Cobine. *Gaseous Conductors: Theory and Engineering Applications.* Dover publications Inc., New York, 1958.

[18] N. St. J. Braithwaite. Introduction to gas discharges. *Plasma Sources Science & Technology*, 9(4):517–527, 2000.

[19] J. L. Potter. Rarefied Gas Dynamics. In J. A. Schetz and A. E. Fuhs, editors, *Fundamentals of Fluid Mechanics*, pages 671–696. John Wiley & Sons, New York, 1999.

[20] L. Agres, Y. Ségui, R. Delsol, and P. Raynaud. Oxygen barrier efficiency of hexamethyldisiloxane/oxygen plasma-deposited coating. *Journal of Applied Polymer Science*, 61(11):2015–2022, 1996.

[21] R. W. Knoll and R. B. Heil. Effects of polymer surface characteristics on the performance of PECVD oxide barrier films. *39th Annual Technical Conference Proceedings of the Society of Vacuum Coaters*, pages 293–298, 1996.

[22] D. Korzec, D. Theirich, F. Werner, K. Traub, and J. Engemann. Remote and direct microwave plasma deposition of HMDSO films: comparative study. *Surface & Coatings Technology*, 74–75(Part 1):67–74, 1995.

[23] A. Schwabedissen, C. Soll, A. Brockhaus, and J. Engemann. Electron density measurements in a slot antenna microwave plasma source by means of the plasma oscillation method. *Plasma Sources Science & Technology*, 8(3):440–447, 1999.

[24] H. Nakashima, K. Furukawa, Y. C. Liu, D. W. Gao, Y. Kashiwazaki, K. Muraoka, K. Shibata, and T. Tsurushima. Low-temperature deposition of high-quality silicon dioxide films by sputtering-type electron cyclotron resonance plasma. *Journal of Vacuum Science & Technology, A: Vacuum, Surfaces, and Films*, 15(4):1951–1954, 1997.

[25] G. Dennler, A. Houdayer, P. Raynaud, I. Séguy, Y. Ségui, and M. R. Wertheimer. Growth modes of $\mathrm{SiO_x}$ films deposited by evaporation and plasma-enhanced chemical vapor deposition on polymeric substrates. *Plasmas and Polymers*, 8(1):43–59, 2003.

[26] J. E. Klemberg-Sapieha, O. M. Küttel, L. Martinu, and M. R. Wertheimer. Dual microwave-RF plasma deposition of functional coatings. *Thin Solid Films*, 193–194(1–2):965–972, 1990.

[27] R. Etemadi, C. Godet, M. Kildemo, J. E. Bourée, R. Brenot, and B. Drévillon. Dual-mode radio frequency/microwave plasma deposition of amorphous silicon oxide thin films. *Journal of Non-Crystalline Solids*, 187:70–74, 1995.

[28] J. Hao, W. Liu, and Q. Xue. Effect of N_2/CH_4 flow ratio on microstructure and composition of hydrogenated carbon nitride films prepared by a dual DC-RF plasma system. *Journal of Non-Crystalline Solids*, 353(2):136–142, 2007.

[29] F. Fracassi. Architecture of Plasma Reactors. In R. D'Agostino, P. Favia, and F. Fracassi, editors, *Plasma Processing of Polymers*, pages 47–64. Kluwer Academic Publishers, Dordrecht, 1997.

[30] A. Grüniger. *Deposition of SiO_x diffusion barriers on flexible packaging materials by plasma enhanced chemical vapor deposition.* PhD thesis, ETH Zurich, Switzerland, 2004.

[31] J. Goodman. The formation of thin polymer films in the gas discharge. *Journal of Polymer Science*, 44:551–552, 1960.

[32] M. Stuart. Dielectric properties of cross-linked polystyrene film formed in a glow discharge. *Nature (London, United Kingdom)*, 199(4888):59–60, 1963.

[33] H. Yasuda. *Plasma Polymerization.* Academic Press, INC., Orlando, 1985.

[34] A. T. Bell. The mechanism and kinetics of plasma polymerization. *Topics in Current Chemistry*, 94:43–68, 1980.

[35] T. Takagi. Ion-surface interactions during thin film deposition. *Journal of Vacuum Science & Technology, A: Vacuum, Surfaces, and Films*, 2(2):382–388, 1984.

[36] D. W. Hess. Plasma-surface interactions in plasma-enhanced chemical vapor deposition. *Annual Review of Materials Science*, 16:163–183, 1986.

[37] H. Yasuda and C. E. Lamaze. Polymerization in an electrodeless glow discharge. II. Olefinic monomers. *Journal of Applied Polymer Science*, 17(5):1519–1531, 1973.

[38] H. Yasuda, C. E. Lamaze, and K. Sakaoku. Effect of electrodeless glow discharge on polymers. *Journal of Applied Polymer Science*, 17(1):137–152, 1973.

[39] H. Yasuda, M. O. Bumgarner, H. C. Marsh, and N. Morosoff. Plasma polymerization of some organic compounds and properties of the polymers. *Journal of Polymer Science, Polymer Chemistry Edition*, 14(1):195–224, 1976.

[40] H. Yasuda and T. Hirotsu. Critical evaluation of conditions of plasma polymerization. *Journal of Polymer Science, Polymer Chemistry Edition*, 16(4):743–759, 1978.

[41] Y. Matsuda and H. Yasuda. Evaluation of plasma polymers of silanes as adhesion promoters for organic paint. *Thin Solid Films*, 118(2):211–224, 1984.

[42] D. Hegemann and M.-M. Hossain. Influence of non-polymerizable gases added during plasma polymerization. *Plasma Processes and Polymers*, 2(7):554–562, 2005.

[43] A. Sonnenfeld. *Beiträge zum Einsatz filametierter Barrierenentladungen unter Atmosphärendruck zur Abscheidung siliziumorganischer Schichten - Plasmachemische Stoffwandlung und Schichtanalyse*. PhD thesis, Ernst-Moritz-Arndt-Universität Greifswald, Germany, 2001.

[44] P. Favia, R. d'Agostino, and F. Fracassi. Plasma and surface diagnostics in PECVD from silicon containing organic monomers. *Pure and Applied Chemistry*, 66(6):1373–1380, 1994.

[45] R. Lamendola, R. d'Agostino, and F. Fracassi. Thin film deposition from hexamethyldisiloxane fed glow discharges. *Plasmas and Polymers*, 2(3):147–164, 1997.

[46] D. Magni, C. Deschenaux, C. Hollenstein, A. Creatore, and P. Fayet. Oxygen diluted hexamethyldisiloxane plasmas investigated by means of in situ infrared absorption spectroscopy and mass spectrometry. *Journal of Physics D: Applied Physics*, 34(1):87–94, 2001.

[47] F. Fracassi, R. d'Agostino, F. Fanelli, A. Fornelli, and F. Palumbo. GC-MS Investigation of Hexamethyldisiloxane-Oxygen Fed Plasmas. *Plasmas and Polymers*, 8(4):259–269, 2003.

[48] M. Goujon, T. Belmonte, and G. Henrion. OES and FTIR diagnostics of HMDSO/O_2 gas mixtures for SiO_x deposition assisted by RF plasma. *Surface & Coatings Technology*, 188–189:756–761, 2004.

[49] Y. Wang, J. Zhang, and X. Shen. Surface structures tailoring of hexamethyldisiloxane films by pulse rf plasma polymerization. *Materials Chemistry and Physics*, 96(2–3):498–505, 2006.

[50] J. T. Felts and T. John. Transparent Barrier Coatings Update: Flexible Substrates. *Journal of Plastic Film & Sheeting*, 9(2):139–158, 1993.

[51] J. E. Klemberg-Sapieha, L. Martinu, O. M. Küttel, and M. R. Wertheimer. Transparent gas barrier coatings produced by dual-frequency PECVD. *36th Annual Technical Conference Proceedings of the Society of Vacuum Coaters*, pages 445–449, 1993.

[52] Ch. Bichler, T. Kerbstadt, H. C. Langowski, and U. Moosheimer. Plasma-modified interfaces between polypropylene films and vacuum roll-to-roll coated thin barrier layers. *Surface & Coatings Technology*, 112(1–3):373–378, 1999.

[53] C. Misiano, E. Simonetti, P. Cerolini, F. Staffetti, and A. Fusi. Silicon oxide barrier improvement on plastic substrate. *34th Annual Technical Conference Proceedings of the Society of Vacuum Coaters*, pages 105–112, 1991.

[54] N. Inagaki and S. Tasaka. Preparation of oxygen gas barrier polypropylene films by deposition of SiO_x films plasma-polymerized from mixture of tetramethoxysilane and oxygen. *Journal of Applied Polymer Science*, 78(13):2389–2397, 2000.

[55] U. Moosheimer. Plasma pretreatment and coating of polymer films. Part 1. Coating of non-treated polymer films. *Materialwissenschaft & Werkstofftechnik*, 29(6):312–324, 1998.

[56] U. Moosheimer and C. Bichler. Plasma pretreatment of polymer films as a key issue for high barrier food packagings. *Surface & Coatings Technology*, 116–119:812–819, 1999.

[57] C. S. Deng, H. E. Assender, F. Dinelli, O. V. Kolosov, G. A. D. Briggs, T. Miyamoto, and Y. Tsukahara. Nucleation and growth of gas barrier aluminium oxide on surfaces of poly(ethylene terephthalate) and polypropylene: effects of the polymer surface properties. *Journal of Polymer Science, Part B: Polymer Physics*, 38(23):3151–3162, 2000.

[58] A. C. Ferrari and J. Robertson. Interpretation of Raman spectra of disordered and amorphous carbon. *Physical Review B*, 61(20):14095, 2000.

[59] J. Robertson. Ultrathin carbon coatings for magnetic storage technology. *Thin Solid Films*, 383(1–2):81–88, 2001.

[60] J. R. Galvão, F. P. Luce, D. L. Baptista, M. E. M. M. da Costa, C. M. Lepienski, and F. C. Zawislak. Ion irradiation effects on a-C:H, a-C:N:H

and a-C:F:H films. *Nuclear Instruments and Methods in Physics Research Section B: Beam Interactions with Materials and Atoms*, 249(1–2):409–413, 2006.

[61] L. A. Thomson, F. C. Law, N. Rushton, and J. Franks. Biocompatibility of diamond-like carbon coating. *Biomaterials*, 12(1):37–40, 1991.

[62] E. Tomasella, C. Meunier, and S. Mikhailov. a-C:H thin films deposited by radio-frequency plasma: influence of gas composition on structure, optical properties and stress levels. *Surface and Coatings Technology*, 141(2–3):286–296, 2001.

[63] L. Valentini, J. M. Kenny, G. Carlotti, G. Socino, L. Lozzi, and S. Santucci. Ar dilution effects on the elastic properties of hydrogenated amorphous hard-carbon films grown by plasma-enhanced chemical vapor deposition. *Journal of Applied Physics*, 89(2):1003–1007, 2001.

[64] N. Mutsukura and K. Akita. Infrared absorption spectroscopy measurements of amorphous CN_x films prepared in CH_4/N_2 RF discharge. *Thin Solid Films*, 349(1–2):115–119, 1999.

[65] D. S. Finch, J. Franks, N. X. Randall, A. Barnetson, J. Crouch, A. C. Evans, and B. Ralph. Diamond-like carbon, a barrier coating for polymers used in packaging applications. *Packaging Technology & Science*, 9(2):73–85, 1996.

[66] E. M. Moser, R. Urech, E. Hack, H. Künzli, and E. Müller. Hydrocarbon films inhibit oxygen permeation through plastic packaging material. *Thin Solid Films*, 317(1,2):388–392, 1998.

[67] A. Ogino and M. Nagatsu. Gas barrier properties of hydrogenated amorphous carbon films coated on polymers by surface-wave plasma chemical vapor deposition. *Thin Solid Films*, 515(7–8):3597–3601, 2007.

[68] R. W. Jaszewski, H. Schift, B. Schnyder, A. Schneuwly, and P. Gröning. The deposition of anti-adhesive ultra-thin teflon-like films and their interaction with polymers during hot embossing. *Applied Surface Science*, 143(1–4):301–308, 1999.

[69] Y. Iriyama, T. Yasuda, D. L. Cho, and H. Yasuda. Plasma surface treatment on nylon fabrics by fluorocarbon compounds. *Journal of Applied Polymer Science*, 39(2):249–264, 1990.

[70] D. F. Franceschini, C. A. Achete, and J. F. L. Freire. Internal stress reduction by nitrogen incorporation in hard amorphous carbon thin films. *Applied Physics Letters*, 60(26):3229–3231, 1992.

[71] L. G. Jacobsohn, D. F. Franceschini, and Jr. Freire, F. L. Hydrogenated carbon-nitrogen films obtained by PECVD using acetylene and nitrogen as precursor gases. *Materials Research Society Symposium Proceedings*, 498:283–288, 1998.

[72] S. E. Rodil, N. A. Morrison, J. Robertson, and W. I. Milne. Nitrogen incorporation into tetrahedral hydrogenated amorphous carbon. *Physica Status Solidi A: Applied Research*, 174(1):25–37, 1999.

[73] E. F. Motta and I. Pereyra. Amorphous hydrogenated carbon-nitride films prepared by RF-PECVD in methane-nitrogen atmospheres. *Journal of Non-Crystalline Solids*, 338–340:525–529, 2004.

[74] S. H. Lee and D. K. Park. Structural characterization of a-CN_x:H films deposited by low-frequency (60 Hz) PECVD at room temperature. *Journal of the Korean Physical Society*, 44(4):950–955, 2004.

[75] H. Y. Lee, D. K. Lee, D. H. Kang, J. J. Lee, and J. H. Joo. The effect of RF substrate bias on the properties of carbon nitride films produced by an inductively coupled plasma chemical vapor deposition. *Surface & Coatings Technology*, 193(1–3):152–156, 2005.

[76] L. Zajíčková, V. Bursikova, V. Perina, A. Mackova, and J. Janca. Correlation between SiO_x content and properties of DLC:SiO_x films prepared by PECVD. *Surface & Coatings Technology*, pages 281–285, 2002.

[77] B. C. Trasferetti, R. V. Gelamo, F. P. Rouxinol, M. A. Bica de Moraes, M. d. C. Goncalves, and C. U. Davanzo. Nanocomposites of Amorphous Hydrogenated Carbon and Siloxane Networks Produced by PECVD. *Chemistry of Materials*, 16(4):567–569, 2004.

[78] S. Tamulevičius and v. S. Meškinis. Diamond like Carbon Films: Growth and Characterization. In *Functionalized Nanoscale Materials, Devices and Systems*, pages 225–240. Springer Netherlands, 2008.

[79] J. G. Wijmans and R. W. Baker. The solution-diffusion model: a review. *Journal of Membrane Science*, 107(1–2):1–21, 1995.

[80] H. B. Hopfenberg and V. Stannett. Diffusion and sorption of gases and vapors in glassy polymers. *Physics of Glassy Polymers*, pages 504–547, 1973.

[81] V. Stannett. The transport of gases in synthetic polymeric membranes - a historic perspective. *Journal of Membrane Science*, 3(2–4):97–115, 1978.

[82] Y. G. Tropsha and N. G. Harvey. Activated Rate Theory Treatment of Oxygen and Water Transport through Silicon Oxide/Poly(ethylene terephthalate) Composite Barrier Structures. *Journal of Physical Chemistry B*, 101(13):2259–2266, 1997.

[83] M. Hanika, H.-C. Langowski, U. Moosheimer, and W. Peukert. Inorganic layers on polymeric films - influence of defects and morphology on barrier properties. *Chemical Engineering & Technology*, 26(5):605–614, 2003.

[84] J. T. Felts. Thickness effects on thin film gas barriers: silicon-based coatings. *34th Annual Technical Conference Proceedings of the Society of Vacuum Coaters*, pages 99–104, 1991.

[85] M. Yanaka, B. M. Henry, A. P. Roberts, C. R. M. Grovenor, G. A. D. Briggs, A. P. Sutton, T. Miyamoto, Y. Tsukahara, N. Takeda, and R. J. Chater. How cracks in SiOx-coated polyester films affect gas permeation. *Thin Solid Films*, 397(1,2):176–185, 2001.

[86] G. Rossi and M. Nulman. Effect of local flaws in polymeric permeation reducing barriers. *Journal of Applied Physics*, 74(9):5471–5475, 1993.

[87] A. P. Roberts, B. M. Henry, A. P. Sutton, C. R. M. Grovenor, G. A. D. Briggs, T. Miyamoto, M. Kano, Y. Tsukahara, and M. Yanaka. Gas permeation in silicon-oxide/polymer (SiO_x/PET) barrier films: role of the oxide lattice, nano-defects and macro-defects. *Journal of Membrane Science*, 208(1–2):75–88, 2002.

[88] A. S. Da Silva Sobrinho, G. Czeremuszkin, M. Latreche, G. Dennler, and M. R. Wertheimer. A study of defects in ultrathin transparent coatings on polymers. *Surface & Coatings Technology*, 116–119:1204–1210, 1999.

[89] F. J. Norton. Permeation of gaseous oxygen through vitreous silica. *Nature (London, United Kingdom)*, 191:701, 1961.

[90] E. L. Williams. Diffusion of Oxygen in Fused Silica. *Journal of the American Ceramic Society*, 48(4):190–194, 1965.

[91] E. W. Sucov. Diffusion of Oxygen in Vitreous Silica. *Journal of the American Ceramic Society*, 46(1):14–20, 1963.

[92] B. E. Deal and A. S. Grove. General relation for the thermal oxidation of silicon. *Journal of Applied Physics*, 36(12):3770–3778, 1965.

[93] A. S. Da Silva Sobrinho, G. Czeremuszkin, M. Latreche, and M. R. Wertheimer. Detection and characterization of defects in transparent barrier coatings. *42^{nd} Annual Technical Conference Proceedings of the Society of Vacuum Coaters*, pages 316–319, 1999.

[94] A. Grüniger and Ph. Rudolf von Rohr. Influence of defects in $\mathrm{SiO_x}$ thin films on their barrier properties. *Thin Solid Films*, 459(1–2):308–312, 2004.

[95] A. G. Erlat, R. J. Spontak, R. P. Clarke, T. C. Robinson, P. D. Haaland, Y. Tropsha, N. G. Harvey, and E. A. Vogler. $\mathrm{SiO_x}$ gas-barrier coatings on polymer substrates: morphology and gas transport considerations. *Journal of Physical Chemistry B*, 103(29):6047–6055, 1999.

[96] E. H. H. Jamieson and A. H. Windle. Structure and oxygen-barrier properties of metallized polymer film. *Journal of Materials Science*, 18(1):64–80, 1983.

[97] R. H. Doremus. *Glass Science*. Wiley, New York, 1973.

[98] A. S. Da Silva Sobrinho, G. Czeremuszkin, M. Latreche, and M. R. Wertheimer. Defect-permeation correlation for ultrathin transparent barrier coatings on polymers. *Journal of Vacuum Science & Technology, A: Vacuum, Surfaces, and Films*, 18(1):149–157, 2000.

[99] A. G. Erlat, B.-C. Wang, R. J. Spontak, Y. Tropsha, K. D. Mar, D. B. Montgomery, and E. A. Vogler. Morphology and gas barrier properties of thin $\mathrm{SiO_x}$ coatings on polycarbonate: correlations with plasma-enhanced chemical vapor deposition conditions. *Journal of Materials Research*, 15(3):704–717, 2000.

[100] W. Prins and J. J. Hermans. Theory of Permeation through Metal Coated Polymer Films. *The Journal of Physical Chemistry*, 63(5):716–720, 1959.

[101] J. Y. Robic, H. Leplan, Y. Pauleau, and B. Rafin. Residual stress in silicon dioxide thin films produced by ion-assisted deposition. *Thin Solid Films*, 290–291:34–39, 1996.

[102] H. Leplan, B. Geenen, J. Y. Robic, and Y. Pauleau. Residual stresses in evaporated silicon dioxide thin films: correlation with deposition parameters and aging behavior. *Journal of Applied Physics*, 78(2):962–968, 1995.

[103] M. Ohring. *Materials Science of Thin Films.* San Diego, CA: Academic Press, 2^{nd} edition, 2002.

[104] A. K. Sinha and T. T. Sheng. The temperature dependence of stresses in aluminum films on oxidized silicon substrates. *Thin Solid Films*, 48(1):117–126, 1978.

[105] M. S. Haque, H. A. Naseem, and W. D. Brown. Residual stress behavior of thin plasma-enhanced chemical vapor deposited silicon dioxide films as a function of storage time. *Journal of Applied Physics*, 81(7):3129–3133, 1997.

[106] L.-N. He, T. Inokuma, Y. Kurata, and S. Hasegawa. Stress in Amorphous SO_x:H Films Prepared by Plasma-Enhanced Chemical Vapor Deposition. *Japanese Journal of Applied Physics*, 35:1873–1879, 1995.

[107] M. Akira and A. Yoshihiro. Residual stress and thermal expansion coefficient of plasma polymerized films. *Journal of Applied Polymer Science*, 27(6):2139–2150, 1982.

[108] Y. Leterrier, Y. Wyser, and J. A. E. Månson. Internal stresses and adhesion of thin silicon oxide coatings on poly(ethylene terephthalate). *Journal of Adhesion Science & Technology*, 15(7):841–865, 2001.

[109] G. G. Stoney. The Tension of Metallic Films Deposited by Electrolysis. *Proceedings of the Royal Society of London. Series A*, 82(553):172–175, 1909.

[110] Y. Inoue and Y. Kobatake. Mechanics of adhesive joints: Part III. Evaluation of residual stress. *Applied Scientific Research A*, 7:314, 1958.

[111] Y. Leterrier, Y. Wyser, J. A. E. Månson, and J. Hilborn. A method to measure the adhesion of thin glass coatings on polymer films. *Journal of Adhesion*, 44(3):213–227, 1994.

[112] M. S. Hu and A. G. Evans. The cracking and decohesion of thin films on ductile substrates. *Acta Metallurgica*, 37(3):917–925, 1989.

[113] P. H. Wojciechowski and M. S. Mendolia. Fracture and cracking phenomena in thin films adhering to high-elongation substrates. *Physics of Thin Films*, 16:271–340, 1992.

[114] M. Yanaka, Y. Tsukahara, N. Nakaso, and N. Takeda. Cracking phenomena of brittle films in nanostructure composites analyzed by a modified shear lag model with residual strain. *Journal of Materials Science*, 33(8):2111–2119, 1998.

[115] H. L. Cox. The elasticity and strength of paper and other fibrous materials. *British Journal of Applied Physics*, 3(3):72–79, 1952.

[116] A. Kelly and W. R. Tyson. Tensile properties of fiber-reinforced metals. Copper/tungsten and copper/molybdenum. *Journal of the Mechanics and Physics of Solids*, 13(6):329–350, 1965.

[117] A. C. Kimber and J. G. Keer. On the theoretical average crack spacing in brittle matrix composites containing continuous aligned fibres. *Journal of Materials Science Letters*, 1(8):353–354, 1982.

[118] J. L. Beuth. Cracking of thin bonded films in residual tension. *International Journal of Solids and Structures*, 29(13):1657–1675, 1992.

[119] J. Andersons, J. Modniks, Y. Leterrier, G. Tornare, P. Dumont, and J. A. E. Månson. Evaluation of toughness by finite fracture mechanics from crack onset strain of brittle coatings on polymers. *Theoretical and Applied Fracture Mechanics*, 49(2):151–157, 2008.

[120] J. Dundurs and D. B. Bogy. Edge-Bonded Dissimilar Orthogonal Elastic Wedges under Normal and Shear Loading. *Journal of Applied Mechanics*, 36(3):650–652, 1969.

[121] S. Schmauder and M. Meyer. Correlation between Dundurs' parameters and elastic constants. *Zeitschrift für Metallkunde*, 83(7):524–527, 1992.

[122] A. P. McGuigan, G. A. D. Briggs, V. M. Burlakov, M. Yanaka, and Y. Tsukahara. An elastic-plastic shear lag model for fracture of layered coatings. *Thin Solid Films*, 424(2):219–223, 2003.

[123] A. Bieder. *PECVD of* SiO_x *films from oxygen and hexamethyldisiloxane in a double source reactor*. PhD thesis, ETH Zurich, Switzerland, 2006.

[124] C. L. Yaws, P. K. Narasimhan, and C. Gabbula. *Yaws' Handbook of Antoine coefficients for vapor pressure.* Knovel, Norwich, 2$^{\text{nd}}$ electronic edition, 2005.

[125] H. Fujiwara. *Spectroscopic ellipsometry: principles and applications.* John Wiley & Sons, Chichester, England; Hoboken, NJ, 2007.

[126] G. Beamson and D. Briggs. *High Resolution XPS of Organic Polymers.* John Wiley & Sons Ltd, Chichester, UK, 1992.

[127] D. A. Shirley. High-resolution x-ray photoemission spectrum of the valence bands of gold. *Physical Review B: Solid State*, 5(12):4709–4714, 1972.

[128] M. F. Ashby. On the engineering properties of materials. *Acta Metallurgica*, 37(5):1273–1293, 1989.

[129] J. Park, K. Eom, O. Kwon, and S. Woo. Chemical etching technique for the investigation of melt-crystallized isotactic polypropylene spherulite and lamellar morphology by scanning electron microscopy. *Microscopy & Microanalysis*, 7(3):276–286, 2001.

[130] D. Hegemann, H. Brunner, and Ch. Oehr. Evaluation of deposition conditions to design plasma coatings like SiO_x and a-C:H on polymers. *Surface & Coatings Technology*, 174–175:253–260, 2003.

[131] R. Lamendola and R. d'Agostino. Process control of organosilicon plasmas for barrier film preparations. *Pure and Applied Chemistry*, 70(6):1203–1208, 1998.

[132] K. H. A. Bogart, S. K. Ramirez, L. A. Gonzales, G. R. Bogart, and E. R. Fisher. Deposition of SiO_2 films from novel alkoxysilane/O_2 plasmas. *Journal of Vacuum Science & Technology, A: Vacuum, Surfaces, and Films*, 16(6):3175–3184, 1998.

[133] Y. Sawada, S. Ogawa, and M. Kogoma. Synthesis of plasma-polymerized tetraethoxysilane and hexamethyldisiloxane films prepd. by atmospheric pressure glow discharge. *Journal of Physics D: Applied Physics*, 28(8):1661–1669, 1995.

[134] P. G. Pai, S. S. Chao, Y. Takagi, and G. Lucovsky. Infrared spectroscopic study of SiO_x films produced by plasma enhanced chemical vapor deposition. *Journal of Vacuum Science & Technology A: Vacuum, Surfaces, and Films*, 4(3):689–694, 1986.

[135] A. Kucirkova and K. Navratil. Interpretation of infrared transmittance spectra of SiO_2 thin films. *Applied Spectroscopy*, 48(1):113–120, 1994.

[136] W. A. Pliskin. Comparison of properties of dielectric films deposited by various methods. *Journal of Vacuum Science & Technology*, 14(5):1064–1081, 1977.

[137] K. Aumaille, C. Vallée, A. Granier, A. Goullet, F. Gaboriau, and G. Turban. A comparative study of oxygen/organosilicon plasmas and thin $SiO_xC_yH_z$ films deposited in a helicon reactor. *Thin Solid Films*, 359(2):188–196, 2000.

[138] M. Creatore, F. Palumbo, and R. d'Agostino. Deposition of SiO_x Films from Hexamethyldisiloxane/Oxygen Radiofrequency Glow Discharges: Process Optimization by Plasma Diagnostics. *Plasmas and Polymers*, 7(3):291–310, 2002.

[139] J. A. Theil, J. G. Brace, and R. W. Knoll. Carbon content of silicon oxide films deposited by room temperature plasma enhanced chemical vapor deposition of hexamethyldisiloxane and oxygen. *Journal of Vacuum Science & Technology, A: Vacuum, Surfaces, and Films*, 12(4):1365–1370, 1994.

[140] G. Lucovsky, M. J. Manitini, J. K. Srivastava, and E. A. Irene. Low-temperature growth of silicon dioxide films: a study of chemical bonding by ellipsometry and infrared spectroscopy. *Journal of Vacuum Science & Technology, B: Microelectronics and Nanometer Structures*, 5(2):530–537, 1987.

[141] H. Tsuchida, I. Kamata, and K. Izumi. Si-H Bonds on the 6H-SiC(0001) Surface after H_2 Annealing. *Japanese Journal of Applied Physics*, 36(6A):L699–L702, 1997.

[142] S. M. Han and E. S. Aydil. Study of surface reactions during plasma enhanced chemical vapor deposition of SiO_2 from SiH_4, O_2, and Ar plasma. *Journal of Vacuum Science & Technology, A: Vacuum, Surfaces, and Films*, 14(4):2062–2070, 1996.

[143] Y. Ogata, H. Niki, T. Sakka, and M. Iwasaki. Hydrogen in porous silicon: vibrational analysis of SiH_x species. *Journal of the Electrochemical Society*, 142(1):195–201, 1995.

[144] D. S. Wavhal, J. Zhang, M. L. Steen, and E. R. Fisher. Investigation of Gas Phase Species and Deposition of SiO_2 Films from HMDSO/O_2 Plasmas. *Plasma Processes and Polymers*, 3(3):276–287, 2006.

[145] R. Balkova, J. Zemek, V. Cech, J. Vanek, and R. Prikryl. XPS study of siloxane plasma polymer films. *Surface & Coatings Technology*, 174–175:1159–1163, 2003.

[146] L. Zuri, M. S. Silverstein, and M. Narkis. Organic-inorganic character of plasma-polymerized hexamethyldisiloxane. *Journal of Applied Polymer Science*, 62(12):2147–2154, 1996.

[147] M. R. Alexander, R. D. Short, F. R. Jones, W. Michaeli, and C. J. Blomfield. A study of HMDSO/O_2 plasma deposits using a high-sensitivity and high-energy resolution XPS instrument: curve fitting of the Si 2p core level. *Applied Surface Science*, 137:179–183, 1999.

[148] L.-A. O'Hare, A. Hynes, and M. R. Alexander. A methodology for curve-fitting of the XPS Si 2p core level from thin siloxane coatings. *Surface & Interface Analysis*, 39(12–13):926–936, 2007.

[149] S. Roualdes, R. Berjoan, and J. Durand. 29Si NMR and Si2p XPS correlation in polysiloxane membranes prepared by plasma enhanced chemical vapor deposition. *Separation & Purification Technology*, 25(1–3):391–397, 2001.

[150] J. F. Moulder, W. F. Stickle, P. E. Sobol, and K. D. Bomben. *Handbook of X-Ray Photoelectron Spectroscopy.* Perkin-Elmer, Physical Electronics Division, Eden Prairie, MN, USA, 1995.

[151] E. Görlich, J. Haber, A. Stoch, and J. Stoch. XPS study of [alpha]-quartz surface. *Journal of Solid State Chemistry*, 33(1):121–124, 1980.

[152] S. D. Gardner, C. S. K. Singamsetty, G. L. Booth, G.-R. He, and C. U. Pittman. Surface characterization of carbon fibers using angle-resolved XPS and ISS. *Carbon*, 33(5):587–595, 1995.

[153] B. C. Repka. Olefin polymers - Polypropylene. *Kirk-Othmer Encycl. Chem. Technol.*, 14:282–309, 1967.

[154] B. Degamber, D. Winter, J. Tetlow, M. Teagle, and G. F. Fernando. Simultaneous DSC/FTIRS/TMA. *Measurement Science & Technology*, 15(9):L5–L10, 2004.

[155] J.-H. Zhao, T. Ryan, P. S. Ho, A. J. McKerrow, and W.-Y. Shih. Measurement of elastic modulus, Poisson ratio, and coefficient of thermal expansion of on-wafer submicron films. *Journral of Applied Physics*, 85(9):6421–6424, 1999.

[156] M. Y. M. Chiang, C. K. Chiang, and W. L. Wu. A Technique for Deducing In-Plane Modulus and Coefficient of Thermal Expansion of a Supported Thin Film. *Journal of Engineering Materials and Technology*, 124(2):274–277, 2002.

[157] B. Bridge, N. D. Patel, and D. N. Waters. On the elastic constants and structure of the pure inorganic oxide glasses. *Physica Status Solidi A: Applied Research*, 77(2):655–668, 1983.

[158] C.-L. Dai and Y.-M. Chang. A resonant method for determining mechanical properties of Si_3N_4 and SiO_2 thin films. *Materials Letters*, 61(14–15):3089–3092, 2007.

[159] D. Hegemann, U. Vohrer, Ch. Oehr, and R. Riedel. Deposition of SiO_x films from O_2/HMDSO plasmas. *Surface & Coatings Technology*, 116–119:1033–1036, 1999.

[160] A. Bieder, V. Gondoin, Y. Leterrier, G. Tornare, Ph. Rudolf von Rohr, and J. A. E. Månson. Mechanical properties of carbon-modified silicon oxide barrier films deposited by plasma enhanced chemical vapor deposition on polymer substrates. *Thin Solid Films*, 515(13):5430–5438, 2007.

[161] M. Yanaka, Y. Kato, Y. Tsukahara, and N. Takeda. Thickness effect on cracking phenomena and mechanical properties of submicron glass thin films deposited on a polymer substrate. *Materials Research Society Symposium Proceedings*, 555:33–38, 1999.

[162] G. Dennler, A. Houdayer, M. Latreche, Y. Ségui, and M. R. Wertheimer. Studies of the earliest stages of plasma-enhanced chemical vapor deposition of SiO_2 on polymeric substrates. *Thin Solid Films*, 382(1,2):1–3, 2001.

[163] J. Brandrup and E. H. Immergut, editors. *Polymer Handbook*. Wiley, New York, 2^{nd} edition, 1975.

[164] L. G. Jacobsohn and Jr. Freire, F. L. Influence of the plasma pressure on the microstructure and on the optical and mechanical properties of

amorphous carbon films deposited by direct current magnetron sputtering. *Journal of Vacuum Science & Technology, A: Vacuum, Surfaces, and Films*, 17(5):2841–2849, 1999.

[165] Z. Sun, C. H. Lin, Y. L. Lee, J. R. Shi, B. K. Tay, and X. Shi. Effects on the deposition and mechanical properties of diamond-like carbon film using different inert gases in methane plasma. *Thin Solid Films*, 377–378:198–202, 2000.

[166] K. Chakrabarti, J. B. Kim, J. I. B. Wilson, and C. Lee. Effects of Ar Gas Dilution in Methane Plasma on the Properties of Diamond-like Carbon Films. *Physica Status Solidi A: Applied Research*, 194(1):112–117, 2002.

[167] D. F. Franceschini. Plasma-deposited a-C(N):H films. *Brazilian Journal of Physics*, 30(3):517–526, 2000.

[168] K. J. Clay, S. P. Speakman, G. A. J. Amaratunga, and S. R. P. Silva. Characterization of a-C:H:N deposition from CH_4/N_2 RF plasmas using optical emission spectroscopy. *Journal of Applied Physics*, 79(9):7227–7233, 1996.

[169] N. Inagaki and H. Yasuda. The initial and terminating stage of glow discharge polymerization investigated by thickness monitor. *Journal of Applied Polymer Science*, 26(11):3557–3563, 1981.

[170] J. H. Kaufman, S. Metin, and D. D. Saperstein. Symmetry breaking in nitrogen-doped amorphous carbon: infrared observation of the Raman-active G and D bands. *Physical Review B: Condensed Matter and Materials Physics*, 39(18):13053–13060, 1989.

[171] M. Jelinek, J. Zemek, M. Trchova, V. Vorlicek, J. Lancok, R. Tomov, and M. Simeckova. CN_x films created by combined laser deposition and RF discharge: XPS, FTIR and Raman analysis. *Thin Solid Films*, 366(1,2):69–76, 2000.

[172] L. G. Jacobsohn, Jr. Freire, F. L., D. F. Franceschini, M. M. Lacerda, and G. Mariotto. Growth kinetics and relationship between structure and mechanical properties of a-C(N):H films deposited in acetylene-nitrogen atmospheres. *Journal of Vacuum Science & Technology, A: Vacuum, Surfaces, and Films*, 17(2):545–551, 1999.

[173] J. Schwan, W. Dworschak, K. Jung, and H. Ehrhardt. Microstructures and mechanical properties of amorphous hydrogenated carbon-nitrogen films. *Diamond & Related Materials*, 3(7):1034–1039, 1994.

[174] B. M. Henry, H. Nörenberg, F. Dinelli, C. R. M. Grovenor, G. A. D. Briggs, Y. Tsukahara, and T. Miyamoto. The Effect of Thermal Cycling Damage on the Permeability and Structure of Transparent Gas Barrier Films. *Chemical Engineering & Technology*, 22(12):1010–1011, 1999.

[175] H. Sunami, Y. Itoh, and K. Sato. Stress and thermal-expansion coefficient of chemical-vapor-deposited glass films. *Journal of Applied Physics*, 41(13):5115–5117, 1970.

[176] D. Hegemann, U. Schütz, and Ch. Oehr. RF-Plasma Deposition of SiO_x and a-C:H as Barrier Coatings on Polymers. In R. d'Agostino, P. Favia, Ch. Oehr, and M. R. Wertheimer, editors, *Plasma Processes and Polymers*, pages 23–37. Wiley-VCH Verlag GmbH & Co. KGaA, Weinheim, 2005.

[177] J. Kron, S. Amberg-Schwab, and G. Schottner. Functional coatings on glass using ORMOCER systems. *Journal of Sol-Gel Science and Technology*, 2(1–3):189–192, 1994.

[178] P. Zinck, M. F. Pays, R. Rezakhanlou, and J. F. Gerard. Mechanical characterisation of glass fibers as an indirect analysis of the effect of surface treatment. *Journal of Materials Science*, 34(9):2121–2133, 1999.

[179] V. V. Krzhizhanovskaya, P. M. A. Sloot, and Y. E. Gorbachev. Grid-Based Simulation of Industrial Thin-Film Production. *Simulation*, 81(1):77–85, 2005.

[180] S.-J. Son, K.-W. Yi, J. Mahrholz, and K. T. Rie. Numerical studies on up scaling of metal organic PACVD processes used for tribological coating in automotive industry. *Surface & Coatings Technology*, 201(16–17):7318–7326, 2007.

[181] D. J. Collins, A. J. Strojwas, and Jr. White, D. D. A CFD model for the PECVD of silicon nitride. *IEEE Transactions on Semiconductor Manufacturing*, 7(2):176–183, 1994.

[182] C. L. Yaws. *Chemical Properties Handbook.* McGraw-Hill, New York, 1999.

[183] R. B. Bird, W. E. Stewart, and E. N. Lightfoot. *Transport Phenomena.* John Wiley & Sons, New York, 1960.

List of publications

Journal publications

1. L. Körner, A. Sonnenfeld, and Ph. Rudolf von Rohr. Multilayer Diffusion Barrier Coatings on Poly(propylene) with Improved Temperature Durability. *Plasma Processes and Polymers*, 6(S1):S660–S664, 2009.
2. L. Körner, A. Sonnenfeld, R. Heuberger, J. H. Waller, Y. Leterrier, J. A. E. Månson, and Ph. Rudolf von Rohr. Oxygen permeation, mechanical and structural properties of multilayer diffusion barrier coatings on polypropylene. *Journal of Physics D: Applied Physics*, 43(11):115301–11, 2010.
3. L. Körner, A. Sonnenfeld, and Ph. Rudolf von Rohr. Silicon Oxide Diffusion Barrier Coatings on Polypropylene. *Thin Solid Films*, 518:4840–4846, 2010.

Patent

1. L. Körner, A. Sonnenfeld, and Ph. Rudolf von Rohr. Plastic film with good barrier effect after a sterilisation treatment. *Patent Application Publication*, (WO 2010031461), 2010.

Conference contributions

1. L. Körner, A. Sonnenfeld, and Ph. Rudolf von Rohr. Influence of Pretreatment on the Deposition of SiO_x Diffusion Barrier Coatings on Polypropylene Substrate. *2nd Material Research Center (MRC) Graduate Symposium*, Zurich, 2007.
2. L. Körner, A. Sonnenfeld, and Ph. Rudolf von Rohr. Process optimization of PECVD of SiO_x diffusion barrier coatings on polypropylene substrate and the influence of plasma pretreatment. *NanoEurope Symposium*, St. Gallen, 2007.
3. L. Körner, A. Sonnenfeld, and Ph. Rudolf von Rohr. Influence of Pretreatment on the Deposition of SiO_x Diffusion Barrier Coatings on Polypropylene Substrate. *18th International Symposium on Plasma Chemistry (ISPC)*, Kyoto, 2007.
4. A. Sonnenfeld, L. Körner, and Ph. Rudolf von Rohr. Gas and radiation barrier coatings. *19th International Symposium on Plasma Chemistry (ISPC)*, Bochum, 2009.

5. L. Körner, A. Sonnenfeld, Y. Leterrier, and Ph. Rudolf von Rohr. Mechanical properties of the oxygen barrier dyad system of a pp-HMDSO and a silica-like thin film. *19th International Symposium on Plasma Chemistry (ISPC)*, Bochum, 2009.

Acknowledgements

The present work was conducted at the Institute of Process Engineering at ETH Zurich between October 2006 and April 2010. This project was facilitated by the financial support of Alcan Technology & Management AG and the Commission for Technology and Innovation (CTI).
First of all, I would like to thank my supervisor, Prof. Philipp Rudolf von Rohr, for his continuous support throughout this thesis, for his confidence in me, and for providing the necessary freedom for conducting this work. I wish to express my gratitude to Prof. Nicholas Spencer for being my co-supervisor, regardless of a busy schedule.
Special thanks go to Dr. Markus Dippel and Wolfgang Lohwasser of the Alcan Technology & Management AG for the excellent collaboration and the fruitful discussions.
Several people are gratefully acknowledged for their scientific contribution to the success of this project. Dr. Axel Sonnenfeld introduced me to and increased my interest in the field of plasma physics. He always offered me a sympathetic ear and provided good advice during my work. I thank the other members of the 'LTR plasma group', Dr. Patrick Reichen, Dr. Adrian Spillmann, and Christian Roth, for the scientific discussions, their help, good times at conferences, and the latter two for the SEM analyses. I am deeply indebted to Dr. Yves Leterrier and Judith H. Waller of the Laboratoire de Technologie des Composites et Polymères (LTC) at the EPFL for providing me assistance with the fragmentation tests and for the DMA. I really enjoyed the discussions and learned a lot about thin film mechanics during my numerous stays in Lausanne. I wish to thank Dr. Roman Heuberger for his competence in XPS analysis. Prof. Uwe Pieles and Dr. Patrick Shahgaldian are grate-

fully acknowledged for the AFM investigations, Dr. Barbora Malisova and Prof. Marcus Textor from the Laboratory for Surface Science and Technology (LSST, ETH Zurich) for providing access to the ellipsometer, the Center of Mechanics at the Institute of Mechanical Systems (IMES, ETH Zurich) for the use of the surface profiler, and Simon Steiner of the Centre of Structure Technologies for the tensile tests. Thanks also go to Markus Huber and Prof. Marco Mazzotti for more or less consciously providing access to the DSC, the optical microscope, and the most precise balance at the institute.

The mechanical and electrical workshop of the institute, by name Bruno Kramer, Peter Feusi, Peter Hoffmann, René Plüss, Christan Rohrbach, Martin Meuli, Werner Hess, and Jovo Vidic, contributed considerably to the success of this work with their experience of many years, their practical advice, and their fast help. Sincere thanks are given to Silvia Christoffel, Patricia Horn, and Silke Stubbe for their dedicated work regarding administrative issues and to Sascha Jovanovic, Justina Palmer, and Beni Cadonau for the IT support. I wish to thank my student Eveline Zumstein for her motivated work and the careful handling of the sensitive fiber-optical temperature measurement system. My predecessors, Andrea Bieder and Andrea Grüniger, are also gratefully acknowledged here. I could benefit a lot from their effort although we unfortunately never shared any time at the LTR.

I also wish to thank all former and present colleagues of the LTR group, especially Carsten, Simon, Franz, Donata, Karol, Pädi, Cédi, Christian, Martin, Axel, Ädu, Serge, Tobi R., Tobi V., Bruno, Adi, Panos, Holger, Nora, Yannick, Vasillis, and Thomas, for the good working (and after-work) atmosphere. Many of you became very good ‘colleagues’ not only in the literal but also in the Swiss-German sense.

Finally, I wish to thank my family for always supporting and encouraging me in whatever I am doing. Very special thanks are dedicated to my dearest Ina for her love and, particularly towards the end of the project, for her moral support and patience.

Curriculum Vitae

Lutz Körner

Date of birth: May 25, 1978

Place of birth: Stuttgart, Germany

Citizen of: Germany

10/2006–04/2010	Doctoral studies at the Institute of Process Engineering, ETH Zurich (Prof. Ph. Rudolf von Rohr)
03/2006–09/2006	Teaching assistant at the Institute of Process Engineering, ETH Zurich (Prof. Ph. Rudolf von Rohr)
10/1999–01/2006	Graduate studies in Process Engineering University of Stuttgart, Germany academic degree: Dipl.-Ing.
06/2005–11/2005	Internship at Daimler Chrysler AG, Sindelfingen
09/2003–11/2004	Exchange studies, diploma thesis University of Wisconsin (UW), Madison, USA (Prof. J.A. Dumesic, Prof. M. Mavrikakis)
08/1998–07/1999	Civil service, Germany
1989–1998	Secondary school, Stuttgart, Germany academic degree: Abitur
1985–1989	Primary school, Neuhausen, Germany

Zurich, April 2010